
Molecular dynamics simulations of protein-protein interactions and THz driving of molecular rotors on gold

Jan Neumann



Munich 2011

Molecular dynamics simulations of protein-protein interactions and THz driving of molecular rotors on gold

Jan Neumann

Dissertation
at the Faculty of Physics
of the Ludwig-Maximilians-University
Munich, Germany
presented by
Jan Neumann
from Wolfenbüttel

Munich, June 15, 2011

First referee: Prof. Dr. Kay E. Gottschalk

Second referee: Prof. Dr. Joachim Rädler

Day of the defence: July 19, 2011

Contents

Zusammenfassung	1
Abstract	3
1 Introduction	5
2 Theory	11
2.1 MD Simulations	11
2.1.1 Born-Oppenheimer approximation	11
2.1.2 Classical dynamics	13
2.1.3 Force fields	14
2.1.4 Simulation details	16
2.2 Force measurements on proteins	19
2.2.1 Protein structure	19
2.2.2 Energy landscape of a protein	20
2.2.3 Thermodynamics and kinetics	22
2.2.4 Single-molecule AFM force spectroscopy	25
2.2.5 Single-molecule force probe MD simulations	27
2.3 Molecular rotors	29
2.3.1 Basic principles	29
2.3.2 Classification of rotors	30
2.3.3 Rotor behavior	32
3 Force-Based Analysis of Multidimensional Energy Landscapes	37
3.1 Aims	37
3.2 Antibody-Antigen Interaction	38
3.2.1 Biological background	38
3.2.2 Summary	38
3.2.3 Publication P1	40

3.3	Barnase-Barstar	41
3.3.1	Biological background	41
3.3.2	Summary	41
3.3.3	Publication P2	43
4	Force response of the integrin-talin complex	45
4.1	Aims	45
4.2	Biological background	46
4.2.1	Motivation	46
4.2.2	Integrin	46
4.2.3	Talin	48
4.3	Summary	48
4.4	Outlook	50
4.5	Publication P3	51
5	Controlling molecular rotation on gold	53
5.1	Aims	53
5.2	Motivation	53
5.3	Summary	54
5.4	Outlook	58
5.5	Publication P4	59
6	List of Publications and Manuscripts	61
	List of Publications and Manuscripts	61
	Force-based Analysis of ... an Antibody Fragment-Peptide Complex	62
	The Effect of Different Force Applications on ... Barnase-Barstar	77
	The Integrin Talin Complex under Force	91
	Driving and controlling a molecular surface rotor with THz electric fields . .	117
	References	141
	Acknowledgement	155

List of Figures

2.1	Force Field	14
2.2	Protein Structure	20
2.3	From Levinthal to Funnels	21
2.4	Chemical reaction rates	23
2.5	Atomic force microscopy setup	26
3.1	Antibody-Antigen binding sites	39
3.2	Barnase-Barstar complex	42
4.1	Integrin active and passive conformations	47
5.1	Molecular rotor on gold	55

List of Tables

2.1	Rotor classification by structure according to review Kottas et al. ¹¹¹ . .	31
2.2	Rotor classification by function according to review Kottas et al. ¹¹¹ . .	32
4.1	This overview lists the three modular binding sites of the integrin we identify and describes their interaction sites.	49

Nomenclature

AFM	atomic force microscope
ATP	adenosinetriphosphate
COM	center of mass
DES	diethylsulfid
ECM	extracellular matrix
FERM	four point one, ezrin, radixin, and moesin
FRET	Förster resonance energy transfer
GFP	green fluorescent protein
iPALM	interferometric photoactivated localization microscopy
LJ	Lennard-Jones
MD	molecular dynamics
NMR	nuclear magnetic resonance
RNA	ribonucleic acid
RNAse	ribonuclease
SMD	steered molecular dynamics
STM	scanning tunneling microscope

Zusammenfassung

Proteine sind die molekularen Maschinen der Zelle und gehören zu den essentiellen Grundbausteinen des Lebens. Ganze Netzwerke aus dynamischen Protein-Protein Wechselwirkungen steuern das Leben auf zellulärer Ebene. Thema dieser Arbeit ist es mittels Computersimulationen ein besseres Verständnis von Proteinkomplexen und molekularen Rotoren zu erlangen. Hierbei konzentriere ich mich auf drei Schwerpunktthemen: Erstens trage ich dazu bei ein besseres Verständnis zur methodischen Untersuchung der Energielandschaften von Proteinen und Proteinkomplexen mittels der Anwendung vektorieller Kräfte zu erlangen. Zweitens wende ich diese Methode an um den biologisch wichtigen Integrin-Talin Komplex zu studieren, welcher die initiale, kraftleitende Verbindung zwischen Zellinnerem und -äußeren schafft. Drittens studiere ich wie mittels elektrischer Terahertz-Felder ein molekular Rotor auf einer Goldoberfläche gesteuert wird.

Kräfte sind von Natur aus vektorielle Größen. Zur eindeutigen Beschreibung sind Betrag, Richtung und Angriffspunkt nötig. Am Beispiel zweier Protein Komplexe werden Wichtigkeit und Einfluß verschiedener Kraftparameter für die Entwicklung des Systems unter Krafteinfluss untersucht. Das erste System ist ein Antikörper-Peptid Komplex. Antikörper sind essentielle Bestandteile des adaptiven Immunsystems und ihre Hauptaufgabe besteht in der Bindung pathogener Antigene. Anhand einer solchen Antikörper-Antigen Bindung wird gezeigt, dass die Variation der Kraftangriffspunkte zu unterschiedlichen Entbindungspfaden mit jeweils zwei Hauptbarrieren führt. Experimentelle Ergebnisse mittels Atomarer Kraftmikroskopie (AFM) stimmen hierbei sehr gut mit Molekularen Dynamik (MD) Simulationen des Systems überein. Ferner konnte ich für alle Entbindungsbarrieren die genauen molekularen Wechselwirkungen mittels MD Simulationen identifizieren.

Ein weiteres interessantes System ist der Barnase-Barstar Komplex. Die evolutionäre Optimierung des Ribonuklease-Inhibitor Komplexes hat eine sehr starke Bindung geschaffen. Anhand dieses Komplexes werden weitere Protokolle für die Erkundung der Energielandschaft von Protein Komplexen getestet. Besonders hervorzuheben ist, das mittels variierender Parameter eine interne Hierarchie der Stabilität der Bindungs-

und Faltungsmotive erstellt werden kann. Zusätzlich wird gezeigt, dass mit hohen Zuggeschwindigkeiten die Labilität und somit die Barrieren des Komplexes dominieren, während bei niedrigen Zuggeschwindigkeiten die Stabilität und die Minima in der Energielandschaft das Verhalten des Komplexes bestimmen.

Kräfte sind nicht nur Mittel zum Zweck, sondern beeinflussen das Leben auf allen Längenskalen, von ganzen Organismen bis zu nanoskopischen Proteinen. Für Integrine als die wichtigsten Adhäsionsrezeptoren der Zellen spielen Kräfte physiologisch eine besonders wichtige Rolle. Das Integrin wird von seinem Ligand Talin aktiviert. Der Integrin-Talin Komplex stellt die initiale kraftleitende Verbindung zwischen extrazellulärer Matrix und intracellulärem Zytoskelett her. Die zwei wichtigsten Ergebnisse sind die Erweiterung des Aktivierungsmechanismus des Komplexes um eine zusätzlich benötigte Kraftkomponente und die Entdeckung der kraftinduzierten Stabilisierung des Komplexes durch die Ausbildung eines stabilisierenden beta-Faltblatts zwischen Integrin und Talin. Des Weiteren konnte ich zeigen, dass der Komplex versucht sich entlang seiner mechanisch stabileren Achse auszurichten, falls er frei rotieren kann.

In der Natur sind molekulare Rotoren wichtige Bausteine für einige essentielle Nanomaschinen. Besonders bekannte Beispiele hierfür sind die F1-ATPase oder das Flagellum von Bakterien. In beiden Fällen entscheidet die Rotationsrichtung sogar über die Wirkung der Maschinen. Für die kontrollierte Verwendung von Rotoren in künstlichen Nanomaschinen wird ein besseres Verständnis dieser Systeme vonnöten sein. In meinem letzten Projekt untersuche ich einen diethylsulfid Rotor auf einer Gold (111) Oberfläche mittels MD Simulationen. Die Energielandschaft dieses Rotors kann mit elektrischen Feldern im Terahertzbereich so manipuliert werden, dass die effektive Rotationsrichtung und -frequenz im Gigahertzbereich gesteuert werden kann. Eine theoretische Beschreibung dieses Phänomens und seine Abhängigkeit von der Struktur des Rotors werden behandelt. Dies kann ein erster Schritt zu einem Interface zwischen bekannten elektrischen Schaltungen und zukünftigen künstlichen Nanomaschinen sein.

Abstract

The scope of this work is to gain insight and a deeper understanding of exploring and controlling molecular devices like proteins and rotors by fine tuned manipulation via mechanical or electrical energies. I focus on three main topics. First, I investigate vectorial forces as a tool to explore the energy landscape of protein complexes. Second, I apply this method to a biologically important force transduction complex, the integrin-talin complex. Third, I use Terahertz electric fields to manipulate the energy landscape of a molecular rotor on a gold surface and drive their effective rotation bidirectionally.

Force is by nature a vector and depends on its three parameters: magnitude, direction and attachment point. Here, the impact of different force protocols varying these parameters is shown for an antibody-antigen complex and the ribonuclease-inhibitor complex barnase-barstar. Antibodies are essential for our adaptive immune system in their function to bind specific antigens. Here, the binding of an antibody to a peptide is probed with varying attachment points. Different attachment points clearly change the dissociation pathways. The barriers identified using experimental atomic force microscopy (AFM) and molecular dynamics (MD) simulations are in excellent agreement. I determine the molecular interactions of two main barriers for each setup. This results in a common outer barrier of the complex and different inner barriers probed by AFM. The ribonuclease barnase and its inhibitor barstar form an evolutionary optimized complex. Different force protocols are shown to determine the hierarchy of relative stability within a protein complex. For the barnase-barstar complex, the internal fold of the barstar is identified to be less stable than the barnase-barstar binding interaction. High velocities probe the lability or barriers of the system while low velocities probe the stability or energy wells of this system.

Forces impact biological life on totally different length scales which range from whole organisms to individual proteins. Integrins are the major cell adhesion receptors binding to the extracellular matrix and talin. Talin activates the integrins and creates the initial connection to the actin cytoskeleton of the cell. Here, I have chosen to investigate the integrin-talin complex as a biologically important force transduc-

tion complex. The force dependence of the system is probed by constant force MD simulations. The two main results include the activation of the complex and its force response. I demonstrate, that the binding of talin to integrin does not disrupt the integrin's transmembrane helix interactions sterically. Since, this disruption is necessary for integrin activation, a modified activation mechanism requiring a small force application is proposed. The response of the integrin-talin complex normal and parallel to the cell membrane is analyzed. The complete dissociation pathways generated for both directions identify a force-induced formation of a stabilizing beta strand between integrin and talin only for normal forces. Furthermore, the complex tries to rotate such that the external force aligns with the more force resistant axis of the complex.

In nature, molecular rotors are essential building blocks of many molecular machines and brownian motors like the F1-ATPase or the flagellum of a bacterium. The direction of rotation often steers different processes in clockwise and counterclockwise directions. Rotation on the nanoscopic level in artificial devices is still very limited and requires a deeper understanding. In my last project, I study the switching and driving of a molecular diethylsulfid rotor on a gold (111) surface by Terahertz electric fields. The response of the rotational energy landscape to static and oscillation electric fields is analyzed. Varying the Terahertz driving frequency, the rotation direction and frequency are controlled. A theoretical framework is presented to describe the behavior of the molecular rotor. This can be seen as the first step into the direction of man-made controllable nano-devices driven and controlled by energy from the electric wall-socket.

1

Introduction

Biological life arose from inorganic matter by forming a first generation of organic macromolecules¹. These macromolecules gained the ability of self-organization and self-replication. Life evolved from single- to multi-cellular organisms. Today, all organisms depend on the functional interaction of highly specialized molecular nanomachines, the proteins.

How can you gain insight into the nanoscopic world of life on the molecular level? The answer lies in the combination of different approaches. This highly interdisciplinary research area, the life sciences, complement each other by accumulating ideas and exchanging methods and knowledge from physics, biology, chemistry, computer sciences and medicine. It can be subdivided into many fields of active research. One of these fields is biophysics. In this interdisciplinary field, physical toolkits and methods are used to study biological building blocks and systems. My contribution to this field is the examination and manipulation of the energy landscape of protein-protein complexes using molecular dynamics (MD) simulations. In addition to these mechanical manipulations I study the control of a non-deterministic molecular rotor with Terahertz electric fields.

Protein function and protein-protein interactions are determined by their dynamics as well as by their stability². In the past 15 years, observing protein internal dynamics became possible due to advanced experimental methods like nuclear magnetic resonance (NMR) relaxation experiments³⁻⁵. Förster resonance energy transfer

(FRET) experiments can be used to study protein folding, protein-protein interactions and in vivo protein transport or turnover⁶⁻⁹. Single-molecule force spectroscopy like atomic force microscopy (AFM) or optical traps can detect forces resulting from conformational changes, binding or activation events. The unfolding and refolding of titin and bacteriorhodopsin¹⁰⁻¹² or the ligand dependent fluctuations of calmodulin¹³ are prominent examples (For details on AFM see Section 2.2.4).

However, experimental techniques are not capable to yield insight into protein dynamics on the atomistic level, yet. Therefore, computer simulations can be used to complement experimental techniques¹⁴. Molecular dynamics (MD) simulations integrate classical Newton dynamics using empirical force fields to simulate the time development of a system. An ever increasing amount of computational power^{15,16} and improving algorithms allow to reach increasing system sizes and simulation timescales from picoseconds up to a few milliseconds¹⁷. Large systems with a few million atoms like the simulation of virus capsids^{18,19} or large macromolecules like a ribosome^{20,21} can be simulated. Simulations of the NTL9(1-39) identify a set of 1.5 ms long folding pathways¹⁷. Even though, biological processes and transitions may require even longer times under equilibrium conditions. A reduction of the system size using a coarse graining or the use of implicit water can speed up the simulation at the cost of reduced accuracy. Parallel approaches like replica exchange molecular dynamics simulate the system at multiple temperatures²² or intelligent sampling methods like the Markov Model approach in the NTL9 protein folding can optimize the sampling of slow processes within a given computational time²³. Since the protein dynamics is determined by their potential energy landscape, the addition of a potential can speed up such processes. Conformational flooding like methods employ artificial potentials destabilizing sampled conformations^{24,25}. The drawbacks are that the system can neither be dynamically steered nor mimicked by experiments. In this work, we use mechanical and electric energy to influence the energy landscape of the chosen systems. Mechanical forces are used to achieve optimal steering of the transitions along the chosen reaction coordinate by tilting the energy landscapes.

The application of forces in MD simulations is realized by mimicking AFM ex-

periments. Harmonic potentials are used as analogon to mechanical springs which can manipulate individual atoms, residues or chains. Combining MD simulations and experiments enable to identify the key events in force-induced unfolding of the titin immunoglobulin domain I27²⁶ or in the exploration of the energy landscape of the antibody fragment H6 binding to the leucine zipper GCN4-p1 antigen²⁷ (Section 3.2). Furthermore, MD simulations are challenged to gain predictive character and first successes have been made¹⁴. For example, the talin rod unfolding simulations predicted decryption of hidden vinculin binding sites under force²⁸. This effect has been confirmed by magnetic tweezer, total internal reflection and AFM measurements approximately one year later²⁹.

Forces are characterized by their magnitude, their direction and their specific attachment point. These three characteristics determine the influence of the applied force on the system and its evolution. An example for the importance of the direction and attachment point of forces is the well studied molecule ubiquitin. Chains of ubiquitin molecules linked by different covalent bonds are found in nature. It is shown by single molecule force experiments and computer simulations that the mechanical stability of ubiquitin depends on the attachment points of the force³⁰⁻³². The application of forces at different attachment points to a protein is also used by the group of Prof. M. Rief to probe the green fluorescent protein (GFP) molecule with single molecule force measurements. They gain the unfolding energy landscape of the GFP and can model the dependence on the force application to the molecule with an elastic bond network³³⁻³⁵. The choice of the force application may critically influence the results of experiments and simulations.

Life at the molecular level is not based on the function of isolated proteins, but on a finely choreographed interplay of proteins interacting with each other and their environment. Thus, this work focusses on studying the examination of protein-protein interactions. My first project in cooperation with Dr. J. Morfill and Prof. H. E. Gaub combines experimental AFM measurements with MD simulations to explore the energy landscape of an antibody binding to a target peptide. The binding site of the complex is not only defined by the binding energy since its dissociation pathways

differs for each force attachment point. The combined efforts of experiments and simulations could identify a two barrier unbinding with the higher barrier being dominant in the equilibrium dissociations and the lower barrier with the smaller potential width to be dominating the AFM results. The SMD simulations could identify the atomistic interactions for each barrier (Section 3.2). My second project intensifies the studies on the influence of different applied force vectors to protein complexes. The well studied and highly stable barnase barstar complex serves as a model complex. The effect of attachment points, geometry and loading rates of the applied forces are studied. A high loading rate (fast pulling) is shown to test the lability of the energy landscape. Slow changes address the stability of the system. The final conformational state of the unbound proteins strongly depended on the force attachment points. The individual folds of both binding partners are shown to be less stable than the protein-protein binding site (Section 3.3).

Forces are not only a tool to explore and examine proteins. Many biological systems experience forces in a physiological environment. For example, the gigantic titin protein fulfills an essential passive role in muscle contraction and elasticity^{26,37}. The enzymatic role of the titin kinase has been shown to be actively regulated by forces³⁸. On the cellular level tension plays an important role. Cells forming tissues interact with each other as well as with the extracellular matrix (ECM)^{39–41}. In this context, adhesion forces and force sensing of the environment are essential. Integrins are the major class of cell adhesion receptors which mediate cell-cell and cell-ECM interactions. Furthermore, they transmit bidirectional signals and forces between ECM and their cytoplasmic domain^{42,43}. The integrins play central roles in cellular adhesion, migration, apoptosis, development and immune responses^{44,45}. For functional adhesions, the integrins need to be connected to the cytoskeleton of the cell⁴⁶. Recent three-dimensional interferometric photoactivated localization microscopy (iPALM) measurements showed that the talin molecules bridge the cytoplasmic gap between integrins and the cytoskeleton⁴⁷. Talin is an essential adaptor protein which activates the integrins on the inside-out signaling pathway⁴⁸. It is composed of the head domain binding the integrin and its rod domain binding the actin

cytoskeleton. The rod domain is shown to decrypt hidden vinculin binding sites under force to allow additional mechanical stabilization^{29,49}. Recently, structures of the integrins transmembrane region⁵⁰ is solved by NMR, while the integrin-talin complex⁵¹ and the complete talin head group⁵² are solved by X-ray crystallography. This allows to study the integrin-talin complex by MD simulations.

In my third project I focus on the direct interface of the integrin-talin complex by simulating the complex under equilibrium conditions and analyze the fluctuation behavior of the integrin residues. Finally, I probe the integrin-talin complex with constant forces in the range of 20 - 500 pN in different directions and identify the residues important for the mechanical stability of the complex. These residues are highly conserved and show strong binding. The force response of the complex is found to be direction dependent. Further, I determine a force induced formation of an intermolecular beta-sheet which stabilizes the integrin-talin complex against forces normal to the plane of the cell membrane. This is the key mechanism in the self-strengthening force response of the complex. Based on these results, we proposed a force dependent activation of the integrin extending a recently published mechanism by Anthis et al.⁵¹. More details can be found in Chapter 4.

My last project is a cooperation with Prof. R.D. Astumian. Complementing my previous work, the energy landscape of a molecular diethylsulfide (DES) rotor on a gold (111) surface is now influenced by Terahertz electric fields instead of by mechanical forces. But why should we study molecular rotation? Since the invention of the wheel approx. 4000 BC, rotation in the macroscopic world is part of our daily lives. Cars, engines or soccer - so much depends on rotation. In the nanoscopic world rotations are as widely spread as in the macroscopic. Rotations occur around chemical bonds or in essential machines like the F1-ATPase⁵³ or the bacterial flagellar motor⁵⁴. However, the behavior of macroscopic systems is different from nanoscopic ones. Low Reynolds numbers and high thermal noise dominate the behavior of many nanoscopic systems^{55,56}. The harvesting of molecular rotation for biotechnological devices or a deep understanding of rotational concepts are yet to be achieved. Our system is a minimal system of a small molecule rotating on a periodically structured surface in

vacuum. It has been studied experimentally with a scanning tunneling microscope (STM) by the group of Prof. E. C. H. Sykes⁵⁷. We use parallel static and oscillating electric fields to characterize and drive the molecular rotor depending on its conformational state. The intrinsic energy landscape dependent on the rotational angle and the current field is simulated. The rotor's frequency response on the external electric field could be modeled with two main contributions at the characteristic frequency and at twice its value. Thus, we provide a theoretical framework for the understanding of electric driving of surface mounted rotational motion. Details can be found in Chapter 5. This theory can be used as a first step to design biotechnical applications driven by surface mounted molecular rotors in the GHz regime. This may be a first step to fuel molecular machines like the F1-ATPase in a highly parallel way directly by electric current from a power socket.

In summary, I focussed on gaining a better understanding of manipulating and exploring molecular devices like proteins and rotors by fine tuned manipulation via mechanical or electrical energies.

2

Theory

This chapter describes the theoretical frameworks and basic methods on which this dissertation is based on. Specific biological details and particular methods used in the projects can be found in Chapters 3.2 - 5

2.1 Molecular Dynamics simulations

The main method of my thesis are MD simulations. These computer simulations calculate the dynamics of molecular systems like proteins, rotors or membranes using statistical mechanics and Newton's equation of motion in atomistic detail. MD simulations are based on the following three main approximations. Textbooks on MD can give further insight^{58,59}.

2.1.1 Born-Oppenheimer approximation

Aim: Separation of motion into time-independent electron and time-dependent atomic nuclei motion.

The time-dependent Schrödinger equation describes the time evolution of a quantum system.

$$\mathcal{H}\Psi = i\hbar\frac{\delta\Psi}{\delta t} \quad (2.1)$$

where the Hamiltonian \mathcal{H} describes the sum of potential and kinetic energy. Ψ is the wave function which contains the information about all particles of the system and \hbar the Planck constant divided by 2π .

Since the analytical calculation of the exact solution of the Schrödinger equation for multiple nuclei and electrons is not possible, Max Born and J. Robert Oppenheimer proposed to decouple the motion of the atomic nuclei from the motion of the electrons⁶⁰. If the velocity of the atomic nuclei is small compared to the electrons, it can be assumed that the electrons adapt to the state of the atomic nuclei adiabatically and instantaneously. As a result the wave function Ψ of the complete system can be written as a product of the time-dependent wave function of the atomic nuclei Ψ_n and the time-independent electron wave function Ψ_e

$$\Psi(\mathbf{R}, \mathbf{r}, t) = \Psi_n(\mathbf{R}, t)\Psi_e(\mathbf{r}; \mathbf{R}) \quad (2.2)$$

where $\mathbf{R} = (\mathbf{R}_1, \mathbf{R}_2, \dots, \mathbf{R}_N)$ and $\mathbf{r} = (\mathbf{r}_1, \mathbf{r}_2, \dots, \mathbf{r}_K)$ are the coordinates of the N nuclei and the K electrons, respectively.

The wave function Ψ_e of the electronic subsystem depends only on the coordinates \mathbf{R} and not on the velocities $\mathbf{v}_\mathbf{R}$ of the nuclei. Thus, the electronic subsystem is solved given fixed nuclei positions \mathbf{R} by

$$\mathcal{H}_e(\mathbf{R})\Psi_e(\mathbf{r}; \mathbf{R}) = E_e(\mathbf{R})\Psi_e(\mathbf{r}; \mathbf{R}). \quad (2.3)$$

The electric Hamiltonian $\mathcal{H}_e = \mathcal{H} - \mathcal{H}_n$ can be expressed as the Hamiltonian of the complete system \mathcal{H} minus the Hamiltonian of the nuclei \mathcal{H}_n . The energy eigenvalues $E_e(\mathbf{R})$ of eq. 2.3 represent the potential energy surface. By applying 2.2 and 2.3 to 2.1, the following time-dependent Schrödinger equation for the atomic nuclei can be obtained:

$$(T_n + E_e(\mathbf{R}))\Psi_n(\mathbf{R}, t) = i\hbar \frac{\delta\Psi_n(\mathbf{R}, t)}{\delta t} \quad (2.4)$$

T_n is the kinetic energy of the nuclei. The Born-Oppenheimer approximation is valid as long as the electronic eigenvalues E_e of eq. 2.3 are not overlapping. This can

usually be assumed for molecules in the ground state.

2.1.2 Classical dynamics

Aim: Speed up simulations by treating large quantum mechanical systems with classical physics.

Due to the large number of atoms in current MD simulations, the calculation of the molecular dynamics is restricted to the motion of the atomic nuclei. Furthermore, solving the time-dependent Schrödinger equation of the system would be too time consuming. Therefore, the nuclei are treated as classical particles (Ehrenfest theorem⁶¹) with a potential energy

$$V(\mathbf{R}) = E_e^0(\mathbf{R}) \quad (2.5)$$

with the potential energy surface of the ground state $E_e^0(\mathbf{R})$ according to eq. 2.3. The motion of the nuclei is described by Newton mechanics:

$$\mathbf{F}_i = m_i \cdot \mathbf{a}_i \quad (2.6)$$

$$-\nabla_{\mathbf{R}_i} V(\mathbf{R}) = m_i \cdot \frac{\delta^2 \mathbf{R}_i}{\delta t^2} \quad (2.7)$$

with the force \mathbf{F}_i and the acceleration \mathbf{a}_i acting on the i th atom of the system. The time evolution of the system is calculated in small time steps Δt by the leap-frog algorithm⁶²:

$$\mathbf{v}_i(t + \frac{\Delta t}{2}) = \mathbf{v}_i(t - \frac{\Delta t}{2}) + \frac{\mathbf{F}_i(t)}{m_i} \cdot \Delta t \quad (2.8)$$

$$\mathbf{R}_i(t + \Delta t) = \mathbf{R}_i(t) + \mathbf{v}_i(t + \frac{\Delta t}{2}) \cdot \Delta t. \quad (2.9)$$

These equations are solved iteratively every time step resulting in trajectories of positions $\mathbf{R}(t)$ (and velocities $\mathbf{v}(t) = (\mathbf{v}_1(t), \mathbf{v}_2(t), \dots, \mathbf{v}_N(t))$) for all atoms ($i=1,2,\dots,N$)

in the system. The time step Δt of the simulation is restricted to 1 fs by the fastest relaxation times of the system, the bond and angle vibrations involving hydrogen atoms. These bond vibrations do not generally couple to the global protein domain motions. They can be constrained by algorithms like LINCS to increase the time step to 2 - 4 fs⁶³.

2.1.3 Force fields

Aim: Replace solving of electronic Schrödinger equation by using empirical potentials.

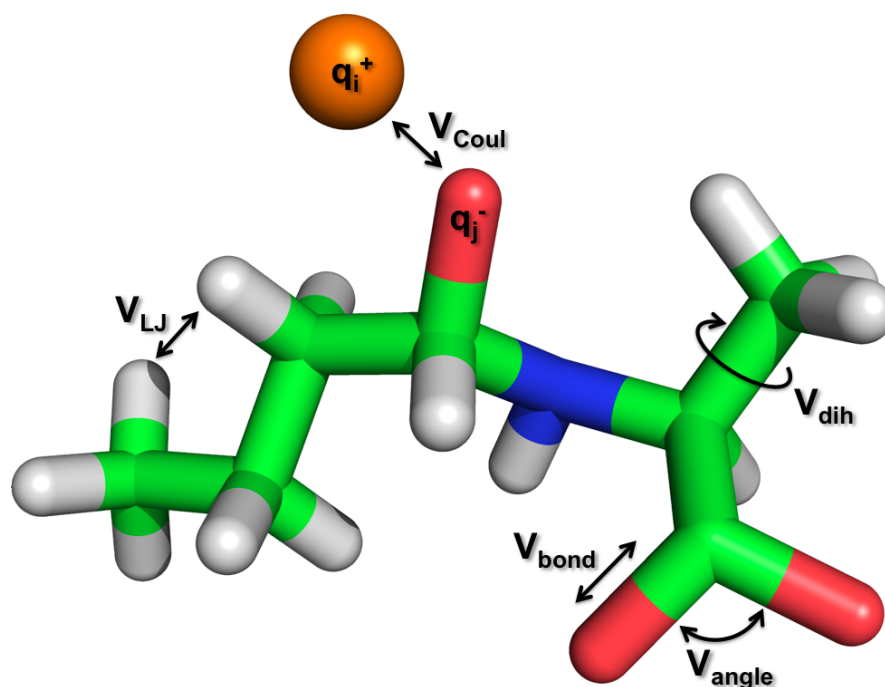


Figure 2.1: This figure indicates the different types of potentials used for a force field.

MD simulations require a potential energy landscape $V(\mathbf{R})$ to describe the atomic interactions in the system. The Born-Oppenheimer approximation reduces this problem to a time-independent Schrödinger equation which depends on the positions of

the nuclei of the system only. Due to the large number of electrons in proteins, the computational costs are too high to solve equation 2.3. Thus, the potential energy surface is approximated by a force field $V(\mathbf{R})$. It is built from classical potential energy expressions and their associated adjustable parameters⁶⁴. Pairwise additivity of these energy terms is usually assumed.

Figure 2.1 illustrates the main energy terms contributing to a Force Field $V(\mathbf{R})$. The bonded energy terms describe bond stretching (V_{bond}), angle bending (V_{angle}) and torsion around dihedral angles (V_{dih}). The non-bonded terms are the Lennard-Jones (V_{LJ}) and Coulomb (V_{Coul}) potentials.

$$\begin{aligned}
 V(\mathbf{R}) &= V_{bond} + V_{angle} + V_{torsion} + V_{LJ} + V_{Coulomb} & (2.10) \\
 &= \sum_{\text{bonds}} \frac{k_b}{2} (l - l_{eq})^2 \\
 &+ \sum_{\text{angles}} \frac{k_\theta}{2} (\theta - \theta_{eq})^2 \\
 &+ \sum_{\text{dihedrals}} \frac{V_n}{2} (1 + \cos(n\Phi - \delta)) \\
 &+ \sum_{\text{pairs } i,j} 4\epsilon_{ij} \left[\left(\frac{\sigma_{ij}}{R_{ij}} \right)^{12} - \left(\frac{\sigma_{ij}}{R_{ij}} \right)^6 \right] + \frac{q_i q_j}{4\pi\epsilon_0 R_{ij}} & (2.11)
 \end{aligned}$$

The bond and angle force field parameters are the force constants k_b , k_θ , the equilibrium angles θ_{eq} and equilibrium bond lengths l_{eq} . The torsion potential is described by its multiplicity n , its barrier height V_n and its phase δ . Improper dihedrals are treated analog to normal angles. The non-bonded parameters are the partial charges q_i and the Lennard-Jones (LJ) parameters ϵ_{ij} and σ_{ij} . Further details can be found in the review by Prof. W.L. Jorgensen⁶⁴.

In this thesis, the classical OPLS all atom force field is used for all protein-protein interaction projects (Chapters 3.2-4)⁶⁵. For the simulation of the molecular rotor on gold in Chapter 5 the GolP force field is applied. It is optimized to describe peptide adsorption to gold in vacuum⁶⁶.

2.1.4 Simulation details

In this subsections, some general details of MD simulations used in this thesis are discussed. All MD simulations are performed using the GROMACS software package⁶⁷⁻⁷⁰. Further technical details can be found in the GROMACS manual⁷¹.

Explicit water and periodic boundary conditions

Proteins do not only interact with other proteins, but their natural environment features membranes, macromolecules, ions and water as interaction partners. For simulating protein-protein interactions the complexes are solvated in explicit water with physiological concentrations of sodium chloride. Periodic boundary conditions are used to minimize artifacts caused by boundaries⁵⁸ with simulation boxes large enough to accommodate all simulated conformations of each system properly.

Non-bonded interactions

The most time consuming step in MD simulations is the calculation of the non-bonded interactions. The number of interactions scales with $\mathcal{O}(N^2)$ quadratically with the number of the atoms N in the simulated system (double sum in eq. 2.11). To improve the scaling for large systems, the with R^{-6} fast decaying LJ interactions are typically cut off between 1.0 to 1.4 nm. The long ranging Coulomb interactions decay slowly with R^{-1} and cannot simply be cutoff⁷². Therefore, the Particle-Mesh Ewald (PME) algorithm scaling with $\mathcal{O}(N \log N)$ is used⁷³. Here, the interaction potential V_{Coul} is separated into a short ranged term V_{sr} and a long ranged term V_{lr} . By calculating the short ranged term in real space and the long-ranged term in reciprocal space using Fast Fourier Transformation with a discrete mesh both terms converge quickly⁷⁴.

Temperature coupling

The temperature T in MD simulations is defined by the kinetic energy E_{kin} of the system⁷⁰

$$E_{kin} = \sum_{\text{atoms } i} \frac{m_i v_i^2}{2} = \frac{1}{2} N_f k_B T \quad (2.12)$$

with N_f degrees of freedom, the Boltzmann constant k_B , the velocity v_i and mass m_i of the i th atom.

Numerical integration, approximation of non-bonded interactions or dissipative work done on the system can change the temperature T of a (sub)system. Coupling the simulation box to a large temperature bath with a fixed reference temperature T_0 can correct this effect. Therefore, the Berendsen algorithm⁷⁵ is based on extending the simple Newtonian equation 2.6 to a Langevin formulation by introducing a friction and a stochastic term, using a Gaussian stochastic variable ξ_i with zero mean.

$$m_i \cdot \dot{\mathbf{v}}_i = \mathbf{F}_i - \frac{m_i}{2\tau_T} v_i + \xi_i(t) \quad (2.13)$$

$$\langle \xi_i(t) \xi_j(t + \tau_T) \rangle = \frac{m_i}{\tau_T} k_B T_0 \delta(\tau_T) \delta_{ij} \quad (2.14)$$

It effectively rescales the velocities of the particles ($v' = \lambda v$) with a factor

$$\lambda = \sqrt{1 + \frac{\Delta t}{\tau_T} \left(\frac{T_0}{T} - 1 \right)} \quad (2.15)$$

with the coupling time constant τ_T and the integration time step Δt . The change in temperature is then described by

$$\frac{dT(t)}{dt} = \frac{1}{\tau_T} (T_0 - T(t)). \quad (2.16)$$

The Berendsen thermostat does not result in a well-defined ensemble. Depending on the coupling time constant τ_T something between a micro canonical and a canonical ensemble is created⁷⁶. In 2007 the velocity rescaling algorithm was developed to allow

a canonical distribution. It can be understood as a Berendsen thermostat with an added stochastic term including Wiener noise dW ⁷⁷

$$\frac{dT(t)}{dt} = \frac{1}{\tau_T}(T_0 - T(t)) + 2\sqrt{\frac{T_0 T(t)}{N_f \tau_T}} \frac{dW}{dt}. \quad (2.17)$$

The velocity rescaling algorithm is used in the more recent integrin/talin and rotor projects.

Pressure coupling

For the equilibration of the systems, a Berendsen pressure coupling is used⁷⁵. Analog with the temperature coupling the system is coupled to an external pressure bath. The box vectors are scaled to decay toward a chosen reference pressure P_0 by

$$\frac{dP(t)}{dt} = \frac{1}{\tau_P}(P_0 - P(t)) \quad (2.18)$$

. where τ_P is the time constant for the pressure coupling.

2.2 Force measurements on proteins

The examination of the protein-protein interactions using directed force vectors requires a background about proteins. Their energy landscape and kinetic interaction models in equilibrium and under force are reviewed. Relevant force probe techniques will complement this section.

2.2.1 Protein structure

Proteins have different levels of internal structure and organization (Figure 2.2). Their basic building blocks are the amino acids. The 22 different standard amino acids can be connected via peptide bonds. The sequence of amino acids is called the primary structure of a protein.

The functional form of a protein is a complex three dimensional structure. It has two structural main motifs: α -helices and β -sheets, also called secondary structure elements. These are stabilized by hydrogen bond interactions and connected via flexible loops. The final three dimensional structure of a single protein is called the tertiary structure of the protein. Its formation is often driven by non-specific hydrophobic interactions and stabilized by hydrogen bonds, salt-bridges, van-der-Waals interactions and/or disulfide bonds. A complex of multiple proteins is called a quaternary structure. It is stabilized by the same interactions as a tertiary structure⁷⁹.

The calculation of the three dimensional protein structure from its amino acid sequence is still only possible for small proteins⁸⁰⁻⁸⁵. Larger structures are solved with the help of experiments. Experimental structure determination at atomistic detail is mainly driven by X-ray crystallography and nuclear magnetic resonance (NMR) spectroscopy. Both techniques result in static structures of stable conformations. The importance of protein structures is clearly stated by the Nobel Prize in 1962. It was awarded for the first atomic structure of a protein using X-ray crystallography to John Kendrew and Max Perutz⁸⁶.

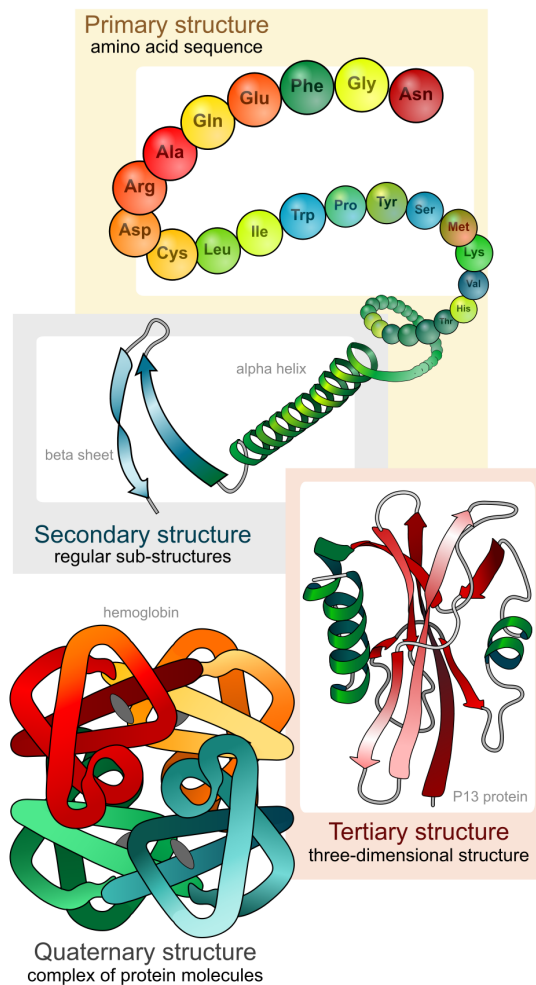


Figure 2.2: This figure shows the different levels of protein structure. (Taken from Wikipedia⁷⁸)

2.2.2 Energy landscape of a protein

The description of the protein complexes and molecules in terms of an energy landscape is used in all projects of this thesis. The main development of this energy landscape picture for proteins was done in the field of protein folding. The prediction of a protein structure from the knowledge of its sequence alone is one of the goals in

proteomics. According to Anfinsen's thermodynamic hypothesis, the native structure of most proteins is a thermodynamically stable structure under the given environmental conditions^{87,88}. Thus, it is independent of its kinetic folding pathway and depends only on its intrinsic high dimensional energy landscape.

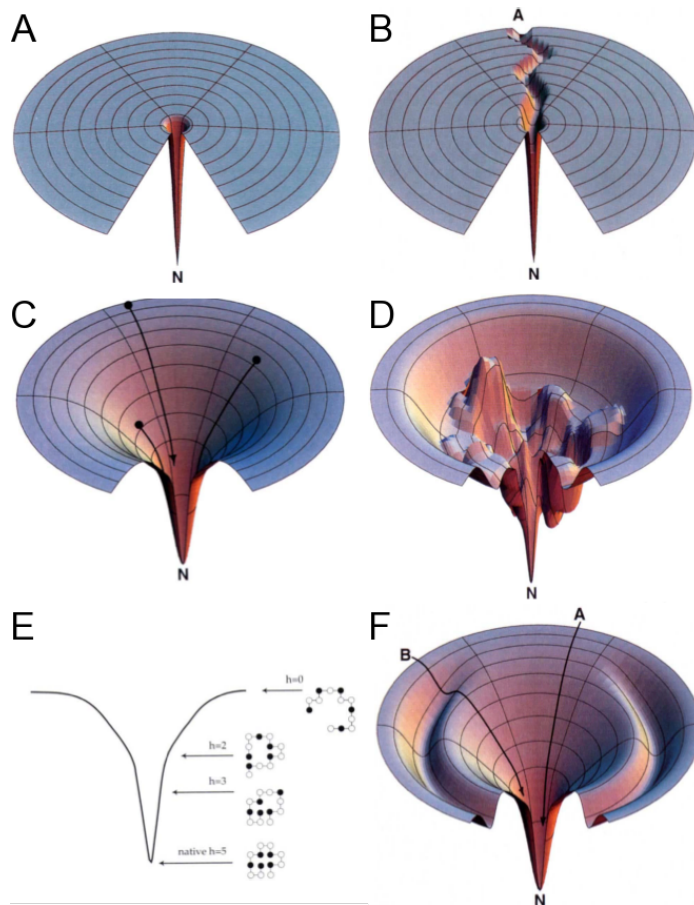


Figure 2.3: This figure shows different views of protein folding funnels. (Taken from Dill et. al.⁸⁹)

Finding the native state by a random search in a huge conformational energy landscape would require much longer times than biological folding experiments actually do. This conflict is thus known as Levinthal's paradox⁸⁹. Figure 2.3 A pictures a golf course potential energy landscape on which a random walk (e.g. by a golf ball)

would search very long to find the minimum. Levinthal proposed a folding pathway of intermediates leading to a reduced search time. Lacking a physical basis for this model, the idea of a funnel shaped energy landscape was introduced⁸⁹⁻⁹¹ (Fig. 2.3 C). Thus, different pathways can lead to the same energy minimum. The progressive organization through various stages of partial folding on the way to the native structure results in a rugged energy landscape⁹² (Fig. 2.3 D and E). The ruggedness of the energy landscape around the native structure allows proteins and protein complexes multiple functional conformations^{93,94}.

For a protein to function, it needs to undergo dynamic changes. The functions of a protein like enzymatic reactions, conformational changes, association or dissociation can all be understood as the protein moving on its free energy landscape. Therefore, these processes are controlled by the energy barriers, plateaus and wells in a rugged energy landscape (Fig. 2.3 F). As protein-protein complexes are a quaternary protein structure, these protein complexes can be understood in terms of multidimensional energy landscapes as well.

2.2.3 Thermodynamics and kinetics

Protein-protein complexes result from an interplay of multiple weak interactions. Only the sum of multiple interactions designs a stable connection.

Force free molecular interactions A single non-covalent bond between two reaction partners A and B can be described by a two state model



The Arrhenius equation describes the dependence of the rate constant k of such a reaction in terms of temperature T , Boltzmann constant k_B , attempt frequency $\nu_{\text{on/off}}$ and the height of the activation energy barrier $\Delta G_{\text{on/off}}$ ⁹⁶. In equilibrium the constant

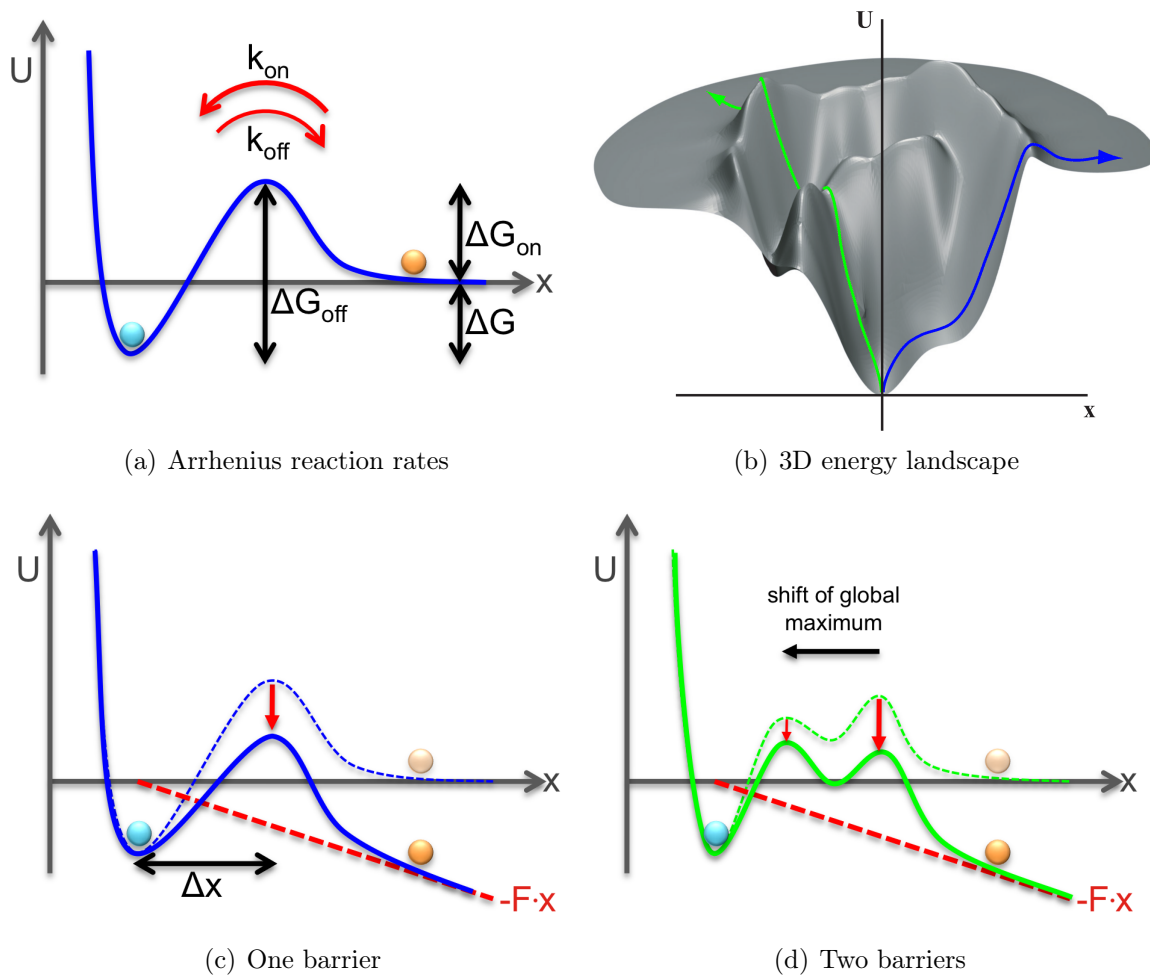


Figure 2.4: This figure shows a 1-dimensional potential energy landscape of a chemical bond (Adapted from⁹⁵). (A) The activation energy of the on/off-reactions are indicated as $\Delta G_{on/off}$ and the binding energy is ΔG . (B) This graph shows the schematic energy landscape of a protein-protein interaction. The green and the blue lines represent different dissociation pathways. (C) Applying a force results in a tilted energy landscape with an effectively reduced barrier height ΔG_{off} . (D) Different potential width of multiple barriers can lead to a shift of the global maximum position in the tilted energy landscape.

binding and unbinding is driven by thermal fluctuations.

$$k_{\text{on}}^0 = \nu_{\text{on}} e^{-\frac{\Delta G_{\text{on}}}{k_B T}} \quad (2.20)$$

$$k_{\text{off}}^0 = \nu_{\text{off}} e^{-\frac{\Delta G_{\text{off}}}{k_B T}} \quad (2.21)$$

The dissociation constant K_D is a measure for the stability of a bond under equilibrium conditions. It is defined as

$$K_D = \frac{[A][B]}{[AB]} = \frac{k_{\text{off}}}{k_{\text{on}}} = \frac{\nu_{\text{off}}}{\nu_{\text{on}}} e^{-\frac{\Delta G}{k_B T}} \quad (2.22)$$

Assuming $\Delta G = \Delta G_{\text{off}} - \Delta G_{\text{on}}$ and $\nu_{\text{off}} \approx \nu_{\text{on}}$ equations 2.20, 2.21 and 2.22 result in

$$K_D = \frac{k_{\text{off}}}{k_{\text{on}}} = e^{-\frac{\Delta G}{k_B T}} \quad (2.23)$$

Bell-Evans-model In many biological and experimental systems, bond dissociation occurs under dynamic load. External forces tilt the energy landscape and thus reduce the energy of the transition state. The Arrhenius equation was extended by Bell to describe this influence of external forces for cell adhesion⁹⁸. The model was further improved by Evans^{99,100}. The effective decrease of the barrier height is determined by the applied Force F times the potential width Δx (red arrow in Figure 2.4 C). For deep potentials the potential width Δx can be assumed to be independent of the applied force. This leads to a force dependent dissociation rate¹⁰¹

$$k_{\text{off}}(F) = \nu_0 e^{-\frac{\Delta G_{\text{off}} - F \cdot \Delta x}{k_B T}} \quad (2.24)$$

$$= k_{\text{off}}^0 e^{\frac{F \cdot \Delta x}{k_B T}} \quad (2.25)$$

with the natural vibration frequency ν_0 . From this dissociation rate the time evolution of existing bonds N_B can be described as

$$\frac{dN_B}{dt} = -k_{\text{off}}(t)N_B(t) \quad (2.26)$$

Integrating eq. 2.26 over time leads to the number of intact interactions N_B :

$$N_B(t) = e^{-\int_0^t dt' k_{off}(t')} \quad (2.27)$$

$$= e^{-\int_0^F df k_{off}(f) \cdot \dot{f}^{-1}} \quad (2.28)$$

It is assumed, that the force can be expressed as a continuous and reversible function of time $F(t)$. The dissociation of molecular interactions are influenced by thermal fluctuations, causing a probability distribution of unbinding forces $p(F)$. It is determined from the number of dissociated bonds $(1 - N_B)$ as follows:

$$p(F) = \frac{d}{dF}(1 - N_B(F)) \quad (2.29)$$

$$= k_{off}(F) \cdot e^{-\int_0^F df k_{off}(f) \cdot \dot{f}^{-1}} \quad (2.30)$$

$$= k_{off}^0 e^{\frac{F \cdot \Delta x}{k_B T}} \cdot e^{-k_{off}^0 \int_0^F df e^{\frac{F \cdot \Delta x}{k_B T}} \cdot \dot{f}^{-1}} \quad (2.31)$$

The most probable rupture force F^* is defined by the maximum condition $\frac{dp(F)}{dF} = 0$. For a force independent loading rate \dot{F} the most probable rupture force can be described as

$$F^*(\dot{F}) = \frac{k_B T}{\Delta x} \ln \left(\frac{\dot{F} \Delta x}{k_B T k_{off}^0} \right) \propto \ln(\dot{F}) \quad (2.32)$$

The most probable rupture force shows a linear dependence on the logarithm of the loading rate $\dot{F} = \frac{dF}{dt}$. Thus, in the case of slow pulling (low loading rates), the system has can be used to determine the natural dissociation rate k_{off} and and the potential width Δx .

2.2.4 Single-molecule AFM force spectroscopy

Multiple experimental techniques are available nowadays to investigate the forces on molecular systems. The most important ones are optical and magnetic tweezers, biomembrane force probe, molecular force balance as well as the atomic force micro-

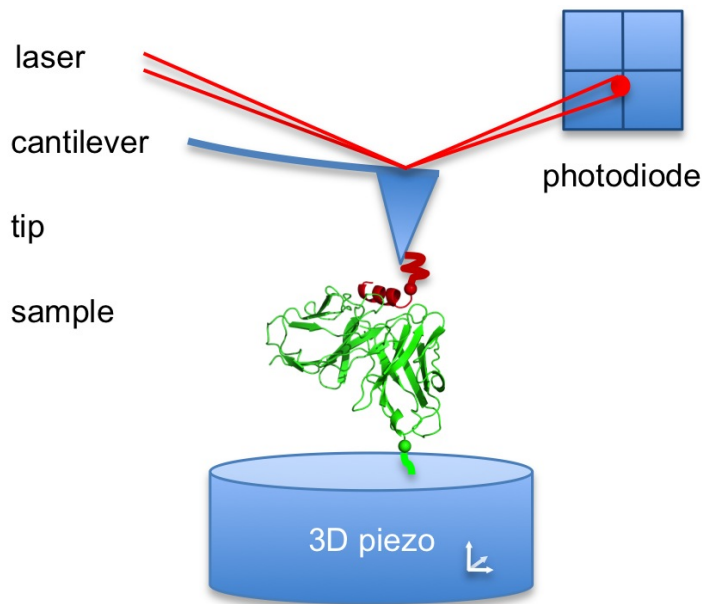


Figure 2.5: The schematic setup of an atomic force microscope. The sample is attached to a piezo for positioning and to the AFM cantilever tip. The bending of the cantilever as a mechanic spring is detected via the reflection of a laser beam on a segmented photodiode.

scope (AFM)^{102–106}. Here, we focus on the AFM (Section 3.2) as a high-sensitive single molecule force spectroscopy technique. It measures and applies forces in the physiological picoNewton range with spacial subnanometer resolution to detect unbinding, unfolding and stretching forces of single (bio)molecules^{33,34,37,107–109}.

A schematic AFM setup is shown in Figure 2.5. The cantilever, a microscopic small force sensor is the key-part of the AFM, acting as a sensitive force sensor. The cantilever bending is detected by a reflected laser beam on a segmented photodiode. It is described as a linear spring $F = sx$. The spring constant s is determined by the cantilever stiffness and the displacement x , measured by the deflection.

For the examination of molecular complexes, one is bound to the cantilever probe tip and the other is immobilized on a surface mounted on the piezo. For measurement of the interactions, the cantilever tip is brought into contact with the surface, allowing

the molecules to interact. Upon retraction of the cantilever, the applied forces are moderated by the piezoelectric actuators. Generally, the forces are applied with either a constant velocity of the retracting cantilever or as constant forces controlled by a force feedback loop.

Force-extension curves are recorded by the AFM. From these, rupture forces (the force at which a specific interaction dissociates) and rupture lengths (distance at which the interaction dissociates) are determined. The corresponding loading rate is determined from the slope of the force versus time curve at the moment of the rupture event.

2.2.5 Single-molecule force probe MD simulations

Even though the three approximations in Section 2.1 allow the simulations of molecular systems on the nano- to microsecond time scale, many processes in biology require longer time scales. As mentioned in the introduction, multiple approaches are available to gain insight into dynamics on a longer time scale using MD simulations. In this thesis, force probe simulations with two different pulling protocols are used: constant velocity and constant force.

As discussed in Section 2.2.3, applied forces speed up the simulated protein-protein dissociations to make them accessible with MD simulations and closely mimic the AFM experiments from the previous Section 2.2.4. For this, one or more groups of atoms, so called pull groups, are enforced to move along a predefined pulling direction. Furthermore, force probe simulations give insight into protein complex reaction which are either physiologically relevant (integrin-talin complex in Section 4) or are compared to experiments including force probing (AFM experiments on the antibody-peptide complex in Section 3.2).

Constant velocity

For constant velocity probing, a harmonic potential V_{spring} is added to the atoms of the pull group.

$$V_{\text{spring}}(t) = \frac{s_0}{2}[R(t) - R_{\text{spring}}(t)]^2 \quad (2.33)$$

where s_0 is the spring constant, $R(t)$ is the position of the COM of the pulled atoms and $R_{\text{spring}}(t)$ is the position of the the spring. The force

$$F(t) = s_0[R(t) - R_{\text{spring}}(t)] \quad (2.34)$$

is applied by moving the spring position $R_{\text{spring}}(t)$ with constant velocity v_{spring} along a chosen reaction coordinate

$$R_{\text{spring}}(t) = R_{\text{spring}}(t = 0) + v_{\text{spring}}t. \quad (2.35)$$

For weak springs, the loading rate $\dot{F} = \frac{dF_{\text{spring}}}{dt} = s_0v_{\text{spring}}$ is directly proportional to the pulling velocity v_{spring} . The pulling force F_{spring} on the COM of a group of atoms is redistributed mass weighted to the individual atoms.

Constant force

In constant force mode, either a linear potential is applied to tilt the energy landscape in the direction of the reaction coordinate (Fig. 2.4) or the force is added directly to the calculated forces for each atom of the pull group. The resulting time-independent tilt of the energy landscape permits a direct insight into the dissociation kinetics of the probed system by looking at the unfolding or dissociation lifetimes of the system.

2.3 Molecular rotors

2.3.1 Basic principles

Since the formulation of statistical physics by Maxwell and Boltzmann, the dream of many scientists was to selectively use fluctuations for driving systems. In this context it is important to keep the second law of thermodynamics in mind.

Second law of thermodynamics

The change of entropy dS in a closed system is related to the change in heat δQ and the temperature T via

$$dS \geq \frac{\delta Q}{T} \quad (2.36)$$

where the equality holds for reversible and the inequality for irreversible processes. In the formulation according to Carnot:

"No series of processes is possible whose sole result is the transfer of energy as heat from a thermal reservoir and the complete conversion of this energy to work."¹¹⁰

Langevin dynamics

The basic behavior of a rotor is approximated by a one dimensional system interacting with a thermal bath according to a Langevin equation¹¹¹.

$$I \frac{d^2\theta}{dt^2} + \Gamma \frac{d\theta}{dt} - \frac{\delta U}{\delta\theta} = \xi(T, t). \quad (2.37)$$

with time t , moment of inertia I , the rotation angle θ and friction constant Γ . ξ is a stochastic torque representing the thermal fluctuations of the system.

Fluctuation-Dissipation theorem

The stochastic interaction of the rotor with the bath is divided into two terms¹¹¹. First, the purely random stochastic torque ξ has a zero average mean $\langle \xi \rangle = 0$ and is rapidly varying. Second, a slower, velocity dependent friction term $\Gamma \frac{d\theta}{dt}$ influences the system if the effective average rotation velocity $\frac{d\theta}{dt} \neq 0$. Friction constant Γ and stochastic torque $\xi(T, t)$ are correlated by the fluctuation-dissipation theorem¹¹¹

$$\Gamma = \frac{1}{k_B T} \int_0^\infty \langle \xi(t_0) \xi(t_0 + t) \rangle dt. \quad (2.38)$$

This fluctuation-dissipation theorem connects the energy dissipated from the rotor by friction to the fluctuations of the bath. It connects the friction to an autocorrelation of the stochastic noise term ξ weighted by the inverse thermal energy.

2.3.2 Classification of rotors

A multitude of rotors is existing. Here, I present a classification of rotors according to the review of Kottas et al.¹¹¹.

Definition

The molecular rotor consists of a stator and a rotator which can rotate against each other. The part with the larger moment of inertia is commonly regarded as the stator. The axle of the rotor carries the rotator and the rotator turns about the axle. An axle is not required for a rotor to function. For example, surface mounted R-rotors don't have an axle (see below).

Classification by structure

The structure of a rotor can be classified by different criteria summarized in Table 2.1. This classification occurs according to the chemical bond between rotator and stator, the environment of the rotor, existence and chemical nature of the axle and in case of a surface-mounted rotor the type of its mounting. These criteria are taken from the review¹¹¹.

Table 2.1: Rotor classification by structure according to review Kottas et al.¹¹¹

<i>criteria</i>	<i>description</i>
chemical bond	<ul style="list-style-type: none"> • covalently bound rotator and stator • non-covalently bound rotator and stator
environment	<ul style="list-style-type: none"> • free in solution or vapor • inside solids • surface-mounted
type of surface mounting	<ul style="list-style-type: none"> • R-rotor: rotator bound to the surface (no axle, surface=stator) • RS-rotor: stator is fixed on the surface
rotation axis	<ul style="list-style-type: none"> • free in space • perpendicular to surface (azimuthal rotor) • parallel to surface (altitudinal rotor)
chemical nature of the axle	<ul style="list-style-type: none"> • single bond • double bond (highly hindered) • triple bond • metal ion • no axle (e.g. R-rotor)

Classification by function

Not only structure defines a rotor, but also its function (Table 2.2). As for the protein-protein interactions, the rotor motion can be described by its energy landscape (see Section 2.2.2). The rotor dynamics depend on the interplay of the various energies in a system. The energy contributions can be divided into environmental (e.g. thermal energy), structural (e.g. torsional barriers defined by the structure) and combined structural/environmental (e.g. dipole coupling) contributions. The rotor motion can

be classified as driven or random, depending on the effect of the external forces (see Section 2.3.3).

Table 2.2: Rotor classification by function according to review Kottas et al.¹¹¹

<i>criteria</i>	<i>description</i>
energy contributions	<ul style="list-style-type: none"> • environmental (e.g. temperature) • structural (e.g. torsional barrier) • environmental and structural interaction (e.g. electric dipole coupling to applied electric field)
barrier height	<ul style="list-style-type: none"> • low compared to $k_B T$ - frequent reorientation • high compared to $k_B T$ - only driven rotation
rotation mechanism	<ul style="list-style-type: none"> • driven/deterministic - external force dominates dynamics • random/non-deterministic - thermal energy dominates dynamics
driven rotation	<ul style="list-style-type: none"> • forces caused by external field • forces due to steric interactions
random rotation	<ul style="list-style-type: none"> • Brownian motion • Thermally activated hopping

2.3.3 Rotor behavior

Potential energy landscape

The potential energy landscape U has two main contributions: the internal torsional potential U_{tor} and the interaction energy due to external fields U_{Coul} . The internal torsional potential describe the potential energy versus the rotation angle in the absence of external fields. A typical model is a sinusoidal description with n potential minima and a characteristic amplitude A

$$U_{\text{tor}} = A \cos(n\theta). \quad (2.39)$$

The order of the symmetry of rotator and stator often define the number of po-

tentials as their least common multiple. For example, a three-fold symmetric stator and a two-fold symmetric rotator have a internal torsional potential with six minima (e.g. trans-rotor on gold in Chapter 5). In this thesis, the interaction energy is caused by the external electric field acting on the partial charge distribution of the rotator. Another example of interaction energy would be the orientation of a dipole along a rotating electric field¹¹².

Depending on the relative strength of the thermal energy, the torsional barrier heights and the external field, three typical types of motion can be described. For a dominating external field, the rotor shows driven motion. Otherwise, the rotor is subject to random motion. For truly random motion the average change in angle is zero ($\langle \theta \rangle = 0$), but random rotors can achieve directional rotation. Random motion is generally subdivided into Brownian motion dominated by the thermal energy contribution and hindered motion dominated by the intrinsic torsional barriers of the rotor. In the following all three types of rotor motion are described.

Driven motion

For a driven rotor, the external forces dominate the dynamics of the rotor. The external potential V is larger than the magnitude of the internal torsional barriers $2A$ and the thermal energy $k_B T$ ($V > k_B T$ and $V > 2A$). The rotor can be driven by forces caused by external fields or steric interactions. Three types of motion can be distinguished for a driven rotor¹¹¹:

- synchronous motion
- thermal librations within the potential well
- thermally activated hops to neighboring potential wells

With decreasing strength of the external driving source or increasing temperature, the dominating deterministic synchronous rotation decreases and the other motions become more important. If the frictional response of the system dominates over the externally driven torque ($\frac{\delta V}{\delta t} < \Gamma \frac{d\theta}{dt}$), then the response of the rotor is a randomly

driven motion and differs for each cycle of the external field. Still, an effective directional rotation is caused by the external field.

Brownian motion

In the Brownian motion regime the motion of the rotor is dominated by thermal energy. Using $\frac{dU}{d\theta} \approx 0$ to solve eq. 2.37 leads to

$$\langle \theta^2 \rangle = \frac{2k_B T}{\Gamma} \left[t - \frac{I}{\Gamma} (1 - e^{-\Gamma t/I}) \right]. \quad (2.40)$$

At long time scales $t \gg \frac{I}{\Gamma}$ this reduces to a random walk.

$$\langle \theta^2 \rangle = \frac{2k_B T}{\Gamma} t \quad (2.41)$$

For small time scales, an expansion of eq. 2.40 by $\frac{\Gamma}{I}t$ yields a motion with an angular velocity $\sqrt{\frac{k_B T}{I}}$ described by

$$\langle \theta^2 \rangle = \frac{k_B T}{I} t^2. \quad (2.42)$$

Small external fields can cause a preferred direction in this regime.

Hindered motion

Hindered motion is caused if the barrier height $2A$ of the intrinsic torsional potential U_{tor} are dominating ($2A > k_B T$ and $2A > V$ and $2A > \Gamma \frac{d\theta}{dt}$). The motion of the rotor is then dominated by thermal librations within the well of the intrinsic torsion potential. Thermally activated hops can move the system from one well to another with the probability $P \propto e^{-\frac{2A}{k_B T}}$. This gives rise to the rate of thermally activated hopping k^0 analog to eq. 2.20

$$k^0 = \nu_0 e^{-\frac{2A}{k_B T}} \quad (2.43)$$

with the natural vibration frequency ν_0 . Using a harmonic small angle estimate on the sinusoidal torsional potential $U_{\text{tor}} = A \cos(n\theta)$ with n wells and a spring constant s , assuming $F = -s\theta$ and $\sin \theta \approx \theta$, results in

$$\frac{dV}{d\theta} \equiv -s\theta = -nA \sin(n\theta) \approx -n^2 A \theta \quad (2.44)$$

$$s = n^2 A \quad (2.45)$$

with

$$\nu_0 = \sqrt{\frac{s}{I}} = \sqrt{\frac{n^2 A}{I}}. \quad (2.46)$$

Small rotors show characteristic frequencies on the order of ~ 1 THz¹¹³.

3

Force-Based Analysis of Multidimensional Energy Landscapes

3.1 Aims

- Comparison of steered molecular dynamics simulation results with AFM single-molecule force experiment results
- Examine importance and impact of force application as a vectorial tool and with different loading rates to explore the energy landscape of a protein complex
- Identify the dependence of the unbinding pathway on the direction of the applied force for the antibody fragment-peptide complex
- Study the response of the barnase-barstar complex to enforced dissociation in atomistic detail

3.2 Antibody-Antigen Interaction

3.2.1 Biological background

Our immune system is a highly complex and adaptive protection mechanism against infections. Antibodies play an essential part in the adaptive immune response. They make up to 20 percent of the total amount of proteins in the blood plasma. The antibodies are collectively called immunoglobulins (Ig) and are produced by B-cells. Each B-cell produces only a single species of antibody with unique antigen binding sites⁷⁹. Here, we focus on the simplest Y-shaped antibody type, the IgG molecules. Each IgG consists of two heavy and two light chains which are connected by disulfide bonds. At the short arms of the Y-shaped antibody there are two variable domains defined by hyper-variable regions in both the heavy and light chain. This variable region is called Fv fragment and contains the complete antigen binding site. The recombinant single chain antibody Fv fragment (scFv) H6 is used in our work¹¹⁴. It binds a truncated GCN4-p1 leucine zipper $Y_1HLENEVA_8RLKK_{12}$. The crystal structure (PDB: 1P4B)¹¹⁵ of this antibody-antigen complex is well known.

3.2.2 Summary

We examine the influence of probing forces on the dissociation pathways of an antibody binding its 12 amino acid antigen peptide (Fig. 3.1). The forces were applied using steered molecular dynamics (SMD) simulation and single-molecule AFM force spectroscopy. The crystal structure (PDB: 1P4B)¹¹⁵ contains the 12 amino acid antigen. Three different attachment points are chosen, the N-terminus (setup N), the C-terminus (setup C) and the middle of the peptide at position 8 (setup M). The same attachment points are probed by AFM and SMD.

The AFM measurements determine the loading rate dependence of the most probable rupture forces (Fig. 4 in Ref. P1). From these, different potential widths Δx and dissociation rates k_{off} are extracted for all three setups according to eq. 2.32 (Table 1 in Ref. P1). Setup N is the least stable ($k_{\text{off}} = 16.9 \cdot 10^{-3} \text{ s}^{-1}$) with the smallest

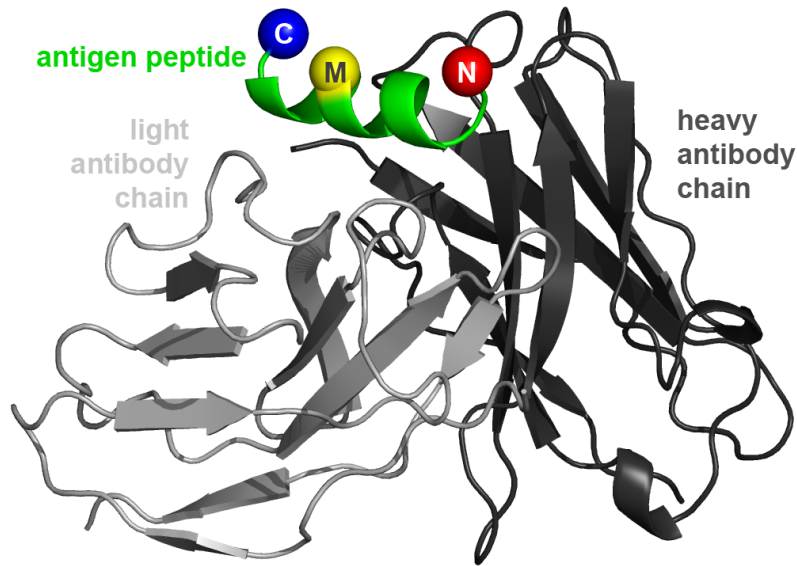


Figure 3.1: This is the antibody scFv H6 crystal structure binding the truncated GCN4-p1 leucine zipper. The light chain is indicated in light grey and the heavy chain in dark grey. The antigen is shown as yellow helix with the attachment points for the force probing shown as spheres (C,M and N from left to right).

potential width ($\Delta x^N = 0.82$ nm). The dissociation of Setup C is 13 times slower ($k_{\text{off}} = 1.3 \cdot 10^{-3} \text{ s}^{-1}$) and has a 23% larger potential width ($\Delta x^C = 1.10$ nm). Setup M shows intermediate values for dissociation rate ($k_{\text{off}} = 7.6 \cdot 10^{-3} \text{ s}^{-1}$) and potential width ($\Delta x^M = 0.95$ nm).

The SMD simulations show different unbinding pathways in atomistic detail for all three setups (Figs. 7-9 and Table 2 in Ref. P1). In all setups the peptide is zipped off starting from the force attachment point. For setup M this results in a double zipper dissociation (Fig. 6 in Ref. P1). For each setup, two main interactions with comparable rupture forces were identified. However, all setups share a pathway-independent main dissociation barrier in the simulation. This barrier can be attributed to the rupture of the hydrogen bond between the peptide's $\text{GLU}^{O\epsilon-6}$ and the heavy chain's backbone hydrogen $\text{GLY}^H\text{-H40}$ (Figs. 7c, 8b and 9c in Ref. P1).

In the setups N and C, the potential widths ($\Delta x^N, \Delta x^C$) are in good agreement with the first rupture lengths r of the SMD simulations ($r_1^N = 0.88$ nm and $r_1^C = 1.03$ nm) (Fig. 10 in Ref. P1). Hence, the AFM experiments probe the first barrier of the system attributed to different interactions. For setup N, the hydrophobic contact of the peptides LEU-3 with the antibody's light chain TYR-L40 dissociates. In setup C, the hydrogen bond between the peptide residues VAL-7 and LEU-10 is broken and the peptide's C-terminal helix loop opens. The SMD simulations identify a second barrier for each setup. Their longer rupture lengths ($r_2^N = 1.72$ nm and $r_2^C = 1.50$ nm) indicate larger potential widths. The enforced tilt of the energy landscape reduces the outer barriers more strongly. This indicates that the AFM is measuring the different inner barriers. From the higher rupture forces and the longer rupture lengths of the first barrier in setup C it can be assumed to have a higher first barrier than setup N. This results in a qualitatively lower dissociation rate for setup C ($k_{\text{off}}^C < k_{\text{off}}^N$, see Fig. 10 in Ref. P1).

Concluding, the comparison of the probed energy barriers of both methods (AFM and SMD) show an excellent agreement even though the loading rates of the SMD simulations exceeded those of the AFM experiments by orders of magnitudes. The direction of the applied forces in single-molecule force spectroscopy clearly define the preferred dissociation pathway on a multidimensional energy landscape of the protein complex.

3.2.3 Publication P1

Julia Morfill, [Jan Neumann](#), Kerstin Blank, Uta Steinbach, Elias Puchner, Kay E. Gottschalk, Hermann E. Gaub.

Force-Based Analysis of Multidimensional Energy Landscapes: Application of Dynamic Force Spectroscopy and Steered Molecular Dynamics Simulations to an Antibody Fragment-Peptide Complex.

J Mol Biol (2008) 381, pp. 1253-66

3.3 Barnase-Barstar

3.3.1 Biological background

Ribonucleases are enzymes that catalyze the degradation of RNA into smaller components. The bacterium *Bacillus amyloliquefaciens* excretes the ribonuclease (RNase) barnase for food degradation and protection against predators and competitors¹¹⁶. Since barnase has a lethal effect on all unprotected cells, the *Bacillus amyloliquefaciens* developed the inhibitor barstar for self-protection. The crystal structure (PDB: 1BRS) shows that a barstar α -helix blocks the active site of the barnase¹¹⁷. The very high association rate constant of the complex ($k_{\text{on}} = 10^8 \text{s}^{-1} \text{M}^{-1}$)¹¹⁸ is achieved by electrostatic steering^{119–121}. The optimal association pathway involves a region near the RNA binding site^{122,123}. An overlap of the association and dissociation pathways has been suggested from rigid-body Brownian dynamics simulations with implicit solvent¹²³.

3.3.2 Summary

The antibody-antigen project shows clearly that forces can be used to examine the energy landscape of a protein complex dissociation in experiment and simulation. In this project we use SMD simulations to show that the variation of force parameters can be used as a differential force assay. We examine additional variations of the geometry and velocity of force application (Fig. 1 in Ref. P2). These allow to determine the relative stability of different protein regions within the complex against each other. For this project, we choose the small and fast binding barnase-barstar complex to optimize the computational effort¹¹⁷. In the past, the association of the barnase-barstar complex has been studied extensively under equilibrium conditions^{118–123}. However, our simulations contribute new insight into the dynamic response of the complex under non-equilibrium conditions. We can switch the main dissociation pathway of a protein complex from unfolding to several unbinding pathways. In setup 1, the influence of the viscous drag compensating the pulling force is increased with increasing

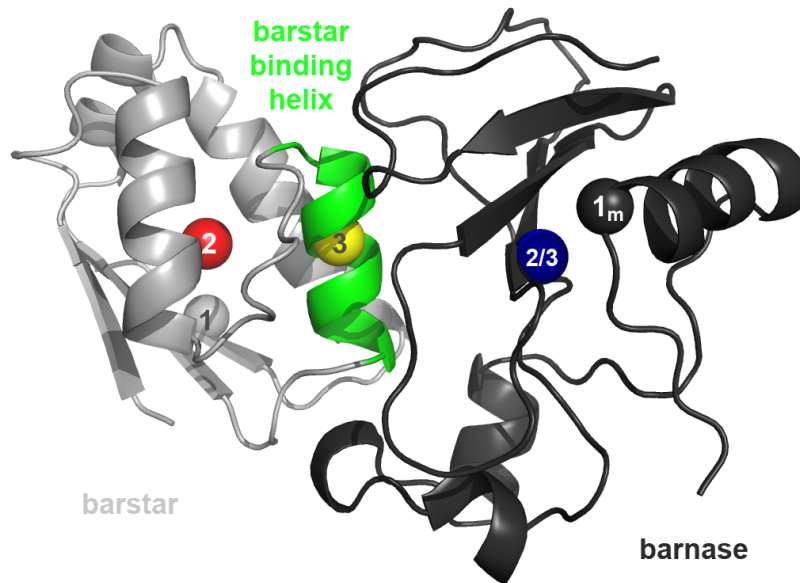


Figure 3.2: This is the barnase-barstar complex crystal structure (PDB: 1BRS)¹¹⁷. The dark grey molecule is the barnase RNase, the light grey is the barnase with a green highlighted binding helix. The light and dark grey spheres are the force attachment points for the end-to-end pulling in setups 1 and 1_m . The red sphere represents the COM of the complete barstar pulled in setup 2, while the yellow sphere represents the COM of barstar's binding helix pulled in setup 3. The blue sphere represents the COM of the barnase locally restrained in setups 2 and 3.

pulling velocity. Therefore, it is important from which side the protein complex is probed (Fig. 3A in Ref. P2). Two main pathways can be identified: the energetically more costly shearing of barstar's β -sheet and the cooperative zipper-like unbinding of the barnase's N-terminal α -helix (Fig. 6 in Ref. P2). Given enough time in the slow pulling setups, the system prefers the unbinding of barnase's α -helix. A rapid change of the system lacks enough time to relax orthogonally to the reaction coordinate and the lability instead of the stability of the system is tested. Thus, fast pulling can be used to study the barriers in the energy landscape.

In setups 2 and 3, barnase's center of mass (COM) is restrained. In setup 2, barstar's

COM is pulled away from barnase. This shows, that the intramolecular stability of barstar's conformation is less stable than the intermolecular binding to the barnase. This is reasonable since the evolutionary pressure for the survival of the bacterium based on a blocked barnase is dominating against the conformational stability of the inhibitor as long as it still blocks (Fig. 3B in Ref. P2). The direct unbinding of the proteins is achieved by force application to the COM of the barstar's binding helix in setup 3 (Fig. 3C in Ref. P2).

Summarizing, the barnase-barstar simulations show that velocity and geometry have a strong impact on the development of the system. For an atomistic understanding of unbinding or unfolding pathways a variety of force protocols needs to be tested.

3.3.3 Publication P2

Jan Neumann, Kay E. Gottschalk.

The Effect of Different Force Applications on the Protein-Protein Complex Barnase-Barstar.

Biophys J (2009) Vol. 91(6) pp.1687-99

4

Force response of the integrin-talin complex

4.1 Aims

- Analyze the integrin activation mechanism by talin binding focussing on the disruption of the salt bridge (β_3 -D723 - α_{IIb} -R995) which stabilizes the integrin's TM helix interactions
- Study the dependence of the integrin-talin complex on the direction of force response probed parallel and normal to the membrane
- Investigate the design principles of force resistance by combining mechanical force resistance and natural sensitivity to directional probing

4.2 Biological background

4.2.1 Motivation

Protein-protein interactions choreograph the life on the cellular level. Integrins are the major cell adhesion receptors of cells⁴². They were optimized by evolution as a force resistant and functional interface between inside and outside of the cell. Design principles combining functional two-way signaling and mechanical force resistance could improve bioengineering of future nanoscale machinery. The understanding of integrins as major cell adhesion receptors could also lead to improved medical devices such as implant coatings resulting in less immune rejection. Integrins are important not only in cellular processes from cell migration, proliferation to apoptosis, but are also important targets for pharmaceutical research in fighting inflammation reactions¹²⁴, multiple sclerosis¹²⁵, tumors^{126,127} or HIV¹²⁸. The importance of the integrins in basic research is highlighted by the integrin being the molecule of the month February 2011 of the international most important structure database www.pdb.org.

4.2.2 Integrin

Integrins are heterodimeric transmembrane (TM) adhesion receptors transducing bi-directional signals and forces through the membrane^{42,129}. They are composed of two subdomains (α and β). In humans, 18 known α and 8 known β units combine to at least 24 functional adhesion receptors. Both subdomains of the integrin consist of a short cytoplasmic tail, a single TM helix and a large extracellular domain. The size of the extracellular integrin domain contains about 1000 amino acids in the α - and 750 in the β -domain¹³⁰⁻¹³².

The extracellular domain of the integrin has two main conformations - a passive bent switchblade and an active open switchblade (shown in Fig. 4.1)¹³⁴. In the passive form, the TM helices are tightly packed¹³⁵⁻¹³⁷. The α - and β -TM-helices interact via an outer and an inner membrane clasp⁵⁰. The outer membrane clasp stabilizes the TM crossing via a glycine-packing. The inner membrane clasp consists of a hydrophobic

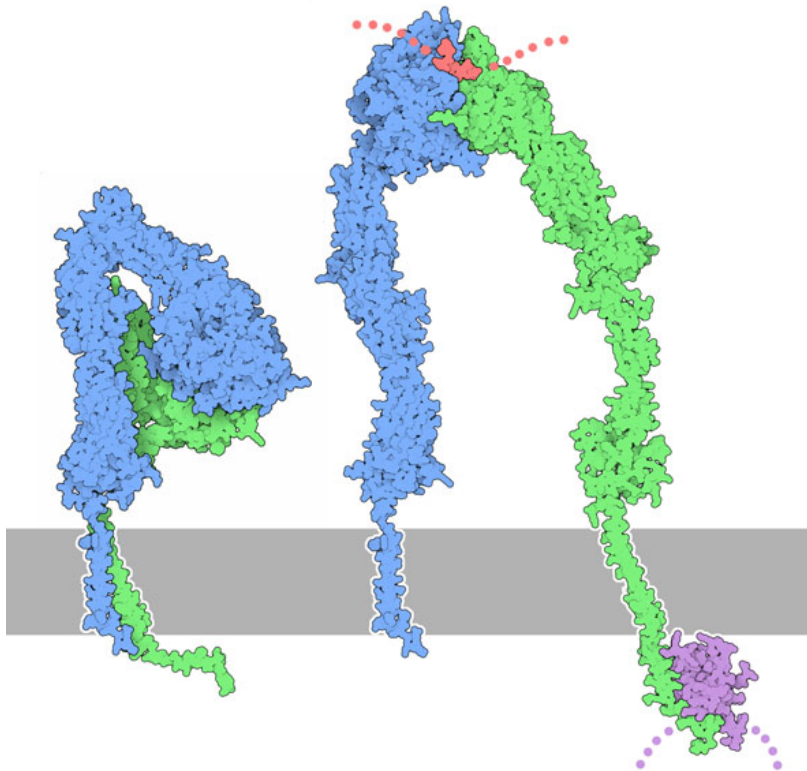


Figure 4.1: This figure shows the α (blue) and β (green) subunits of the integrin in a passive (left) and an active (right) conformation. The bound talin is shown in violet and the bound short fibrinogen peptide is shown in red. The figure was designed by David S. Goodsell and published by RCSB PDB¹³³

core (α_{IIb} -F992/F993 - β_3 -W715) and a salt bridge (α_{IIb} -R995 - β_3 -D723)

Integrin activation is accompanied by separation of the α - and β -TM helices¹³⁸. The dissociation of the inner membrane clasp initiates an inside-out signaling pathway activating the integrin. This activation is caused by talin binding to the integrin's cytoplasmic β -tail^{48,131,139,140}. The separation of the extracellular integrin legs causes the outside-in signaling by initiating the dissociation of the outer membrane clasp^{50,141,142}.

Activation and deactivation of integrins can also be caused by applied forces^{41,143}. Whether this requires vertical⁴¹ or lateral forces¹⁴³ is currently under discussion and motivates the normal and parallel force applications in our project.

4.2.3 Talin

Talin is a special ligand out of the large variety of molecules that bind the integrin, the so called integrin adhesome of more than 155 proteins¹⁴⁴. Talin binding with its FERM domain to the cytoplasmic β -tail of the integrin is the essential last step in the inside-out activation of the integrins^{139,145,146}. Additionally, talin binds actin with its rod domain¹⁴⁷. Thus, talin acts as a force clamp between integrin and cytoskeleton. It forms the initial force transmitting link between the extracellular matrix (ECM) and the intracellular actin network⁴⁷. Figure 1A in Ref. P3 shows a scheme of this force propagation pathway. Talin completes the mechanical connection from the outside of the cell to the cell's mechanical carcass, the cytoskeleton. Additionally, the positively charged residues of the FERM domain bind to the cell membrane and enhance the integrin activation^{51,140,148,149}.

4.3 Summary

The integrin-talin interface is essential in the activation of the integrin and in the early stages of the force transmission from the ECM to the intracellular cytoskeleton. Here, we study the effect of forces on the initial integrin-talin complex by simulating the integrin-talin interface region in the recently published complex structure of the integrin β_{1D} binding to the talin-2 FERM F3 domain⁵⁰.

A 100 ns long equilibration of this structure results in a stable complex with a root mean square deviation of the C_{α} atoms from the initial structure of ~ 0.2 nm (Fig. 2A in Ref. P3). A clustering algorithm identifies the most representative structure of the dominating integrin-talin conformation. The dominating cluster represents 47% of all frames and three times more than the second largest. From the analysis of the

structure and the root mean square fluctuations of the amino acids in equilibrium, three modular binding regions with more flexible interconnects are identified (Table 4.1 and Fig. 3 in Ref. P3). The importance of these tight binding modules is confirmed by a high evolutionary conservation identified using a multiple sequence alignment.

Table 4.1: This overview lists the three modular binding sites of the integrin we identify and describes their interaction sites.

<i>integrin binding region</i>	<i>interaction type</i>
helix ⁷⁶³ F...E ⁷⁶⁹	<ul style="list-style-type: none"> • hydrophobic interactions of β_{1D}-F⁷⁶³ and β_{1D}-F⁷⁶⁶ • hydrogen bonds of the charged amino acids β_{1D}-D⁷⁵⁹, β_{1D}-E⁷⁶⁷ and β_{1D}E⁻⁷⁶⁹
tryptophan W ⁷⁷⁵	<ul style="list-style-type: none"> • deep hydrophobic talin binding pocket • stabilization via a cation-π interaction possible
NPxY motif	<ul style="list-style-type: none"> • hydrogen network of β_{1D} -⁷⁸⁰ NPIY⁷⁸³

The direct environment of our simulated integrin-talin complex fragment is generated (Fig. 1B in Ref. P3). We align our long time equilibrated integrin-talin complex fragment to the adjacent structures including the full talin FERM domain and the integrin's α -/ β -TM helix bundle⁵⁰⁻⁵². Surprisingly, no steric disturbance resulted from the α_{11b} -cytoplasmic tail and the talin FERM domain, both being bound to the integrin β -tail at the same time. From low force pulling experiments we identify the N-terminal integrin helix near the membrane as the first secondary structure element to unfold. We propose that this conformational change disrupts the salt bridge of the inner membrane clasp (Fig. 9 in Ref. P3). The mechanical stress resulting from the rotation of the talin head by $\sim 20^\circ$ during its binding to the cell membrane might already be sufficient to cause these forces required for the integrin activation⁵¹.

To identify the force response of the integrin-talin complex, constant force MD simulations ranging from 20 - 500 pN are performed with two perpendicular pulling directions. The N-terminal C $_{\alpha}$ of the β_{1D} integrin is pulled either normal or parallel to the putative plane of the cell membrane and away from the talin-2 F3 FERM domain. The integrin-talin COM-COM distance is evaluated as reaction coordinate.

Dissociation of the complex within the simulation time of 20 ns starts at 200 pN for parallel forces and at 400 pN for normal forces. Thus, the mechanical force resistance of the integrin-talin complex parallel to the membrane is weaker than that normal to it.

To gain an atomistic insight into the dissociation of the complex, a pathway map is generated. A peak detection algorithm determines (meta)stable intermediate states from the distance distributions of each force and each probing direction. The structures of each state are clustered and a dissociation pathway map is generated from the representative cluster conformations (Figs. 6 and 7 in Ref. P3). From these maps, the dissociation pathways for normal and parallel pulling are clearly distinguishable. The three modular binding regions mentioned above unbind characteristically for each setup. The main difference in the dissociation is the formation of an intermolecular β -sheet which occurs only for normal pulling (Fig. 8 in Ref. P3). This force induced strengthening of the complex causes the higher normal force resistance. Ubiquitin is a prominent example for such a direction dependence of force resistant β -sheets^{30,150}.

Additional end-to-end simulations without talin restraint show a rotation of the complex. This reorientates the complex to experience the pulling forces along its more force resistant axis corresponding to the force axis of the normal force pulling setup.

Summarizing, we clearly show the direction dependence of the mechanical force resistance in the integrin-talin complex. A force induced complex strengthening is attributed to the formation of an intermolecular β -sheet. A complex reorientation to allow this β -sheet formation is identified. Additionally, the steric compatibility of both integrin α -tail and talin binding to the integrin β -tail was shown. An extension of the integrin activation model¹⁴⁰ is proposed to require the unfolding of the membrane proximal integrin α -helix loop.

4.4 Outlook

As described, the talin integrin complex is the initial force resistant connection between the cell's cytoskeleton and the extracellular matrix. The force induced strengthening of the integrin-talin complex should in the next step be studied including the TM integrin, a cell membrane and possibly the talin-2 F2 FERM domain. The introduction of mutations which prevent the formation of the force-induced beta-sheet at the interface can yield additional insight into the mechanical stability of the complex. Ultimately, the goal is to simulate the complete integrin activation with talin, integrin and a membrane long enough to identify a conformational change of the extracellular integrin domain from passive to active state. Additionally the force transmission pathway in atomistic detail should be identified including the aforementioned system, actin and an ECM ligand.

4.5 Publication P3

Jan Neumann, Kay E. Gottschalk

The Integrin-Talin Complex under Force.

(submitted to PLoS Comput Biol)

5

Controlling molecular rotation on gold

5.1 Aims

- Switching and driving of bidirectional molecular rotation on a gold surface by Terahertz electric fields
- Understanding the design principles for effective directionality of a non-deterministic rotor on the nanoscale
- Description of the rotor behavior within a theoretical framework

5.2 Motivation

In nature molecular rotors are essential building blocks of many molecular machines and brownian motors¹⁵¹. The F1-ATP synthase uses rotations to drive the chemical fuel production of adenosinetriphosphate (ATP)^{53,152}. The mechanism of a bacterial flagellum moves or reorientates the bacterium depending on the direction of its rotation^{54,153}. But not only nature builds molecular rotors, also man-made nanodevices are in desperate need for understanding molecular rotation to improve future artificial designs.

In this field, unidirectional rotation¹⁵⁴ and electrically driven rotors^{112,155} have been major research topics. The idea to drive a molecular rotor as a parametric pump was first introduced by Horinek et al. to describe a sub-harmonic rotor response¹⁵⁵. This deterministic rotor is subject to a changing energy landscape. The electric field is directly coupling to the dipole moment of the rotor. The position of the energy barriers and energy wells exchange due to the oscillatory driving. In the slow adiabatic limit, the rotor follows exactly the minima positions and rotates at the same frequency as the external field. In the parametrically driven mode, the field is changing slightly faster than the rotor can respond. Thus, it rotates every second cycle and is reflected at a forming barrier every other cycle.

5.3 Summary

In our simulations a diethylsulfid (DES) rotor on a gold (111) surface is simulated (Fig. 5.1 A). It was modeled analogously to low temperature STM experiments in which the rotor behavior was experimentally observed on a single-molecule level⁵⁷. The flexibility of the molecular rotors and the effective surface interaction are important for the rotational dynamics of this system¹⁵⁶. The observed temperature fluctuations even at low temperatures make it a simple and dynamic system to study non-deterministic driving of molecular rotation and allow extensive sampling in computer simulations. We chose to examine the DES rotor by means of Molecular Dynamics (MD) simulations and its behavior under the influence of externally applied static and oscillating electric fields. It is a surface-mounted azimuthal R-rotor bound to the gold via a sulfur gold bond (Table 2.1).

Studying the basics of rotation in non-deterministic systems is essential for further development of nanotechnology. Our research aims at highly efficient artificial rotors driven classically by externally controlled devices such as parallel electric fields of long wavelength infrared light. Here, we show how to control the rotational behavior of a simple surface mounted rotor using Terahertz electric fields perpendicular to the surface. Furthermore, we introduce a general theoretical framework to model

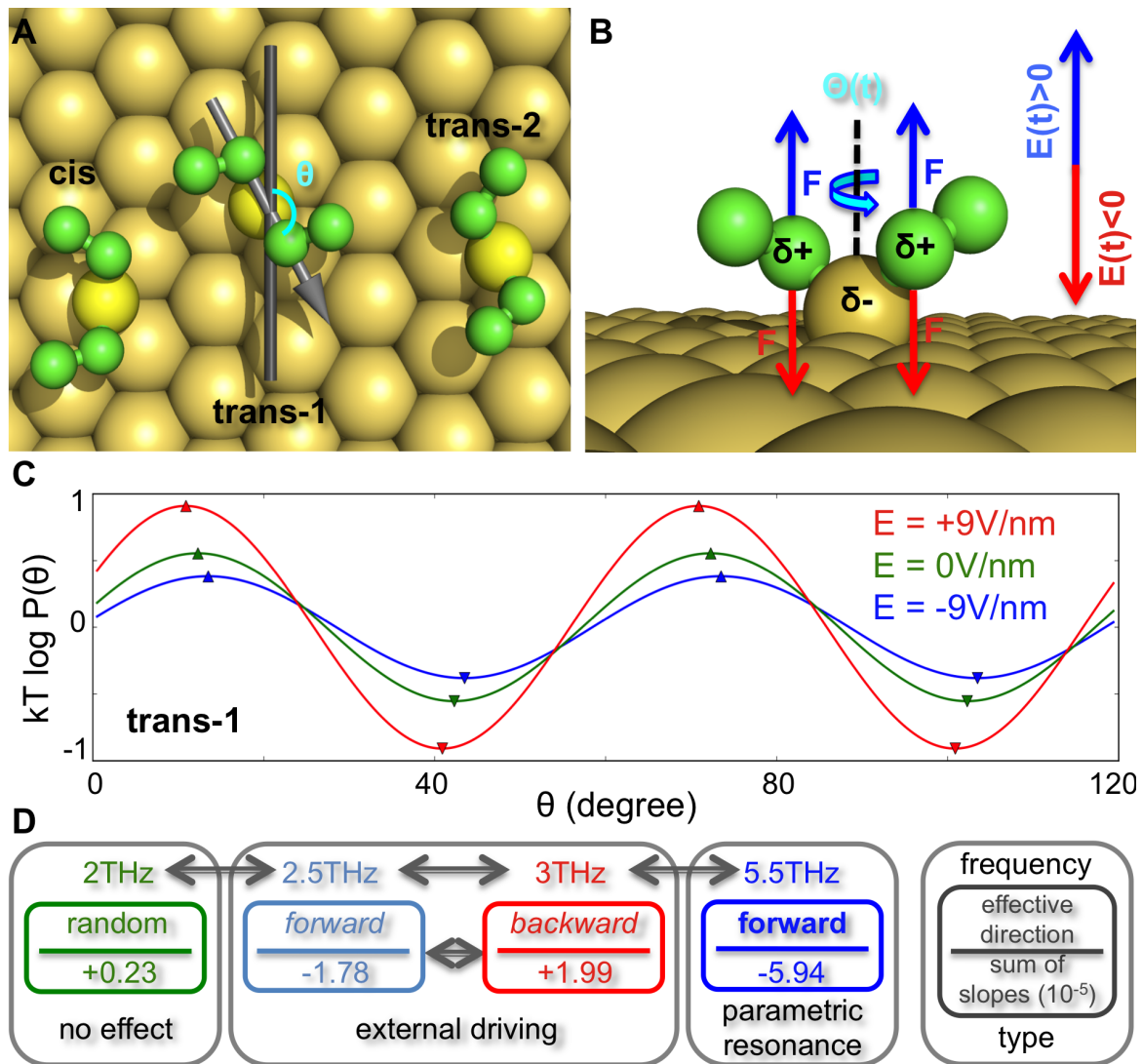


Figure 5.1: (A) Three conformations of the Diethylsulfid rotor on gold (111) surface are shown with indicated rotation angle θ . (B) The partial charges in the rotor ($\delta+ = 0.1675e$, $\delta- = -0.3350e$) are influenced by the external electric field. (C) The potential energy landscape $U(\theta, \vec{E})$ described by eq. 5.1 versus the rotation angle θ is plotted for high, neutral and low electric fields. (D) Scheme of the different driving regimes for the trans-1 conformation.

bidirectional rotation caused by a combination of external driving and parametric pumping of a non-deterministic system.

The isolated rotor has two intrinsic conformations - cis and trans (Fig. 5.1 A). Both conformations split in two sub-states when the rotor is bound to the gold (111) surface. The cis states (cis-1 and cis-2) can be transformed into one another with a rotation by 180° . The trans states (trans-1 and trans-2) can only interconvert by conformational change of the molecule, not by rotation around their sulfur-gold bond.

The rotor's partial charges can be influenced directly with an electric field (Fig. 5.1 B). All fields were perpendicular to the gold surface and the plane of rotation. From static field simulations we could characterize the potential energy landscapes of the different rotor conformations and for different electric field strengths ranging from -9 to $+9$ V/nm (Fig. 5.1 C, Fig. 2 in Ref. P4). The torsional energy landscape U with n energy minima per full cycle was fitted by

$$U(\theta, \vec{E}) = A(\vec{E})\cos[n\theta + \Phi(\vec{E})] \quad (5.1)$$

Both amplitude A and phase shift Φ depend on the external field \vec{E} for the trans conformations. The phase shift Φ has a different sign for trans-1 and trans-2 (Fig. 2 in Ref. P4). As expected from the second law of thermodynamics, no effective driving is detected with static electric fields. However, the rotational diffusion decreases from negative to positive external fields. The phase shift Φ is constant for the cis states.

The Terahertz oscillating field $\vec{E}(t) = E_0\cos(\omega t)$ can drive an effective rotation of the rotor. How is this possible with the potential energy landscape of the rotor $U(\theta, \vec{E})$ being symmetric at every instant of time? The answer is that the asymmetry necessary for the driving is induced with the coupled time-dependence of phase shift $\Phi[\vec{E}(t)]$ and amplitude $A[\vec{E}(t)]$. The oscillating phase shift effectively oscillates the position of the minimum while the amplitude oscillates the barrier heights. The direction and effective rotation rate depend also on the driving frequency ω (ranging from 1.5 to $7.5THz$). The oscillation of the energy minimum causes an oscillation of the peak of the angle distribution around the minimum position. The phase shift between

the minimum position and the population peak of the rotor depends on the driving frequency. For certain driving frequencies, the peak population experiences effectively a different barrier height for forward and backward rotations due to the coupled barrier height oscillations. Thus, a directed rotation depending on the external driving frequency is caused (Fig. 5.1 , Fig. 3 in Ref. P4). The equation of motion for the rotor motion driven by an external field \vec{E} and thermal noise $\xi(t)$ is similar to eq. 2.37:

$$I \frac{d^2\theta}{dt^2} + \Gamma \frac{d\theta}{dt} - \frac{\delta U(\theta, \vec{E})}{\delta\theta} = \xi(t). \quad (5.2)$$

From this a librational frequency $\omega_0 = n\sqrt{\frac{A(0)}{I}}$. Using a reduced mass of 15 amu, $n=6$ for the trans conformation and an amplitude of $1k_B T$, we calculate $\omega_0 = 2.4$ THz. Inspired by the knowledge of a combined external and parametric driving, the following equation describes the effective rotation except for a scaling factor

$$J = J_{\max} \left\{ \frac{\tau^{-1}(\omega - \omega_0)}{1 + [2\tau^{-1}(\omega - \omega_0)]^2} + \frac{1}{1 + [2\tau^{-1}(\omega - 2\omega_0)]^2} \right\} \quad (5.3)$$

using three parameters, the characteristic librational frequency ω_0 of approximately 2.8 THz and the damping frequency τ^{-1} which is a bit less than half the librational frequency and the maximum rotation frequency J_{\max} . The first term expresses the external driving as a Lorentz oscillator and the second term describes the parametric pumping at double the librational frequency $2\omega_0$. The mirror symmetric rotor conformations trans-1 and trans-2 are driven in different directions. The cis-states without oscillating phase shift do not show directional rotation, but only frequency-dependent diffusion.

Concluding, we can control bidirectional rotation of a molecular rotor using Terahertz electric fields. The structural design of the rotor molecule determines the most effective rotation rate and the preferred directionality of rotation. Both rotation

rate and directionality can be tuned by varying the external driving frequency. A theoretical framework is presented to describe the rotation with only two parameters.

5.4 Outlook

Design principles for a tunable rotor with the three states rotating clockwise, rotating counterclockwise and a random/locked state are suggested. Furthermore, these simulations can be the starting point for experimental studies to break microscopic and macroscopic reversibility in molecular systems. This is a first step in the direction of connecting molecular machines driven by a rotation to the electric wall socket. The neutral rotor and the parallel electric driving field perpendicular to the surface both allow an easy parallelization of many rotors. The effective rotation requires no metal surface but only a surface breaking the symmetry of the rotor. Here, we used a threefold symmetric gold and a twofold symmetric trans-conformation. This allows the rotor to be directly mounted on protein machinery. Our rotor is a proof of principle. Many optimizations need to be explored until a final product can be achieved. Important steps on this road are:

- Increase the coupling efficiency of the rotor to the external field by increasing the dipole moment perpendicular to the surface
- Develop a surface pattern which prefers a rotor conformation. This might allow a GHz puls which accelerates conformational switching to reset a majority of the rotors to a desired conformation.
- Develop a rotor with only one possible rotation on the surface and a method to securely couple it in the right orientation

5.5 Publication P4

Jan Neumann, Kay. E. Gottschalk and R. Dean Astumian.

Driving and controlling molecular surface rotors with a Terahertz electric field.

(submitted to Science)

6

List of Publications and Manuscripts

1. J. Morfill, J. Neumann, K. Blank, U. Steinbach, E.M. Puchner, K.-E. Gottschalk and H.E. Gaub. Force-based Analysis of Multidimensional Energy Landscapes: Application of Dynamic Force Spectroscopy and Steered Molecular Dynamics Simulations to an Antibody Fragment-Peptide Complex. . . . *Journal of Molecular Biology*, 381:1253-1266, **2008**.
2. J. Neumann and K.-E. Gottschalk. The effect of different force applications on the protein-protein complex barnase-barstar. *Biophysical Journal*, 97(6):1687–99, **2009**.
3. J. Neumann and K.-E. Gottschalk. The Integrin Talin Complex under Force. *PLoS Computational Biology*, submitted **2011**.
4. J. Neumann, K.-E. Gottschalk and R.D. Astumian. Driving and controlling a molecular surface rotor with Terahertz electric fields. *Science*, submitted **2011**.

Conference publication

5. J. Neumann, J. Morfill and K.-E. Gottschalk. Exploration of the energy landscape of protein-protein and antibody-antigen interactions. *From Computational Biophysics to Systems Biology (CBSB08), Proceedings of the NIC Workshop 2008*, pages 1–5, **2008**.

Force-based Analysis of Multidimensional Energy Landscapes: Application of Dynamic Force Spectroscopy and Steered Molecular Dynamics Simulations to an Antibody Fragment–Peptide Complex

Julia Morfill, Jan Neumann, Kerstin Blank*, Uta Steinbach, Elias M. Puchner, Kay-E. Gottschalk and Hermann E. Gaub

Lehrstuhl für Angewandte
Physik & Center for
Nanoscience, LMU München,
Amalienstrasse 54,
D-80799 München, Germany

Received 13 March 2008;
received in revised form
18 June 2008;
accepted 20 June 2008
Available online
28 June 2008

Multidimensional energy landscapes are an intrinsic property of proteins and define their dynamic behavior as well as their response to external stimuli. In order to explore the energy landscape and its implications on the dynamic function of proteins dynamic force spectroscopy and steered molecular dynamics (SMD) simulations have proved to be important tools. In this study, these techniques have been employed to analyze the influence of the direction of the probing forces on the complex of an antibody fragment with its peptide antigen. Using an atomic force microscope, experiments were performed where the attachment points of the 12 amino acid long peptide antigen were varied. These measurements yielded clearly distinguishable basal dissociation rates and potential widths, proving that the direction of the applied force determines the unbinding pathway. Complementary atomistic SMD simulations were performed, which also show that the unbinding pathways of the system are dependent on the pulling direction. However, the main barrier to be crossed was independent of the pulling direction and is represented by a backbone hydrogen bond between Gly^H-H40 of the antibody fragment and Glu^{O_E}-6_{peptide} of the peptide. For each pulling direction, the observed barriers can be correlated with the rupture of specific interactions, which stabilize the bound complex. Furthermore, although the SMD simulations were performed at loading rates exceeding the experimental rates by orders of magnitude due to computational limitations, a detailed comparison of the barriers that were overcome in the SMD simulations with the data obtained from the atomic force microscope unbinding experiments show excellent agreement.

© 2008 Elsevier Ltd. All rights reserved.

Keywords: single molecule force spectroscopy; atomic force microscope; molecular dynamics simulations; energy landscape; antibody–antigen interaction

Edited by D. Case

*Corresponding author. E-mail address:
Kerstin.Blank@chem.kuleuven.be.

Present address: K. Blank, Department of Chemistry,
Katholieke Universiteit Leuven, Celestijnenlaan 200 F,
B-3001 Heverlee, Belgium.

Abbreviations used: AFM, atomic force microscope;
scFv, single-chain Fv fragment; SMD, steered molecular
dynamics; PEG, poly(ethylene glycol); SPR, surface
plasmon resonance; MD, molecular dynamics.

Introduction

The knowledge of protein structures has revolutionized the understanding of protein function on the atomic level. However, crystal structures provide static pictures and do not account for the fact that proteins are soft materials, which, due to thermal fluctuations sample a large ensemble of slightly different conformations around their average structure. Multidimensional energy landscapes, which define the relative probabilities of the conformational states and the energy barriers between them, are able to describe the dynamical equilibrium of

protein conformations.^{1–3} As a result, the complexation of two proteins forming a protein–protein complex also occurs on these multidimensional energy landscapes. The corresponding complexation rates of a protein–protein interaction are determined by the barriers in the underlying energy landscape (Fig. 1a) that can be influenced by a variety of internal and external factors such as phosphorylation, mutations, or even the action of external forces. All these factors can alter the relative energy barrier height between different substates or even generate new local substates.

Since force is an ideal control parameter to explore the multidimensional energy landscape of a protein (Fig. 1b), single-molecule force spectroscopy experiments have become an important tool for studying the dynamic function of individual proteins and protein–protein complexes.^{4–10} Technically, the application of forces on the single-molecule level can be realized using different experimental techniques as well as molecular dynamics simulations. The atomic force microscope (AFM) and laser tweezers have evolved into the most prominent experimental tools for the analysis of the mechanical and dissociation properties of proteins and protein–protein interactions.^{11–14}

Here, the energy landscape of an antibody fragment–peptide complex was explored using single-molecule force spectroscopy and molecular dynamics simulations. We chose this system because the crystal structure of the complex is known,¹⁵ and

therefore provides the possibility of explaining the response of this complex to the externally applied force with structural data. The peptide antigen was derived from the leucine zipper domain of the yeast transcription factor GCN4. For the generation of antibodies, two proline mutations have been introduced into this 33 amino acid long peptide to prevent coiled coil formation. Using this peptide, mice have been immunized and the mouse antibody genes derived from the spleen cells have been cloned into a ribosome display system to select and improve peptide binders.^{15,16} The antibody single-chain Fv fragment (scFv; clone H6) was obtained from this affinity maturation process and has been further modified by site-directed mutagenesis. In order to crystallize the complex of scFv fragment and peptide, a truncated 12 amino acid long peptide was used, which is recognized by the scFv fragment. The truncated peptide binds to the scFv fragment in an α -helical conformation facing the scFv fragment with the side that binds the complementary peptide in the leucine zipper. This region of the peptide corresponds to the so-called trigger sequence, which has been found by Kammerer *et al.*¹⁷ The trigger region has been shown to be essential for folding and coiled coil formation of the leucine zipper and contains a high α -helical content.¹⁸ It is considered that the interaction of the two peptides upon coiled coil formation involves assembly of these α -helical stretches by conformational selection. The similarity of the peptide conformation in the coiled-coil pep-

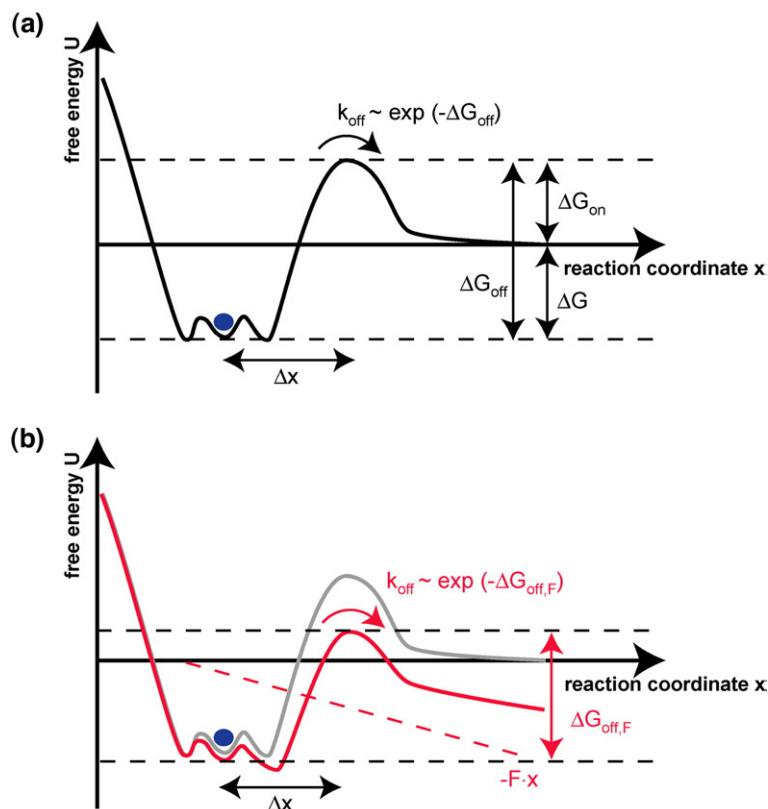


Fig. 1. Influence of an externally applied force on the energy landscape of a protein or a protein–protein complex. (a) Two-dimensional cross-section through the energy landscape without an externally applied force (black). In this picture the protein or the protein–protein complex (blue) is situated in one of the closely related substates at minimal energy. The free energy difference ΔG between the folded protein or the bound protein–protein complex (blue) and the unbound or unfolded state is determined by the difference between the energy barrier ΔG_{off} and the activation energy ΔG_{on} . Therefore, the barrier between these two states (ΔG_{off}), which can be overcome due to thermal fluctuations, determines the rate of interconversion (k_{off}). k_{off} is the basal dissociation rate; Δx is the potential width. (b) Two-dimensional cross-section through the energy landscape with an externally applied force (red). If an external force F is applied, the energy landscape is tilted (red), thereby reducing the energy barrier by $-Fx$ (broken red line). This reduction leads to an increase of the dissociation rate.

tide and in the complex with the antibody fragment implies that the binding to the antibody fragment follows a similar mechanism with helix formation being the prerequisite for binding to the antibody fragment.

For our studies, the peptide antigen provides the possibility to vary the attachment points of the peptide, since the amino acid for coupling can be introduced easily at different positions. This gives us the possibility to investigate whether the unbinding pathway of the regarded antibody fragment-peptide complex is changed by the direction of the applied force, which would point to the existence of a multidimensional energy landscape. High-resolution AFM-based single molecule force spectroscopy measurements were performed to determine the basal dissociation rate k_{off} , which correlates with the height of the energy barrier, which has to be overcome for unbinding, and the potential width Δx , which is a rough measure of the width of the binding potential. The results for k_{off} were then compared with the k_{off} values determined under equilibrium conditions with surface plasmon resonance (SPR).

Complementary, steered molecular dynamics (SMD) simulations were performed to provide additional information about the energy landscape of the respective antibody fragment-peptide system. Furthermore, SMD simulations allow the analysis of the chosen unbinding pathway with atomic resolution.^{19–22} SMD simulations enable the identification of the rupture events and the corresponding molecular interactions correlated with these ruptures.

This structural information was related to the results obtained from the AFM measurements.

Results and Discussion

Single-molecule force spectroscopy

The antibody fragment H6 used in our studies binds the truncated 12 amino acid long peptide antigen corresponding to amino acids 17–28 of the wildtype leucine zipper GCN4-p1.^{15,23} Here, the numbering of the structure file (PDB code 1P4B) is used, which numbers the amino acids of the peptide from 1 to 12. To explore the energy landscape of the antibody fragment-peptide complex in detail, force spectroscopy measurements were performed using an atomic force microscope (AFM). For this purpose, the antibody fragment H6 was covalently coupled to a surface containing covalently attached poly(ethylene glycol) (PEG) and the peptide was immobilized on the cantilever tip in the same way (Fig. 2). The use of the elastic spacer PEG minimizes nonspecific interactions and maximizes the probability of detecting specific and single rupture events. Three configurations representing different attachment points were analyzed in detail: For configuration N, a cysteine followed by three glycine residues was attached to the N terminus (Tyr-1_{peptide}; corresponding to amino acid 17 of the full-length leucine zipper) in order to couple the peptide to the cantilever of the AFM. For configuration M, the coupling

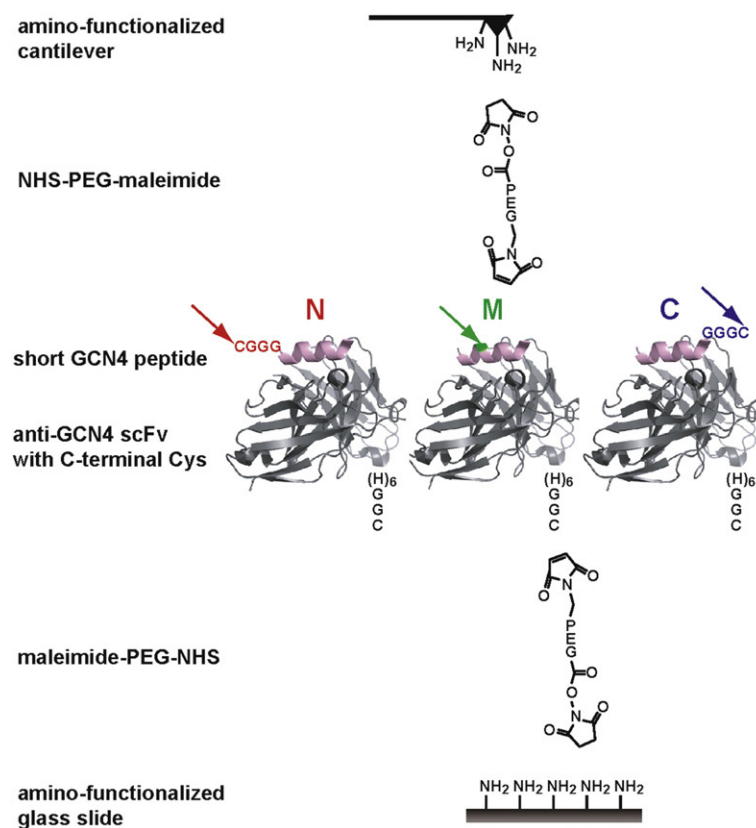


Fig. 2. Experimental setup. The antibody fragment H6 possessing a C-terminal cysteine was covalently immobilized onto an amino-functionalized glass slide using a heterobifunctional poly(ethylene glycol) spacer. The same coupling chemistry was used for the immobilization of the peptide to the cantilever. N, M and C show different measurement configurations. In configuration N, a cysteine and three glycine residues were attached to the N terminus of the peptide. In configuration M, alanine on position 8 of the peptide sequence was changed to a cysteine. In configuration C, three glycine residues followed by a cysteine were attached to the C terminus of the peptide.

to the cantilever was achieved via a cysteine residue, which replaced Ala-8_{peptide} (corresponding to amino acid 24 of the full-length leucine zipper) in the “middle” of the peptide. It is obvious from the structure of the peptide that Ala-8_{peptide} is not involved in interactions with the antibody fragment. However, this amino acid is in the region of the leucine zipper with the highest helix propensity and mutations in this region might impair helix formation.²⁴ For configuration C, a spacer of three glycine residues followed by a cysteine was attached to the C terminus of the truncated peptide (Lys-12_{peptide}; corresponding to amino acid 28 of the full-length leucine zipper). In the following, the three different attachment possibilities of the peptide are abbreviated to N, M and C. In all experiments, the surface was approached with the tip of the cantilever, allowing the antibody fragment-peptide complex to bind. Subsequently, the cantilever was retracted and the antibody fragment-peptide complex was loaded with an increasing force until the complex ruptured and the cantilever relaxed back into its equilibrium position. The force applied to this complex was recorded as a function of the distance between the cantilever tip and the surface. Fig. 3a shows three different force-extension curves, which correspond to the rupture events of the different antibody fragment-peptide complexes N (red), M (green) or C (blue) respectively. The force-extension curves measured for the three different configurations N, M and C exhibit similar rupture forces. To obtain good statistics, several hundreds of force-extension curves at different retract velocities were recorded using only one cantilever for every configuration. The use of one cantilever per configuration is crucial in these experiments to minimize errors originating from the cantilever calibration. The rupture force and the rupture length were determined from the force-extension curves. Force-time curves revealed the corresponding loading rate. Fig. 3b and c show the rupture force and loading rate distributions for configuration N, measured at a retract velocity of 800 nm/s. The rupture force histogram was fit with a Gaussian distribution (black curve) and has a most probable force of 47.3 pN. The Gaussian distribution of the loading rates (plotted logarithmically) (Fig. 3c) shows a maximum at a loading rate of 1307.8 pN s⁻¹. The maxima of the force and the loading rate distributions were determined for a large range of loading rates (from 40 pN s⁻¹ to 31,000 pN s⁻¹) for all three configurations, which were each measured with only one cantilever to reduce spring calibration errors within one measurement. In the following step these values were plotted in a force *versus* loading rate (plotted logarithmically) diagram (Fig. 4). Following the approach used by Evans and co-workers,⁴ the basal dissociation rate k_{off} and the potential width Δx were determined from a linear fit to the data points in the force *versus* loading rate diagram (Eq. (1)). The measurements of configuration N resulted in a k_{off} of $16.9(\pm 1.0) \times 10^{-3} \text{ s}^{-1}$ and a Δx of $0.82 \pm 0.01 \text{ nm}$. The denoted errors refer to the

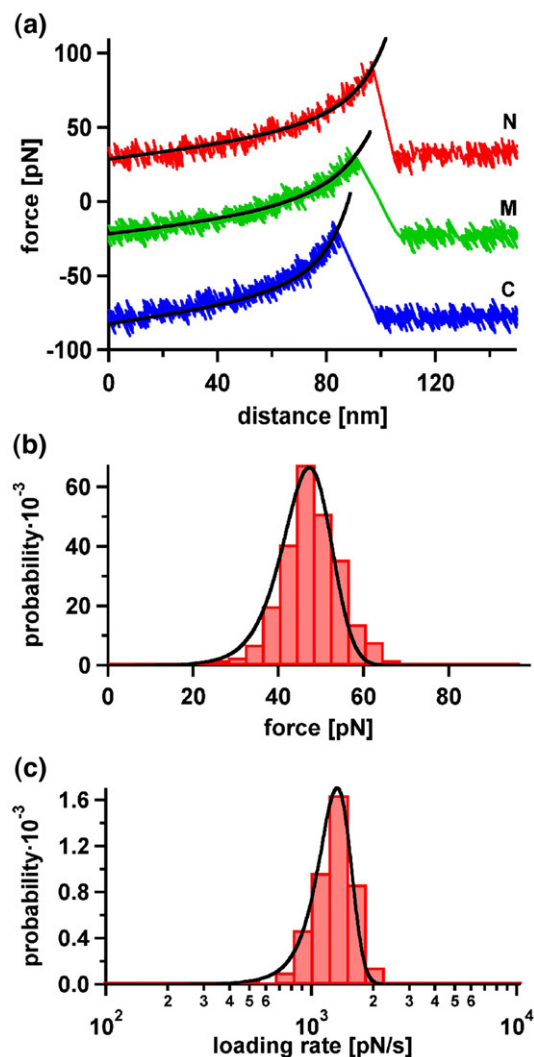


Fig. 3. Results from the AFM measurements. (a) Example of three typical force-extension curves measured for configurations N, M and C. The force-extension curves show the rupture event of the scFv-peptide complex, recorded at a retract velocity of 800 nm/s. The red force-extension curve corresponds to a rupture event measured for configuration N. The green and blue force-extension curves were gained for configurations M and C, respectively. All force-extension curves follow the characteristic shape of an extension curve of the poly(ethylene glycol) spacer and possess very similar rupture forces. The elastic behavior of the spacer can be described with the two-state FJC-fit (black curve). (b) Example of a rupture force distribution, obtained for configuration N. The rupture force histogram contains ~300 rupture events and was fitted with a Gaussian curve (black). (c) Example of a loading rate distribution obtained for configuration N. The histogram of the loading rates was plotted logarithmically and fit with a Gaussian curve (black).

constant estimated error of $\pm 0.2 \text{ pN}$, which includes the injected noise and oscillations as described in Materials and Methods. In order to obtain the total error of the measurement, the systematic error for the calibration of the spring constant needs to be taken into account. The resulting maximum and

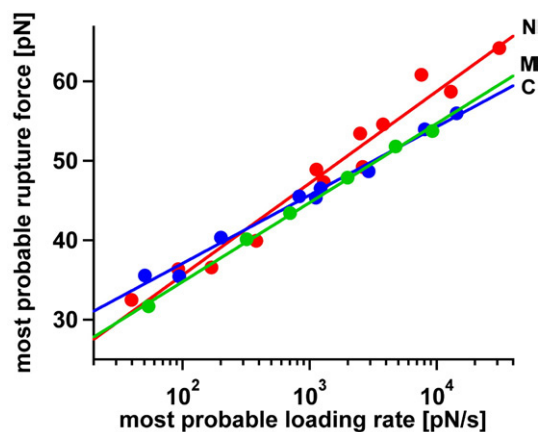


Fig. 4. Diagram showing the most probable rupture force plotted against the corresponding loading rate (logarithmically) for all three configurations N, M and C. The data points were gained from the Gaussian fits of the rupture force histogram and the histogram of loading rates. The red data points (configuration N) were fit to a straight line. From this linear fit, $\Delta x = 0.82 \pm 0.01$ nm and $k_{\text{off}} = 16.9(\pm 1.3) \times 10^{-3} \text{ s}^{-1}$ were obtained. The green data set was measured for configuration M. From the linear fit, $\Delta x = 0.95 \pm 0.01$ nm and $k_{\text{off}} = 7.6(\pm 1.0) \times 10^{-3} \text{ s}^{-1}$ were obtained. Finally, the measurement of configuration C yielded the blue data set. Here, the linear fit led to $\Delta x = 1.10 \pm 0.01$ nm and $k_{\text{off}} = 1.3(\pm 0.2) \times 10^{-3} \text{ s}^{-1}$.

minimum linear fit (see Materials and Methods) reveals the following values for k_{off} and Δx : $14.5(\pm 1.0) \times 10^{-3} \text{ s}^{-1}$ for $k_{\text{off,max}}$ and 0.79 ± 0.01 nm for Δx_{max} and $14.8(\pm 1.0) \times 10^{-3} \text{ s}^{-1}$ for $k_{\text{off,min}}$ and 0.87 ± 0.01 nm for Δx_{min} . The obtained values for k_{off} and Δx , including their calculated errors, for all configurations N, M and C are given in Table 1. This detailed error analysis demonstrates that the basal dissociation rates and the potential widths of the three different configurations N, M and C can be clearly separated. A comparison of the three different configurations shows that configuration N possesses the smallest potential width and the fastest basal dissociation rate, which corresponds to the smallest energy barrier in the respective multidimensional energy landscape. In contrast, configuration C revealed the largest potential width ($\Delta x = 1.10 \pm 0.01$ nm) and the slowest basal dissociation rate ($k_{\text{off}} = 1.3(\pm 1.0) \times 10^{-3} \text{ s}^{-1}$), which therefore corresponds to the highest energy barrier of the three measured configurations. The values for the basal dissociation rate ($k_{\text{off}} = 7.6(\pm 1.0) \times 10^{-3} \text{ s}^{-1}$) and the potential width ($\Delta x = 0.95 \pm 0.01$ nm) for con-

figuration M are between the values obtained for configurations N and C. Interestingly, the configuration with the fastest basal dissociation rate has the smallest potential width (configuration N), and the configuration with the slowest basal dissociation rate has the largest potential width (configuration C). Hence, in our system the length that the complex can be stretched before it finally ruptures is correlated with the basal dissociation rate. This correlation has been observed before for the interaction of different anti-fluorescein scFv fragments with their antigen fluorescein.²⁵ For the experiments performed here, this correlation can originate from a different starting conformation of the bound complexes. In this case, the number and strength of the stabilizing interactions would determine the basal dissociation rate and the potential width. Alternatively, the direction of the applied force can result in different unbinding pathways on the multidimensional energy landscape.

Comparison of the basal dissociation rates (AFM) with surface plasmon resonance (SPR) data

In order to rule out the existence of different starting conformations, SPR measurements were done to investigate whether the attached cysteine residues (at the N terminus, the C terminus and the Ala8Cys_{peptide} mutation) led to different conformations of the complex and as a result to differences in the dissociation rates and potential widths. These measurements revealed a dissociation rate of $1.5(\pm 0.6) \times 10^{-3} \text{ s}^{-1}$ for the peptide with the cysteine at its N terminus and $0.9(\pm 0.2) \times 10^{-3} \text{ s}^{-1}$ for the peptide with the cysteine at its C terminus. Furthermore, the following equilibrium binding constants were obtained: $13.4(\pm 8.7) \times 10^{-9} \text{ M}$ for configuration N and $9.2(\pm 5.0) \times 10^{-9} \text{ M}$ for configuration C. SPR measurements using the peptide with the Ala8Cys_{peptide} mutation failed due to an insufficient signal. As indicated earlier, the mutation might reduce the helix propensity and therefore result in a lower fraction of α -helical peptides that are available for binding to the antibody fragment. On the basis of this assumption, the amount of helical peptides is considered to be too low to produce a signal in the SPR measurements. Therefore, no conclusion can be drawn about the stability of the complex itself and configuration M is not discussed further. In contrast, the values for the peptides with the cysteine attached at the N or C terminus agree within the experimental error. Concluding from

Table 1. Summary of the values for k_{off} and Δx for the three different configurations N, M and C (AFM and SPR measurements)

Configuration	AFM						
	Original linear fit		Maximum linear fit		Minimum linear fit		SPR
	$k_{\text{off}} (\times 10^{-3} \text{ s}^{-1})$	Δx (nm)	$k_{\text{off}} (\times 10^{-3} \text{ s}^{-1})$	Δx (nm)	$k_{\text{off}} (\times 10^{-3} \text{ s}^{-1})$	Δx (nm)	$k_{\text{off}} (\times 10^{-3} \text{ s}^{-1})$
N	16.9±1.3	0.82±0.01	14.5±1.0	0.79±0.01	14.8±1.0	0.87±0.01	1.5±0.6
M	7.6±1.0	0.95±0.01	9.2±1.0	0.89±0.01	10.2±1.2	0.97±0.01	–
C	1.3±0.2	1.10±0.01	1.5±0.2	1.04±0.01	2.0±0.2	1.11±0.01	0.9±0.2

these data, the differences in the basal dissociation rates and potential widths, observed with the AFM, do not result from conformational changes in the peptide resulting from the cysteine residues attached either at the N or C terminus.

However, from these experiments it cannot be excluded that the different attachment points lead to a disturbance of the system when performing the AFM measurements. The structure together with the SMD simulations (see below) show that one of the main interactions between the peptide and the scFv fragment is very close to the N-terminal attachment point. Hence, the faster dissociation rate observed for the AFM in comparison to the SPR results might be caused by a partial unfolding of the peptide close to the attachment point, so that the interaction is partially weakened due to the linker used in the AFM measurements.

Although it cannot be ruled out that the immobilization on the AFM cantilever leads to slightly different conformations of the peptide, the data suggest that the different basal dissociation rates and potential widths are a consequence of the direction of the applied force. Assuming that the direction of the applied force results in different unbinding pathways, the values obtained for the basal dissociation rates and potential widths can be explained as follows. Within the experimental error, the basal dissociation rate for the peptide with the C-terminal cysteine determined with SPR agrees with the k_{off} value obtained for configuration C with the AFM. This leads to the conclusion, that the same barrier in the energy landscape is probed. In contrast, configuration N revealed a 13-fold higher basal dissociation rate, compared with the SPR value for the peptide with the N terminal cysteine. This difference for configuration N can be explained by considering an energy landscape with at least two barriers that need to be overcome (Fig. 5a). If no external force is applied, as is the case in the SPR measurements, the unbinding of the antibody fragment-peptide complex always follows the pathway with the lowest energy barrier. In contrast, in the AFM measurements the externally applied force is considered to define the pathway. In addition, the applied force tilts the energy landscape. The expected experimentally observed barrier heights and unbinding pathways are shown in the 2-D projection in Fig. 5b. For the SPR measurements, the second higher energy barrier is rate limiting for the unbinding of the antibody fragment-peptide complex, since this barrier has to be overcome to generate the free antibody fragment and the peptide (black curve in Fig. 5b). If an external force is applied, unbinding follows a different pathway and the energy landscape is tilted (red curve in Fig. 5b) such that the first originally lower energy barrier becomes prominent and is rate limiting. This simplified picture of the underlying energy landscape is able to explain the observed higher dissociation rate with the AFM for configuration N compared with the equilibrium measurement.

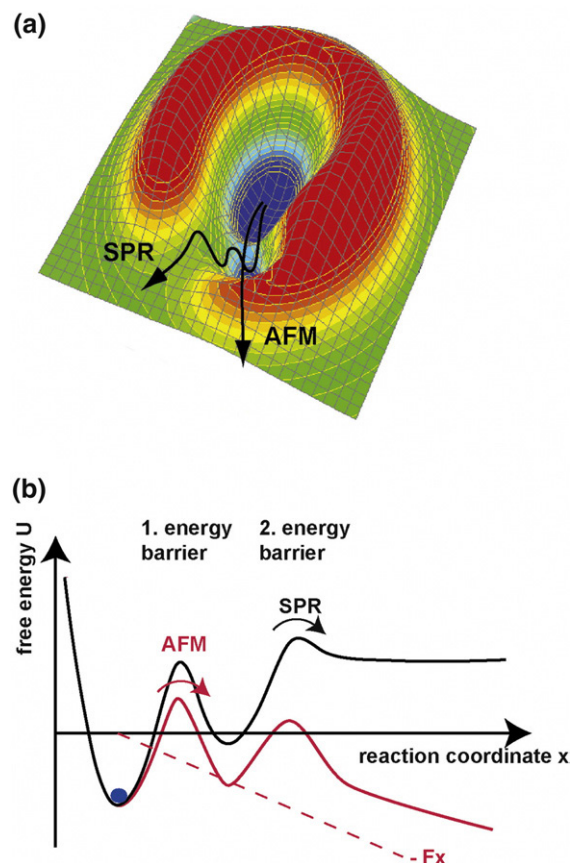


Fig. 5. Simplified model energy landscape explaining the AFM and SPR unbinding pathways of configuration N. (a) Three-dimensional representation of the energy landscape. In the SPR measurements, the unbinding of the antibody fragment-peptide complex always follows the pathway with the lowest energy barrier. In contrast, in the AFM measurements the pathway is determined by the direction of the applied force. (b) Two-dimensional projection of the unbinding pathway, including two energy barriers, in a defined direction. For the SPR measurements (black curve), the second higher energy barrier is rate limiting for the unbinding of the antibody fragment-peptide complex. If an external force is applied, the energy landscape is tilted (red curve). As a consequence, the first originally lower barrier becomes prominent and rate limiting for the unbinding process. Therefore, for configuration N, the AFM and SPR measurements probe different barriers of the energy landscape.

Steered molecular dynamics (SMD) simulations

SMD simulations were done in order to explore the energy landscape in the high-velocity regime and to obtain more structure-based information about the energy barriers.^{8,19–22,26} The structure PDB code 1P4B¹⁵ of the truncated 12 amino acid long peptide bound to the antibody fragment was used for all simulations. Corresponding to the AFM experiments, three different attachment points on the peptide were defined (see Fig. 6). A pulling potential was attached to the N terminus of the peptide (configuration N; Ala-1_{peptide}), its C-terminus (configuration C; Lys-12_{peptide}) and Ala-8_{peptide}

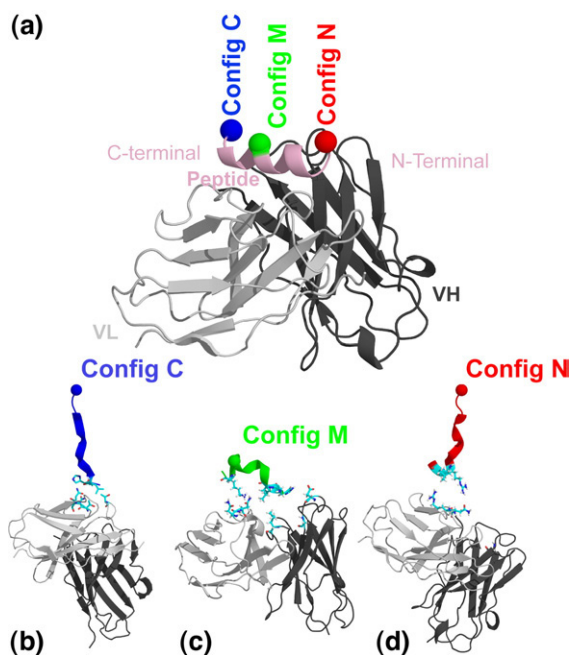


Fig. 6. Steered molecular dynamics simulations setup. All molecular dynamics simulations were started using the same initial structure. The center of mass (COM) of the heavy chain V_H was fixed in space during the whole simulation time, whereas the light chain V_L was not constricted. (a) For the simulation of the unbinding forces the pulling potential was attached to different C^α atoms of the peptide to yield the configurations N, M and C. (b–d) Last contacts between the scFv fragment and the peptide revealed by the SMD simulations. The last contacts between the peptide and the antibody fragment are shown for the respective configurations. The amino acids are identified in the main text.

(configuration M). In contrast to the AFM measurements, no additional amino acid was attached to the N or C terminus of the peptide and the alanine at position 8 was not replaced with a cysteine, which was necessary for the AFM-based analysis. The pulling potential steered the attached amino acid directly away from the antibody fragment at a speed of $v_{\text{pull}}=2$ nm/ns. The all-atom trajectories and the pulling forces for every time-step were recorded for every simulation.

An average force-time curve out of 20 trajectories was generated for every configuration. A characteristic force-time curve with minimal root-mean-square deviation from the average force-time curve is shown in Figs 7–9. At least 65% of all 20 trajectories show the main pathway of the average force-time curve and were used for further analysis. For each configuration, the average times t_i^j and average forces F_i^j ($i=1, 2$, corresponding to the number of the force peak; $j=N, M, C$) were determined by analyzing the force peaks, which indicate the positions of the major rupture events in the unbinding pathways, and the errors were calculated as Gaussian errors.

In configuration N, the peptide is zipped off the antibody fragment starting from its N terminus. Here, two main barriers have been identified (Fig. 7;

Table 2). The first barrier is crossed after $t_1^N=440\pm 25$ ps with a mean force of $F_1^N=567\pm 25$ pN and corresponds to the rupture of a hydrophobic contact between the amino acids Tyr-L40 and Leu-3_{peptide}. For the first rupture event, a rupture length of $r_1^N=0.88\pm 0.05$ nm was detected. The pathway that involves this interaction is taken in 75% of all trajectories. The second rupture event occurs after $t_2^N=860\pm 28$ ps with a mean force of $F_2^N=716\pm 23$ pN. For this second rupture event, the rupture length equaled $r_2^N=1.72\pm 0.06$ nm. The force peak, which corresponds to the second main barrier crossing and appears in 65% of all trajectories, results from the rupture of the H-bond between Glu^{O_e}-6_{peptide} and the backbone hydrogen Gly^H-H40. The last contact for the unbinding process is formed by Asn-L69, Arg-L70, Arg-9_{peptide} and Leu-10_{peptide}.

In configuration M, the peptide is separated from the antibody fragment in a double zipper mode, which leads to breakage of two stabilizing interactions next to the steered amino acid (Fig. 8).

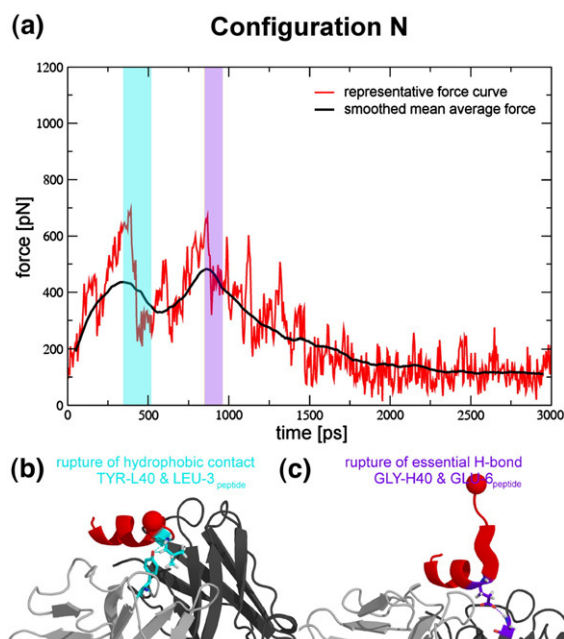


Fig. 7. Unbinding process of configuration N. (a) Force-time curves. The mean average force-time curve (black) and a representative force-time graph (red) were plotted. The unbinding process shows two important events, which correspond to the highlighted force peaks. The colors of the highlighted force peaks were chosen according to the colors in the molecular structures (cyan for the first rupture event and purple for the second rupture event). (b) Structural origin of the first unbinding event. The first unbinding event (cyan) corresponds to the rupture of the hydrophobic contact between Tyr-L40 and Leu-3_{peptide}. The picture shows the molecular structure shortly before the event is observed. (c) Structural origin of the second unbinding event (purple) corresponds to the rupture of the important H-bond between GLY^H-H40 and GLU^{O_e}-6_{peptide}. The picture shows the molecular structure shortly before the event is observed. This second rupture event has also been found in the two other configurations M and C.

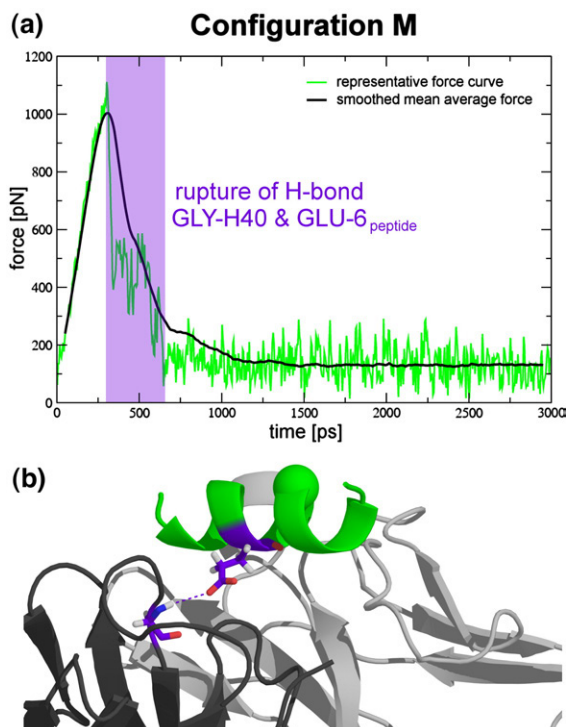


Fig. 8. Unbinding process of configuration M. (a) Force-time curves. The mean average force curve (black) and a representative force-time graph (green) were plotted. The force-time curve shows one major peak highlighted in purple. (b) Structural origin of the observed unbinding event. The unbinding event (purple) corresponds to the rupture of the important H-bond between Gly^H-H40 and Glu^{O^e}-6_{peptide}. The picture shows the molecular structure shortly before the event is observed. This rupture event has also been found in configurations N and C.

Nevertheless, only one major force peak can be identified after an average pulling time of $t_1^M = 319 \pm 9$ ps (corresponding to a rupture length of $r_1^M = 0.64 \pm 0.02$ nm) at an average force of $F_1^M = 1161 \pm 28$ pN (Table 2). The main barrier is identified clearly as the rupture of the H-bond between Gly^H-H40 and Glu^{O^e}-6_{peptide} (in 95% of all trajectories). This interaction also causes the second rupture event in the majority of trajectories in configuration N (Fig. 7; Table 2). Subsequent to this H-bond rupture in configuration M, after a mean time of additional $\Delta t^M = 40 \pm 8$ ps (corresponding to $\Delta r^M = 0.08 \pm 0.02$ nm), the double H-bond between Asp^{O⁶ⁱ}-H137 and Arg^{H⁶ⁱ}-9_{peptide} ($i = 1, 2$) ruptures (Fig. 8) without a resolvable additional force peak. The last contact for the unbinding process in configuration M is formed via Asn-L68, Asn-L69 and Lys-11_{peptide} on the C-terminal side. The last contact on the N-terminal side of the peptide ruptures shortly before the C-terminal last contact between Leu-3_{peptide} and His-2_{peptide} of the peptide and Asn-L68, Asp-H33 and Leu-H110 of the scFv fragment.

In configuration C, the peptide is zipped off starting from its C terminus end. Again, two main force peaks are identified. The first force peak was detected after $t_1^C = 514 \pm 20$ ps (corresponding to a

rupture length of $r_1^C = 1.03 \pm 0.04$ nm) at a mean force of $F_1^C = 775 \pm 28$ pN. This force peak coincides with the opening of the stabilizing backbone H-bond of the first peptide helix loop between Val-7_{peptide} and Leu-10_{peptide}. Hence, the first major rupture event refers to the opening of the secondary structure of the peptide and not to the breakage of a peptide-antibody fragment bond. The rupture of this interaction on the main unbinding pathway is seen in 85% of all trajectories. The second barrier crossing occurred after an average time of $t_2^C = 750 \pm 45$ ps with an average rupture length of $r_2^C = 1.50 \pm 0.09$ nm and an average force of $F_2^C = 720 \pm 21$ pN. This force peak is again determined by the rupture of the H-bond between Gly^H-H40 and Glu^{O^e}-6_{peptide} (Fig. 9; Table 2). A total of 65% of all trajectories crossed this second barrier via the main unbinding pathway. The last contact for the unbinding process of configuration C is formed via His-2_{peptide}, LEU-3_{peptide}, Thr-L32, Thr-L67, Asn-L68 and Asn-L69.

The three configurations underline the importance of the H-bond between the backbone of Gly^H-H40 and Glu^{O^e}-6_{peptide}. The breakage of this bond is a

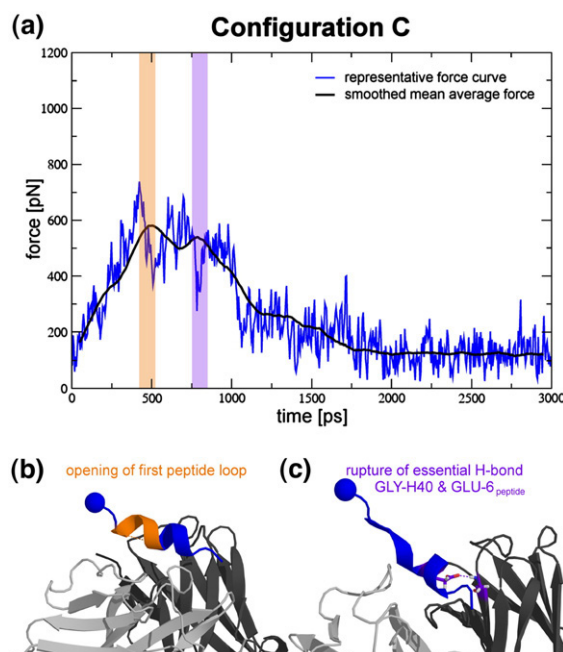


Fig. 9. Unbinding process of configuration C (a) Force-time curves. The mean average force-time curve (black) and a representative force-time graph (blue) were plotted. The two important rupture events represented by the force peaks of the mean curve were highlighted according to the colors in the molecular structures. (b) Structural origin of the first unbinding event. The first rupture event (orange) corresponds to the breakage of a backbone hydrogen bond stabilizing the α -helical structure of the peptide resulting in the opening of a peptide loop. The picture shows the molecular structure shortly before this event is observed. (c) Structural origin of the second unbinding event. The second unbinding event (purple) corresponds to the rupture of the important H-bond between Gly^H-H40 and Glu^{O^e}-6_{peptide}. The picture shows the molecular structure shortly before the event is observed. This rupture event has also been found in configurations N and M.

Table 2. Summary of the information obtained from the force curves from the three different configurations N, M and C (SMD simulations)

Configuration	Force peak 1				Force peak 2			
	t_1 (ps)	F_1 (pN)	r_1 (nm)	Interaction	t_2 (ps)	F_2 (pN)	r_2 (nm)	Interaction
N	440±25	567±25	0.88±0.05	Tyr-L40 and Leu-3 _{peptide}	860±28	716±23	1.72±0.06	Gly ^H -H40 and Glu ^{O^e} -6 _{peptide}
M	319±9	1161±28	0.64±0.02	Gly ^H -H40 and Glu ^{O^e} -6 _{peptide}	359±8	n. d.	0.72±0.02	Asp ^{O⁶ⁱ} -H137 and Arg ^{H⁶ⁱ} -9 _{peptide} ($i=1, 2$)
C	514±20	775±28	1.03±0.04	Loop opening	750±45	720±21	1.50±0.09	Gly ^H -H40 and Glu ^{O^e} -6 _{peptide}

dominant rupture event in the majority of all trajectories independent of the pulling vector. The configurations N and C, where the peptide unbinds in a single zipper mode, show two main rupture events. In configuration N, the first force peaks occurs earlier ($t_1^N < t_1^C$) and at lower forces ($F_1^N < F_1^C$) with respect to configuration C. The respective first force peak in configurations N and C results from different molecular interactions. Therefore, different force vectors probe different pathways through the landscape. However, the second force peak corresponds to the same molecular interaction of Gly^H-H40 and Glu^{O^e}-6_{peptide} in both configurations. The rupture forces of this interaction, indicative of the slope of the energy surface, are comparable in both configurations. And yet, in configuration C, the second force peak occurs earlier ($t_2^N > t_2^C$). The rupture length for this second force peak of configuration C ($r_2^C = 1.50 \pm 0.09$ nm) is hence shorter than in configuration N ($r_2^N = 1.72 \pm 0.06$ nm), despite probing the identical interaction. This is due to the different intramolecular distances between force attachment points and the Glu^{O^e}-6_{peptide}, demonstrating that, depending on the configuration, the same barrier can have different characteristics (here, the barrier width). Furthermore, this interaction between Gly^H-H40 with Glu^{O^e}-6_{peptide} is also probed in configuration M, showing a very different fingerprint of the force curve than in the other two configurations. The shorter rupture length and higher rupture forces compared with configurations N and C result from the very direct force attachment point, again underlining the fact that the molecular nature of the interaction and the geometry of the force probing crucially determine the characteristics of the probed interaction.

Comparison of the SMD and AFM results

Both simulation and experiment probe the respective antibody fragment-peptide complex at the same positions on the peptide, thereby exerting forces in the same directions. SMD simulations, due to computational limitations, probe the system at much higher loading rates.^{22,27} Hence, thermal relaxation occurs only partially. The system lacks the time to relax orthogonally to the pulling direction and resulting from this, lacks the time to explore the energy landscape locally to find the optimal pathway to cross the barrier.²⁷ This might lead to a steeper pathway on the energy landscape potentially

crossing higher barriers and finally resulting in higher rupture forces. Whereas higher rupture forces have been observed for all configurations, this effect is most dominant for configuration M, which unbinds in a double zipper mode (nearly simultaneous rupture of two bonds). In the simulations, as soon as the first important interaction breaks (H-bond Gly^H-H40, which binds Glu^{O^e}-6_{peptide}), the more stable double H-bond of the interaction between Asp^{O⁶ⁱ}-H137 and Arg^{H⁶ⁱ}-9_{peptide} ($i=1, 2$) experiences the full load and ruptures within 40 ps (Fig. 8). In contrast, in the AFM experiments, the system can relax orthogonally to the applied force and can re-arrange after the first breakage. As a result, after the first breakage the complex might become so unstable that dissociation occurs on a timescale too fast to be observed with the AFM.

Furthermore, the Ala8Cys mutation in the peptide used in the AFM experiments may lead to additional disturbances of the peptide structure, which may result in a lower stability of the complex. The mutation lies in that region of the peptide with the highest probability for α -helix formation and mutations at this position have been shown to have an influence on the stability of the leucine zipper.^{24,28} Although, as described previously, this mutation is considered to influence the binding process more than the stability of the bound complex, a destabilizing contribution of the mutation on the complex cannot be fully excluded.

A more detailed comparison of the values obtained from the AFM experiments and the SMD simulations provides an explanation of the energy barriers on the unbinding pathways for the respective configurations. The comparison of the potential widths obtained with the AFM and the rupture lengths obtained from the SMD simulations shows that the rupture lengths for configurations N and C for the first barrier crossing of the main unbinding pathway (r_1^N, r_1^C) are in good agreement with the potential widths obtained with the AFM ($\Delta x^N, \Delta x^C$) (Tables 1 and 2). Hence, the AFM experiments probe the first barrier observed in the SMD simulations (Fig. 10). Again, for configuration M, the observed differences might result from the different relaxation due to different time regimes and from the potentially destabilizing mutation, as discussed above.

Furthermore, the SMD simulations provide further evidence for the existence of a second energy barrier,

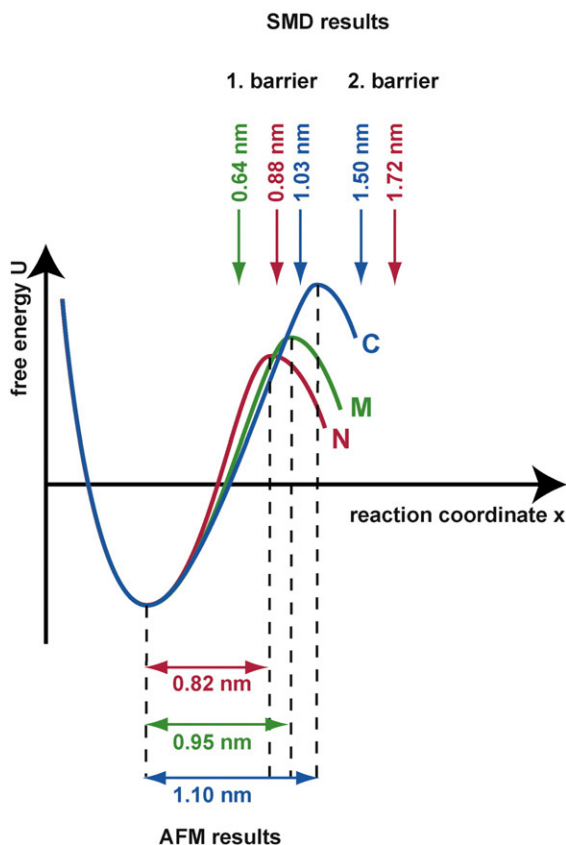


Fig. 10. Two-dimensional projection of the energy barriers obtained from the AFM experiments and the rupture lengths obtained from the SMD simulations. To summarize the results, the potential widths and basal dissociation rates have been taken from the AFM measurements and plotted in a 2-D energy diagram (configuration N, red; configuration M, green; and configuration C, blue) to provide an overview of the barriers that need to be crossed. Further unbinding pathways on the respective energy landscapes are not known. The arrows above the energy landscapes indicate the positions of the respective rupture lengths for the first and second barrier crossing of the main unbinding pathway, obtained from the SMD simulations.

which was not shown unambiguously by the AFM and SPR data. The forces needed to overcome the second barrier of the main unfolding pathway are of the same order of magnitude as for the first barrier crossing. Yet, the second rupture event for configurations N and C occurs at nearly twice the distance of the first rupture event (Table 2). Hence, the second energy barrier of the main unfolding pathway in the energy landscape has a large potential width. Outer barriers are much more influenced by externally applied forces than inner barriers, due to the tilted energy landscape. Because of this large potential width of the second barrier observed in the SMD simulations, it is plausible that this barrier is not probed in the AFM measurements, even at the lowest applied loading rates. Therefore, the existence of two energy barriers is not in conflict with the observation that the AFM data could be fit with a straight line in the force *versus* loading rate plot in Fig. 4.

The SMD data explain the observed potential widths in the different experimental configurations, and they provide more information about the basal dissociation rates of the first barrier crossing obtained from the AFM measurements. As stated earlier, the results from the SMD simulations show that the first barrier crossing in configuration C occurs at a longer rupture length ($r_1^C > r_1^N$) and at a greater force ($F_1^C > F_1^N$) than in configuration N. Since the forces measured with the SMD simulations correspond to the slope of the energy barrier in the energy landscape, the higher forces observed in configuration C result from a steeper energy barrier. This steeper energy barrier together with the longer rupture length indicates that the first energy barrier of the main unbinding pathway is higher in configuration C than in configuration N. A higher energy barrier corresponds to a lower dissociation rate. Hence, if — as already concluded from the comparison of AFM and SPR — the inner energy barrier is rate-determining for the AFM experiments (Fig. 5), experiment and simulation agree on a lower dissociation rate for configuration C compared with the dissociation rate for configuration N ($k_{\text{off},1}(\text{C}) < k_{\text{off},1}(\text{N})$).

Conclusions

A well-characterized antibody–antigen interaction has been chosen to explore the underlying energy landscape with a combination of different techniques. The main focus was to investigate if different pulling directions lead to different unbinding pathways and therefore provide a more detailed insight into the unbinding process of the interaction. SMD simulations detected two rupture events for every pulling direction. One rupture event in each configuration is determined by the same molecular bond, whereas the other rupture event originates from the breakage of different bonds. These findings show clearly that the underlying energy landscape is multidimensional. This information could not be obtained from the AFM measurements alone, which show a linear dependence of the rupture forces on the logarithm of the loading rate — a feature that is characteristic for a two-state system with only one barrier. However, a comparison of AFM and SPR points to the existence of at least one more barrier. SPR always probes the lowest energy barrier in the energy landscape. When performing AFM measurements, the complex might be forced to follow a steeper unbinding pathway, which would result in a lower dissociation rate (corresponding to a higher barrier). But, as stated earlier, the basal dissociation rate for configuration N obtained with the AFM is higher than the k_{off} value obtained with SPR. This leads to the conclusion that the energy barrier probed with the AFM is lower than the energy barrier that has to be overcome under equilibrium conditions. Therefore, an additional energy barrier has to exist along the pulling direction of configuration N (Fig. 5), which is not detectable with the

AFM. The results from the SMD simulations further support this conclusion, since the outer (second) barrier has a very large potential width so that the inner (first) barrier is most likely rate-determining even at the smallest loading rates. For configuration C, the SMD simulations also show a second barrier, which is considered to be lower than the first barrier and which is therefore not probed experimentally.

In conclusion, the experimental set-up chosen for the AFM measurements, which allows the site-specific immobilization of the binding partners, shows clearly that the direction of the applied force defines the unbinding pathway on a multidimensional energy landscape. This finding points out clearly that non(site)-specific coupling procedures provide a simplified picture of the molecular interactions as the contributions of different unbinding pathways are averaged out.

Materials and Methods

Preparation of the peptides and the scFv fragment

Peptides representing a truncated version of the GCN4-p1 leucine zipper Y₁HLENEVA₈RLKK₁₂ were obtained from Jerini Peptide Technologies GmbH, Berlin, Germany. A cysteine has been introduced at different positions during solid-phase synthesis to provide site-specific attachment points for the immobilization on the cantilever (Fig. 2): NH₂-CGGGYHLENEVARLKK-amide (configuration N), NH₂-YHLENEVCRLKK-amide (configuration M), and NH₂-YHLENEVARLKKGGGC-amide (configuration C).

The expression and purification of the scFv fragment H6 was carried out as described.²⁹ Briefly, the scFv fragment H6 was expressed with a C-terminal His tag followed by cysteine to allow a site-specific immobilization. The plasmid for the periplasmic expression in *Escherichia coli* is based on the pAK series.³⁰ The gene for co-expression of the periplasmic chaperone Skp was introduced.³¹ The original His tag was replaced by a His₆ tag followed by two glycine residues and a cysteine. For the expression and purification of H6, the protocol described by Hanes *et al.*¹⁶ was slightly modified. In short, the bacteria with the transformed plasmid were grown at 25 °C in SB medium (20 g l⁻¹ Tryptone, 10 g l⁻¹ yeast extract, 5 g l⁻¹ NaCl, 50 mM K₂HPO₄) containing 30 µg ml⁻¹ chloramphenicol. Expression was induced with 1 mM isopropyl-β-d-thiogalactopyranoside (IPTG) at an A₆₀₀ between 1.0 and 1.5. The cells were harvested 3 h after induction by centrifugation. Cell disruption was achieved by French press lysis. The scFv fragment H6 was purified using two chromatography steps. After chromatography on a Ni²⁺-NTA column (Qiagen, Hilden, Germany) using standard protocols the eluted fraction was loaded directly onto an affinity column with immobilized antigen. The fractions from the affinity column were dialyzed against coupling buffer (50 mM sodium phosphate, pH 7.2, 50 mM NaCl, 10 mM EDTA) and concentrated using Centricon YM-10 (Millipore, Eschborn, Germany). The actual concentration of the purified scFv fragment H6 was determined by measuring A₂₈₀. The extinction coefficient was calculated using the program Vector NTI (Invitrogen, Karlsruhe, Germany). The preparation of the purified protein was adjusted to a concentration of 0.8 mg ml⁻¹ and stored at -80 °C.

Preparation of slides and cantilevers for the AFM measurements

Poly(ethylene glycol) (PEG) was used as a spacer between the biomolecules and the surfaces. PEG is an ideal spacer for force spectroscopy measurements^{25,32-37}, as it provides protein-resistant surfaces,³⁸ thereby reducing the number of non-specific binding events. In addition, PEG shows a characteristic force-extension curve, allowing the discrimination between specific and non-specific interactions during data analysis. The scFv fragment H6 possessing a C terminal cysteine was immobilized on an amino-functionalized slide using a hetero-bifunctional NHS-PEG-maleimide (mass = 5000 g/mol; Nektar, Huntsville, AL, USA). The three peptides were separately immobilized via their introduced cysteine to an amino-functionalized cantilever, again using the NHS-PEG-maleimide spacer (Fig. 2).

In detail, the cantilevers (Bio-lever, Olympus, Tokyo, Japan) were activated with a 10 min UV-ozone cleaning treatment and amino modified with 3-aminopropyl-dimethylethoxysilane (ABC R GmbH, Karlsruhe, Germany) as described.^{29,35,36} Commercially available amino-functionalized slides (Slide A, Nexterion, Mainz, Germany) were used for the immobilization of the scFv fragment. For the next steps, both surfaces (slide and cantilever) were treated in parallel as described.³⁹ Briefly, they were incubated in 50 mM sodium borate buffer, pH 8.5, in order to increase the fraction of unprotonated amino groups for coupling to the NHS groups of the PEG. NHS-PEG-maleimide was dissolved at a concentration of 50 mM in borate buffer and incubated on the surfaces for 1 h. In parallel, one of the peptides and the scFv fragment H6 were reduced using TCEP beads (Perbio Science, Bonn, Germany) in order to generate free thiols. After washing both surfaces with ultrapure water, a solution of the peptide (200 µM) was incubated on the cantilever and a solution of the scFv fragment H6 (0.13 mg/ml) was incubated on the slide for 1 h. Finally, both surfaces were rinsed with PBS (10 mM sodium phosphate, pH 7.4, 137 mM NaCl, 2.7 mM KCl) to remove non-covalently bound material, and stored in PBS at room temperature.

Force spectroscopy

All force measurements were performed with a MFP-1D AFM (Asylum Research, Santa Barbara, CA, USA) at room temperature in PBS. The cantilever spring constants were 8.7 pN/nm for the measurement of configuration N (see Fig. 2), 3.4 pN/nm for the measurement of configuration M, and 4.2 pN/nm for the measurement of configuration C (B-Bio-Lever) and were obtained as described.^{40,41} During the experiments, the approach and retract velocity were held constant, whereas the applied force was adjusted by changing the distance between the cantilever tip and the surface to obtain single binding events. Several hundred approach-retract cycles were carried out to achieve good statistics. Each experiment was done for different retract velocities ranging from 50 nm/s to 10 µm/s to obtain measurements over a broad range of loading rates.

Data extraction

The experimental data were converted into force-extension curves. From these, the rupture force (the force at which the antibody fragment-antigen complex ruptures), the rupture length and the loading rate were

determined using the program Igor Pro 5.0 (Wavemetrics, Lake Oswego, OR, USA) and a custom-written set of procedures. The rupture force was determined as described.^{4,42} The loading rate was determined using the two-state, freely jointed chain fit to the force-extension curve, according to previous studies.⁴³

Data analysis

To analyze the data set obtained from one experiment, which was recorded at a constant retract velocity, the rupture forces, the rupture lengths and the loading rates were plotted in three histograms. These histograms were analyzed with a method based on the so-called Bell-Evans model.^{4,44} The rupture force and loading rate (plotted logarithmically) histograms for each data set, i.e. for each retract velocity, were fitted with a Gaussian distribution to determine the maxima. Finally, these obtained maxima were plotted in a force *versus* loading rate diagram. The maximum force (from the Gaussian distribution of the rupture force histogram) represents the most probable force F^* :

$$F^* = \frac{k_B \cdot T}{\Delta x} \ln \frac{F \cdot \Delta x}{k_B \cdot T \cdot k_{\text{off}}} \quad (1)$$

where k_B is the Boltzmann constant, T is temperature, Δx is the potential width, k_{off} is the basal dissociation rate at zero force and F^* ($=dF/dt$) is the loading rate. From a linear fit of the force *versus* loading rate (pictured logarithmically) plot and Eq. (1), Δx and k_{off} of the antibody fragment-antigen complex can be determined from the slope and the intercept of the linear fit with the abscissa.

Error estimation

To calculate the error of the dissociation rate k_{off} and the potential width Δx , the following assumptions were made:

- (i) The error in the calibration of the spring constant constitutes 10 %.
- (ii) Injected noise and oscillations lead to an error of ± 0.2 pN in the measured rupture force. This value was estimated from the integration of the frequency spectrum of the cantilever in PBS to a frequency of 10 Hz.

As described above, k_{off} and Δx can be calculated from the linear fit to the data points in the force *versus* loading rate diagram. Due to the use of only one cantilever for all data points, the error, originating from the calibration of the spring constant, leads to systematic higher or lower rupture forces and loading rates, and therefore to higher or lower most probable rupture forces and loading rates. We therefore determined the maximum and minimum linear fit. From these two fits, the maximum and minimum k_{off} and Δx can be calculated. In addition, the estimated value of ± 0.2 pN was taken into account. This error is not systematic and can be added or subtracted from the most probable rupture force. By using a random generator, a mean linear fit was calculated. From this, we gained a mean value for k_{off} and Δx with the corresponding standard deviation. This procedure was applied to the original, the maximum and the minimum linear fit in the force *versus* loading rate plot to receive the maximum and minimum k_{off} and Δx with their corresponding standard deviations.

Proof of specificity

To prove the specificity of the force spectroscopy measurements, experiments were performed, either without the antibody fragment or without the peptide. By measuring the antibody fragment H6, attached to the surface, against a cantilever tip passivated with PEG, more than 1000 force-extension curves were recorded. Thereby, less than 1% non-specific interactions were detected. The measurements without the peptide led to similar results.

SPR measurements

The measurements of the dissociation rate k_{off} (25 °C) and the equilibrium constants K_d of the scFv fragment H6 and the peptide with cysteine at either its N or C terminus were done with a Biacore X instrument (Biacore, Freiburg, Germany). For this purpose a CM5 sensor chip (Biacore) was modified via amine coupling according to the manufacturer's protocol. Clone H6 was diluted in immobilization buffer (10 mM sodium acetate, pH 5.0) to a final concentration of 11.4 ng/ μ l and placed onto the chip. The final signal intensity on the surface was ~ 200 RU. A series of the respective peptide solutions in PBS buffer in the range of 1.64–400 nM for the measurement of k_{off} and 4–400 nM for the measurement of K_d was placed onto the chip. After binding, dissociation was followed at a flow rate of 50 μ l/min. The dissociation and association phase was fit globally, using the single-exponential fit function of the program BIAevaluation 3.2. The equilibrium constants were gained from separate determination of the dissociation and association rate.

Molecular dynamics simulations (MD)

All MD simulations were based on the 2.35 Å resolution X-ray structure 1P4B¹⁵ of the antibody scFv fragment bound to the peptide A₁HLENEVA₈RLKK₁₂. Here, the amino acids of the antibody fragment are labeled with the three-letter code of the amino acid, the location in the V_H or V_L domain, and the position in the 1P4B PDB structure. The amino acids of the peptide are labeled as a combination of the three-letter code and the number of the amino acid in the crystal structure. To distinguish between antibody fragment and peptide amino acids, the residues of the peptide are identified by the subscript peptide.

The first amino acid of the 1P4B PDB structure differs from the experimentally used amino acid. We chose not to mutate the sequence to match the experimental one, because this would have reduced the resolution of the structure. The influence of this sequential difference will not be significant, since it is located at the non-interacting end of the peptide.

All MD simulations were performed using the software GROMACS.^{45–47} We used periodic boundary conditions, the OPLS-AA force field⁴⁸ and SPC/E water⁴⁹ for all MD simulations. For all simulations first one energy-minimized, equilibrated and pre-oriented state of the proteins solved in water was generated. This initial structure was assigned to new Boltzmann-distributed velocities and again equilibrated shortly before the SMD simulations were performed.

System preparation

The antibody fragment-peptide structure 1P4B was pre-oriented with the helical peptide axis parallel with the z-

axis of the system. Then the molecules were solvated in a 6.8 nm × 6 nm × 11.6 nm waterbox (16,034 H₂O) ionized with 45 sodium and 43 chloride atoms. The overall charge of the system was neutral.

Steepest descent energy minimization was performed with a maximum step size of 0.01 nm up to a precision of 2000 kJ/(mol·nm). No pressure or temperature coupling was used. The cut-off radius for Coulomb and van der Waals interactions was set to 1 nm.

Afterwards, a water relaxation simulation of 200 ps was preformed. On all protein atoms, a positional restraint was placed using a harmonic potential with a force constant of 2000 kJ/(mol·nm²) = 3.32 nN/nm on the protein atoms. The LINCS algorithm was used on all bond constraints.⁵⁰ Protein and non-protein atoms were coupled separately to a heat-bath of 300 K using a time constant of 0.1 ps.

All further simulations were performed using fast particle-mesh Ewald electrostatics with an order of 4 and a van der Waals cut-off of 1.0 nm. A 1 ns equilibration of the whole system followed. A leapfrog algorithm with a time-step of 2 fs was used. All C^α atoms were restrained with a harmonic potential of 1000 kJ/(mol·nm) = 1.8 nN/nm to avoid an unwanted rotation of the system. The restraint potential was weak enough to allow small conformational changes of the backbone due to the equilibration. The side chains were not restricted and therefore freely equilibrating. The RMSD (nm) fit of the C^α position reached a stable plateau within this equilibration (data not shown). The temperature was restricted to 300 K analogs to the last step. The resulting structure was used as the initial structure for all configurations to allow a better comparison of the results. Before the actual SMD simulations were performed, for each simulation new random Boltzmann distributed velocities were assigned and an additional 200 ps pre-equilibration was performed.

Simulations

In every SMD simulation the antibody fragment was fixed in space via a COM movement removal of the chain V_H of the antibody fragment. In each configuration, a different C^α atom was steered away from the antibody fragment (in the *x*-direction) with a harmonic potential using a spring constant of $k = 1600 \text{ kJ}/(\text{mol}\cdot\text{nm}^2) = 2.66 \text{ nN}/\text{nm}$. This steering was executed for 3 ns at a speed of $v_{\text{pull}} = 2 \text{ nm}/\text{ns}$ resulting in a final separation of 6 nm. The strong steering potential forces the attached atom to follow it closely. No other atom of the peptide is restricted in any way, leaving it to respond freely to the forced movement of the attached atom.

Three different configurations were tested in correspondence to the AFM experiments. In configuration N, the C^α atom of the N-terminal alanine Ala-1_{peptide} of the antigen peptide was attached to the steering potential. In configuration C, the C^α atom of the C-terminal amino acid Lys-12_{peptide} was attached and in the configuration M the C^α atom of the eighth amino acid Ala-8_{peptide} was attached. In contrast to the AFM experiments, no mutation in configuration M was performed, because no cysteine for external linkage was needed in the SMD simulations.

Acknowledgements

We thank Dr. Torsten Pirch and Professor Dr. Kirsten Jung for the SPR data, Professor Dr. Andreas

Plückthun for the gift of the expression vector of the antibody fragment and Gert De Cremer for help in preparing Fig. 5. This work was supported by the Center for Integrative Protein Science Munich, the European Union, the Deutsche Forschungsgemeinschaft and the Fonds der Chemischen Industrie.

References

1. Henzler-Wildman, K. & Kern, D. (2007). Dynamic personalities of proteins. *Nature*, **450**, 964–972.
2. Tsai, C. J., Ma, B., Sham, Y. Y., Kumar, S. & Nussinov, R. (2001). Structured disorder and conformational selection. *Proteins: Struct. Funct. Genet.* **44**, 418–427.
3. Kumar, S., Ma, B., Tsai, C. J., Sinha, N. & Nussinov, R. (2000). Folding and binding cascades: dynamic landscapes and population shifts. *Protein Sci.* **9**, 10–19.
4. Evans, E. & Ritchie, K. (1999). Strength of a weak bond connecting flexible polymer chains. *Biophys. J.* **76**, 2439–2447.
5. Merkel, R., Nassoy, P., Leung, A., Ritchie, K. & Evans, E. (1999). Energy landscapes of receptor-ligand bonds explored with dynamic force spectroscopy. *Nature*, **397**, 50–53.
6. Bustamante, C., Bryant, Z. & Smith, S. B. (2003). Ten years of tension: single-molecule DNA mechanics. *Nature*, **421**, 423–427.
7. Nevo, R., Brumfeld, V., Kapon, R., Hinterdorfer, P. & Reich, Z. (2005). Direct measurement of protein energy landscape roughness. *EMBO Rep.* **6**, 482–486.
8. Barsegov, V. & Thirumalai, D. (2005). Probing protein-protein interactions by dynamic force correlation spectroscopy. *Phys. Rev. Lett.* **95**, 168302.
9. Kessler, M., Gottschalk, K. E., Janovjak, H., Müller, D. J. & Gaub, H. E. (2006). Bacteriorhodopsin folds into the membrane against an external force. *J. Mol. Biol.* **357**, 644–654.
10. Bornschlöggl, T. & Rief, M. (2006). Single molecule unzipping of coiled coils: sequence resolved stability profiles. *Phys. Rev. Lett.* **96**, 118102.
11. Evans, E., Ritchie, K. & Merkel, R. (1995). Sensitive force technique to probe molecular adhesion and structural linkages at biological interfaces. *Biophys. J.* **68**, 2580–2587.
12. Rief, M., Gautel, M., Oesterhelt, F., Fernandez, J. M. & Gaub, H. E. (1997). Reversible unfolding of individual titin immunoglobulin domains by AFM. *Science*, **276**, 1109–1112.
13. Oesterhelt, F., Oesterhelt, D., Pfeiffer, M., Engel, A., Gaub, H. E. & Müller, D. J. (2000). Unfolding pathways of individual bacteriorhodopsins. *Science*, **288**, 143–146.
14. Kessler, M. & Gaub, H. E. (2006). Unfolding barriers in bacteriorhodopsin probed from the cytoplasmic and the extracellular side by AFM. *Structure*, **14**, 521–527.
15. Zahnd, C., Spinelli, S., Luginbühl, B., Amstutz, P., Cambillau, C. & Plückthun, A. (2004). Directed *in vitro* evolution and crystallographic analysis of a peptide-binding single chain antibody fragment (scFv) with low picomolar affinity. *J. Biol. Chem.* **279**, 18870–18877.
16. Hanes, J., Jermutus, L., Weber-Bornhauser, S., Bosshard, H. R. & Plückthun, A. (1998). Ribosome display efficiently selects and evolves high-affinity antibodies *in vitro* from immune libraries. *Proc. Natl Acad. Sci. USA*, **95**, 14130–14135.
17. Kammerer, R. A., Schulthess, T., Landwehr, R., Lustig, A., Engel, J., Aebi, U. & Steinmetz, M. O. (1998). An

- autonomous folding unit mediates the assembly of two-stranded coiled coils. *Proc. Natl Acad. Sci. USA*, **95**, 13419–13424.
18. Myers, J. K. & Oas, T. G. (1999). Reinterpretation of GCN4-p1 folding kinetics: partial helix formation precedes dimerization in coiled coil folding. *J. Mol. Biol.* **289**, 205–209.
 19. Grubmüller, H. (1995). Predicting slow structural transitions in macromolecular systems: conformational flooding. *Phys. Rev. E*, **52**, 2893–2906.
 20. Sotomayor, M. & Schulten, K. (2007). Single-molecule experiments *in vitro* and *in silico*. *Science*, **316**, 1144–1148.
 21. Grubmüller, H. (2005). Force probe molecular dynamics simulations. *Methods Mol. Biol.* **305**, 493–515.
 22. Rief, M. & Grubmüller, H. (2002). Force spectroscopy of single biomolecules. *ChemPhysChem*, **3**, 255–261.
 23. O'Shea, E. K., Klemm, J. D., Kim, P. S. & Alber, T. (1991). X-ray structure of the GCN4 leucine zipper, a two-stranded, parallel coiled coil. *Science*, **254**, 539–544.
 24. Holtzer, M. E., Lovett, E. G., d'Avignon, D. A. & Holtzer, A. (1997). Thermal unfolding in a GCN4-like leucine zipper: ¹³C alpha NMR chemical shifts and local unfolding curves. *Biophys. J.* **73**, 1031–1041.
 25. Schwesinger, F., Ros, R., Strunz, T., Anselmetti, D., Güntherodt, H. J., Honegger, A. *et al.* (2000). Unbinding forces of single antibody-antigen complexes correlate with their thermal dissociation rates. *Proc. Natl Acad. Sci. USA*, **97**, 9972–9977.
 26. Gao, M., Wilmanns, M. & Schulten, K. (2002). Steered molecular dynamics studies of titin I1 domain unfolding. *Biophys. J.* **83**, 3435–3445.
 27. Evans, E. & Ritchie, K. (1997). Dynamic strength of molecular adhesion bonds. *Biophys. J.* **72**, 1541–1555.
 28. Zitzewitz, J. A., Ibarra-Molero, B., Fishel, D. R., Terry, K. L. & Matthews, C. R. (2000). Preformed secondary structure drives the association reaction of GCN4-p1, a model coiled-coil system. *J. Mol. Biol.* **296**, 1105–1116.
 29. Morfill, J., Blank, K., Zahnd, C., Luginbühl, B., Kühner, F., Gottschalk, K. E. *et al.* (2007). Affinity-matured recombinant antibody fragments analyzed by single molecule force spectroscopy. *Biophys. J.* **93**, 3583–3590.
 30. Krebber, A., Bornhauser, S., Burmester, J., Honegger, A., Willuda, J., Bosshard, H. R. & Plückthun, A. (1997). Reliable cloning of functional antibody variable domains from hybridomas and spleen cell repertoires employing a reengineered phage display system. *J. Immunol. Methods*, **201**, 35–55.
 31. Bothmann, H. & Plückthun, A. (1998). Selection for a periplasmic factor improving phage display and functional periplasmic expression. *Nature Biotechnol.* **16**, 376–380.
 32. Hinterdorfer, P., Baumgartner, W., Gruber, H. J., Schilcher, K. & Schindler, H. (1996). Detection and localization of individual antibody-antigen recognition events by atomic force microscopy. *Proc. Natl Acad. Sci. USA*, **93**, 3477–3481.
 33. Ros, R., Schwesinger, F., Anselmetti, D., Kubon, M., Schäfer, R., Plückthun, A. & Tiefenauer, L. (1998). Antigen binding forces of individually addressed single-chain Fv antibody molecules. *Proc. Natl Acad. Sci. USA*, **95**, 7402–7405.
 34. Kienberger, F., Pastushenko, V. P., Kada, G., Gruber, H. J., Riemer, C. K., Schindler, H. & Hinterdorfer, P. (2000). Static and dynamic properties of single poly(ethylene glycol) molecules investigated by force spectroscopy. *Single Mol.* **1**, 123–128.
 35. Neuert, G., Albrecht, C., Pamir, E. & Gaub, H. E. (2006). Dynamic force spectroscopy of the digoxigenin-antibody complex. *FEBS Lett.* **580**, 505–509.
 36. Morfill, J., Kühner, F., Blank, K., Lugmaier, R. A., Sedlmair, J. & Gaub, H. E. (2007). B-S transition in short oligonucleotides. *Biophys. J.* **93**, 2400–2409.
 37. Kühner, F., Morfill, J., Neher, R. A., Blank, K. & Gaub, H. E. (2007). Force-induced DNA slippage. *J. Biophys.* **92**, 2491–2497.
 38. Alcantar, N. A., Aydil, E. S. & Israelachvili, J. N. (2000). Polyethylene glycol-coated biocompatible surfaces. *J. Biomed. Mater. Res.* **51**, 343–351.
 39. Blank, K., Morfill, J. & Gaub, H. E. (2006). Site-specific immobilization of genetically engineered variants of *Candida antarctica* lipase B. *ChemBioChem*, **7**, 1349–1351.
 40. Butt, H. J. & Jaschke, M. (1995). Calculation of thermal noise in atomic-force microscopy. *Nanotechnology*, **6**, 1–7.
 41. Hugel, T. & Seitz, M. (2001). The study of molecular interactions by AFM force spectroscopy. *Macromol. Rapid Commun.* **22**, 989–1016.
 42. Friedsam, C., Wehle, A. K., Kühner, F. & Gaub, H. E. (2003). Dynamic single-molecule force spectroscopy: bond rupture analysis with variable spacer length. *J. Phys. Condens. Matter*, **15**, S1709–S1723.
 43. Oesterhelt, F., Rief, M. & Gaub, H. E. (1999). Single molecule force spectroscopy by AFM indicates helical structure of poly(ethylene-glycol) in water. *New J. Phys.* **1**, 6.1–6.11.
 44. Bell, G. I. (1978). Models for the specific adhesion of cells to cells. *Science*, **200**, 618–627.
 45. Berendsen, H. J. C., van der Spoel, D. & van Drunen, R. (1995). GROMACS: A message-passing parallel molecular dynamics implementation. *Comput. Phys. Commun.* **91**, 43–56.
 46. Lindahl, E., Hess, B. & van der Spoel, D. (2001). GROMACS 3.0: a package for molecular simulation and trajectory analysis. *J. Mol. Model.* **7**, 306–317.
 47. van der Spoel, D., Lindahl, E., Hess, B., Groenhof, G., Mark, A. E. & Berendsen, H. J. C. (2005). GROMACS: fast, flexible and free. *J. Comput. Chem.* **26**, 1701–1718.
 48. Jorgensen, W. L., Maxwell, D. S. & Tirado-Rives, J. (1996). Development and testing of the OPLS all-atom force field on conformational energetics and properties of organic liquids. *J. Am. Chem. Soc.* **118**, 11225–11236.
 49. Berendsen, H. J. C., Grigera, J. R. & Straatsma, T. P. (1987). The missing term in effective pair potentials. *J. Phys. Chem.* **91**, 6269–6271.
 50. Hess, B., Bekker, H., Berendsen, H. J. C. & Fraaije, J. G. E. M. (1997). LINCS: A linear constraint solver for molecular simulations. *J. Comput. Chem.* **18**, 1463–1472.

The Effect of Different Force Applications on the Protein-Protein Complex Barnase-Barstar

Jan Neumann and Kay-Eberhard Gottschalk*

Angewandte Physik und Biophysik, Ludwig-Maximilians Universität, Munich, Germany

ABSTRACT Steered molecular dynamics simulations are a tool to examine the energy landscape of protein-protein complexes by applying external forces. Here, we analyze the influence of the velocity and geometry of the probing forces on a protein complex using this tool. With steered molecular dynamics, we probe the stability of the protein-protein complex Barnase-Barstar. The individual proteins are mechanically labile. The Barnase-Barstar binding site is more stable than the folds of the individual proteins. By using different force protocols, we observe a variety of responses of the system to the applied tension.

INTRODUCTION

Forces are regulating factors on protein complexes. Application of forces is important in numerous processes in biological systems like cell adhesion or cellular mobility (1–5). In addition, forces are often used as an experimental tool for studying the energy landscapes of both individual proteins and protein-protein complexes (6–8). The interpretation of these experiments is complex and a thorough description of the influence of different force protocols on the unbinding pathways is critical (9). In particular, force-induced unfolding follows pathways that are different from spontaneous free-solution, chemically-induced, or temperature-induced types of unfolding (10,11).

Technically, the application of forces on the nanoscale can be realized using different experimental techniques like atomic force microscopy (AFM), force pipette, optical tweezers, or simulation methods like steered molecular dynamics (SMD) on the single-molecule level (12–22).

The response of secondary structure elements on different orientations of external stresses leads to a large range of unraveling forces (23–25). In more recent studies, the dependence of the mechanical stability of protein unfolding on the force linkage is demonstrated. On the model system of ubiquitin, it is shown, by experiment and simulation, that different ubiquitin linkages in nature differ in their unfolding forces and unfolding free energy profiles (26–28). The unfolding of fibronectin depends critically on the vector of the applied forces (29). The force response and energy landscape of the fluorescence molecule GFP on different force attachment points has been examined using AFM experiments as well as model simulations (28,30,31). An asymmetric nature of the force response of the titin kinase in a symmetrical setup was shown by Gräter et al., demonstrating the direction dependency of the protein response to force (32), recently supported by AFM measurements (33). In force-clamp simulations, possible relations between

forced and chemically induced unfolding pathways have been suggested (34). These studies underline the importance of both the history of force application as well as the direction of the force vector for the observed response.

Applied forces have also been used to estimate binding energies and to analyze protein-protein complexes. Recently, SMD simulations were used to force the cytochrome *c*2 unbinding from the reaction center (35), to unbind an antibody-antigen complex (36) as well as to analyze the protein-protein interaction energies of the TCR-pMHC complex (37).

A general advantage of SMD simulations over the experimental techniques is that the chosen unfolding pathway can be analyzed in atomistic detail. However, due to computational limitations, the used velocities exceed the experimental ones by orders of magnitude. This renders a direct comparison between experiment and simulation complicated. Thus, insight into the atomistic response to different force protocols used is crucial for this comparison. Furthermore, it reveals details of the underlying energy landscape not observable without the explicit control over the experimental parameters offered by the simulation.

In this work, we perform SMD simulations on the protein-protein complex Barnase-Barstar. We use different attachment points and different velocities of the force application to observe the response of the model system. This allows us to gain detailed insight into the effect of differently applied forces on a protein complex analogous to the dependence of mechanical stability of protein unfolding on the force linkage.

Barnase is a bacterial RNase, which is excreted by the bacterium *Bacillus amyloliquefaciens* and is deadly to unprotected cells (38–42). The natural inhibitor Barstar protects the bacterium. Due to the high evolutionary pressure, the Barnase-Barstar complex is one of the fastest forming and most stable complexes known (43).

The fast association of the Barnase-Barstar is electrostatically facilitated (44–46). Poisson-Boltzmann calculations predicted a stabilizing electrostatic effect in agreement with

Submitted May 16, 2008, and accepted for publication January 13, 2009.

*Correspondence: kay.gottschalk@physik.uni-muenchen.de

Editor: Helmut Grubmüller.

© 2009 by the Biophysical Society
0006-3495/09/09/1687/13 \$2.00

doi: 10.1016/j.bpj.2009.01.052

experimental data (47). Brownian dynamics studies of the Barnase-Barstar complex showed that its association is diffusion-limited and the experimentally measured association rates can be reproduced (39,44,48,49). Recently, the free energy landscape of this association has been analyzed. An optimal association pathway was found involving a region close to the RNA binding loop of the protein complex (50,51). An overlap of association and dissociation pathways, using rigid-body Brownian dynamics simulations with an implicit solvent model, has been suggested (51). Although the equilibrium association of the Barnase-Barstar complex has been studied to a great extent, the response of the complex to nonequilibrium conditions has not been examined as thoroughly. However, during export of the complex, it is exposed to forces. Furthermore, protein complexes are in general an attractive target for force studies: the probing of protein-protein complexes by force can be regarded as a complex differential assay, where the mechanical stability of the individual folds is compared to the stability of the noncovalent binding site, depending on a variety of experimental parameters.

The aim of this study is to investigate the mechanical stability of this model complex under the influence of different force applications. Since Barnase needs to be exported from the cell, we expect a low mechanical stability of the individual protein. However, since the cell needs to be protected as long as Barnase is not exported, we expect a high stability of the Barnase-Barstar binding site inhibiting RNA binding. Indeed, we demonstrate here that the complex binding site is more stable than the individual domains. We recapture basic features of the unbinding transition state. We show that we can alter the main trajectory from unfolding to several unbinding pathways by altering the attachment points of the steering forces. Hence, our simulations probe, in a differential force assay, the relative stability of regions within the complex, depending on the force protocol used.

METHODS

All simulations on the Barnase-Barstar complex (PDB code: 1BRS (52)) were performed with the MD simulation software GROMACS Ver. 3.2–3.3.3 (53,54). Periodic boundary conditions, SPC/E (55) water, and OPLS-AA (56) force field were used for all simulations.

System preparation

The Barnase-Barstar structure was preoriented in a $4 \text{ nm} \times 5.8 \text{ nm} \times 12 \text{ nm}$ waterbox. The vector connecting $C_{\alpha}^{\text{bn}7}$ and $C_{\alpha}^{\text{bs}86}$ was oriented parallel to the z axis of the box. Thirteen Na^+ and nine Cl^- atoms were added to neutralize the overall charge of the system at a 75 mM NaCl concentration.

Energy minimization was performed with steepest descent and with a maximum step size of 0.01 nm. A cutoff radius of 1 nm for Coulomb and van der Waals interactions was used.

A 200-ps positional restraint simulation followed. All protein atoms were restrained by a harmonic potential with a harmonic force constant of $2000 \frac{\text{kJ}}{\text{mol} \cdot \text{nm}^2} = 3.32 \frac{\text{nN}}{\text{nm}}$. All bonds were constrained via the LINCS algorithm (57). The COM translation of the system was removed. Berendsen temperature coupling (58) was used to couple the protein atoms and the nonprotein

atoms separately in two groups with a temperature bath of 300 K and a time-constant of 0.1 ps.

For all further simulations, electrostatics were calculated with fast particle-mesh Ewald electrostatics (59) with an order of four and a cutoff for Coulomb and van der Waals interactions of 1.0 nm.

Five-hundred picoseconds of equilibration were performed using the leap-frog algorithm with a timestep of 2 fs. All C_{α} backbone-atoms were restrained with a harmonic potential with a force constant of $200 \frac{\text{kJ}}{\text{mol} \cdot \text{nm}^2}$ to avoid a rotation of the system. For equilibration and all SMD runs, the protein complex and the solvent molecules were coupled to two separate Berendsen thermostats, setting each temperature to 300 K. In addition, Berendsen pressure coupling (58) set the whole system to 1 bar with a compressibility of $4.5 \times 10^{-5} \text{ bar}^{-1}$ and a time-constant of 0.5 ps. The final structure of this equilibration step was used as the initial structure for all SMD simulations.

Before an SMD was started, velocities were again randomly assigned and another 200-ps equilibration were performed.

SMD simulation

For all setups, constant velocity pulling simulations with fast ($v_{\text{fast}} = 2 \frac{\text{nm}}{\text{ns}}$), medium ($v_{\text{medium}} = 0.5 \frac{\text{nm}}{\text{ns}}$), and slow ($v_{\text{slow}} = 0.125 \frac{\text{nm}}{\text{ns}}$) pulling velocities was done. The COM movement was removed for the atom/group where the complex was fixed in space. A harmonic potential with a spring constant of $k = 1600 \frac{\text{kJ}}{\text{mol} \cdot \text{nm}^2} = 2.66 \frac{\text{nN}}{\text{nm}}$ was moved in z direction until the final position was at least 3.5 nm (up to 6 nm) away from the initial position. The majority was pulled 5 nm, which results in a pulling time of 2.5 ns for fast, 10 ns for medium, and 40 ns for slow pulling trajectories. The hard spring constantly forces the atom to closely follow the harmonic potential spatially and in time. Because the spring constant was kept constant, its influence on the loading rate of the AFM did not vary in Setups 1–3. The number of simulated trajectories per setup and pulling velocity can be found in Table 1.

Setup 1

The harmonic potential mimicking an AFM tip was attached to the C_{α} atom of the first residue of the first element with regular secondary structure of Barnase ($C_{\alpha}^{\text{bs}86}$) and fixed the position of the C_{α} atom of the last residue of the last element with regular secondary structure of Barstar ($C_{\alpha}^{\text{bn}7}$) in Setup 1. For the mirrored setup, Setup 1_m, the attachment points for pulling and spatial fixation were exchanged (Fig. 1 B).

Setup 2

The COM of Barstar was pulled by the time-dependent harmonic potential, whereas the COM of Barnase was fixed.

Setup 3

For the direct probing of the protein-protein binding site, the COM of the C_{α} values of the Barstar binding helix was the attachment point of the force. The COM of Barnase was fixed like in Setup 2. Only fast pulling was simulated. Due to the early unbinding of the protein complex, the pulling was only simulated for 2.25 ns, corresponding to a pulling length of 4.5 nm.

Calculation of effective force and work

First, the time of separation for each single trajectory in Setups 2 and 3 was determined. The forces exerted on the system after the separation were assumed to be the drag forces of the molecule through the solvent water. These drag forces were averaged for each trajectory individually from the time of the separation to the end of the simulation. To renormalize the forces after the separation to zero, we subtracted the average drag forces from the calculated forces. This resulted in an effective force F_{eff} for the separation:

$$F_{\text{eff}}(x) = F(x) - \langle F_{\text{drag}} \rangle. \quad (1)$$

TABLE 1 The average maximum forces (unfolding for Setups 1 and 1_m; unbinding for Setups 2 and 3) for the different pulling velocities are given with the standard deviation of the forces as error; (...) denotes the average

	Velocity	Attachment	Loading rate/ $\frac{\text{pN}}{\text{ns}}$	$\langle F_{\text{max}} \rangle / \text{pN}$	Error/pN	No. of trajectories/pathway/total number per setup
Setup 1, unfolding						
Barnase	Fast	C-C	5320	951	61	12/77
	Medium	C-C	1330	799	55	24/31
	Slow	C-C	332,5	753	61	7/12
Barstar	Fast	C-C	5320	903	82	67/77
	Medium	C-C	1330	809	58	14/31
	Slow	C-C	332,5	762	33	5/12
Setup 1 _m , unfolding						
Barnase	Fast	C-C	5320	827	57	70/73
	Medium	C-C	1330	732	53	15/15
	Slow	C-C	332,5	737	97	12/12
Barstar	Fast	C-C	5320	855		1/73
Setup 2, unbinding						
	Fast	COM-COM	5320	1310	95	9/67
	Medium	COM-COM	1330	1123	65	10/10
	Slow	COM-COM	332,5	938	97	8/8
Setup 3, unbinding						
	Fast	Helix-COM	5320	1702	175	55/55
	Medium	Helix-COM	1330	1332	214	10/10
	Slow	Helix-COM	332,5	1168	201	8/8

The effective work done during the separation of the complex was calculated by

$$W_{\text{eff}}(x) = \sum_1^{x_i \leq x} F_{\text{eff}}(x_i) \times (x_i - x_{i-1}). \quad (2)$$

These work curves $W_{\text{eff}}(x)$ were then averaged for each pulling velocity of Setups 2 and 3. No average work distributions for Setups 1 and 1_m were calculated since no unbinding is seen.

RESULTS

To understand the influence of force application on the complex, the unfolding pathways need to be described.

Due to the high complexity of the system, an approach to reduce this complexity to a small set of descriptive parameters is needed.

We analyzed the unbinding pathways by defining characteristic contacts in the protein, which open during the simulation. A careful analysis of our trajectories led to the definition of the five specific contacts for the description of the unfolding pathways.

The contacts 1 and 3 are within Barstar. The contact 2 is a contact within Barnase, while the contacts 4 and 5 are between both complex partners (Fig. 1, Table 2). The calculation of the average fluctuations of these specific contacts during the whole equilibration show stochastic fluctuations

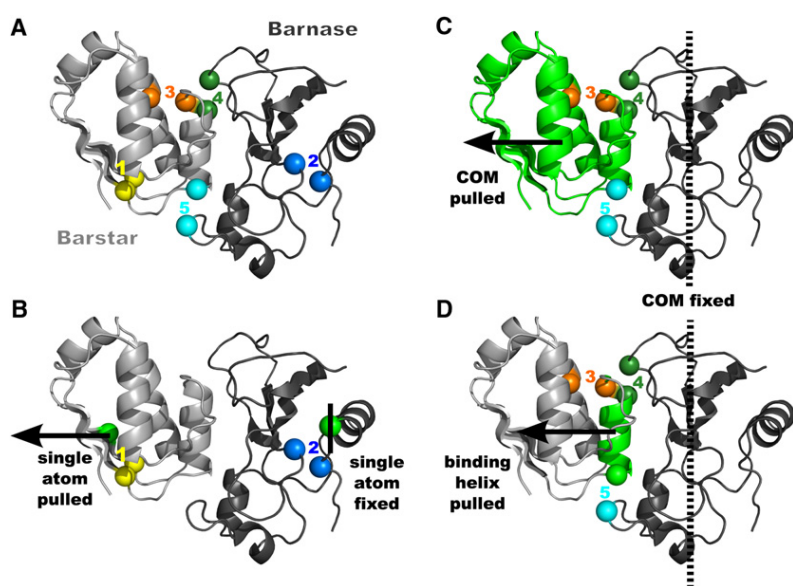


FIGURE 1 (A) Contact points for the analysis of the pathways. The molecular structure of Barnase (dark gray) complexing Barstar (light gray). The specific contacts chosen for a description of the unfolding pathways are shown as colored spheres and denoted with numbers 1–5. (B) Setup 1. The moving potential was attached to the last C_{α} -atom $C_{\alpha}^{\text{bs}86}$ of the last secondary structural element of Barstar (highlighted and with velocity arrow in the direction of pulling), while the spatially fixed potential was located at $C_{\alpha}^{\text{bn}7}$ (with vertical line), the first C_{α} -atom of the first secondary structure element of Barnase (dark gray). (C) Setup 2. The moving potential was attached directly to the COM of Barstar (left molecule), while the spatially fixed potential was attached to the COM of Barnase (right molecule). (D) Setup 3. For a direct probing of the binding site, the moving potential was located at the Barstar binding helix (highlighted and with velocity arrow), while the static potential was attached to the COM of Barnase (dark gray).

TABLE 2 The contact separation distances d_i and the characteristic atoms used in the analysis to determine the trajectory path

Contact	Side chain 1	Side chain 2	$d_i^{\text{eq}}/\text{nm}; \text{in nm}$	$f_i^{\text{eq}}/\text{nm}; \text{in nm}$
d_1	Leu _{bs} 49	Ile _{bs} 84	0.48	0.02
d_2	Asn _{bn} 5	Ile _{bn} 76	0.53	0.02
d_3	Leu _{bs} 34	Val _{bs} 70	0.65	0.02
d_4	Arg _{bn} 59	Asp _{bs} 35	0.58	0.04
d_5	Ser _{bn} 38	Trp _{bs} 44	0.52	0.04

The contacts are given with the three-letter code of the amino acid with the chain at lower position (*bn*, Barnase; *bs*, Barstar) and the number of the residue in the chain. For each specific contact, the average equilibrium distance d_i^{eq} with its average fluctuation f_i^{eq} is given.

of their C_α - C_α distances of <0.05 nm. This indicates that they are in stable regions of the protein complex. However, depending on the setup, these contacts separate at certain times in our simulation. A contact is defined as separated if the specific C_α - C_α distance of the contact is increased by 0.5 nm relative to the starting structure of the simulation (Fig. 2). The pathways are characterized by the pulled distances d_1 - d_5 , at which these specific contacts separate. If the contact did not separate during the simulation, the respective distance was set to zero. By analyzing the histograms of distances d_1 - d_5 , the response of the protein complex to force can be described.

Setups 1 and 1_m

In Setups 1 and 1_m, we chose to simulate the experimental, directly-accessible force application of the acting force to single C_α atoms.

We examined the effect of the pulling speed on the unfolding pathways of the probed protein complex. The system was simulated using three different pulling velocities ($v_{\text{fast}} = 2 \frac{\mu\text{m}}{\text{ns}}$, $v_{\text{medium}} = 0.5 \frac{\mu\text{m}}{\text{ns}}$, and $v_{\text{slow}} = 0.125 \frac{\mu\text{m}}{\text{ns}}$). We furthermore tested this setup with two mirrored force vectors: first, the moving potential was acting on Barstar (Setup 1, Fig. 1) and second on Barnase (Setup 1_m).

The pathways chosen in these setups are well described by the distances d_1 and d_2 (Fig. 2). The value d_1 is describing the unfolding of the probed Barstar β -sheet, while d_2 is characterizing the concerted motion of the outermost Barstar α -helix away from the core of the protein complex.

Setup 1

Here, the force is acting on $C_\alpha^{\text{bs}86}$, while $C_\alpha^{\text{bn}7}$ is fixed (*bs*, Barstar; *bn*, Barnase). Two main unfolding pathways and a mixture of the two main pathways were observed (Fig. 3 A, left).

The unfolding of the Barstar β -sheet, described by d_1 , was the main unfolding pathway at v_{fast} . The characteristic contact broke after a pulled distance of 1.7 nm. However, the concerted movement of the Barnase α -helix shearing away from the core of the protein, described by d_2 , was the main event at the slower pulling speeds (v_{medium} and v_{slow}). Here, the contact broke after a pulled distance of

~ 1.4 nm for the medium and at ~ 0.9 nm for the slow pulling velocity. The maximum force on the main pathway are slightly lower than for the alternative pathway (Table 1). With decreasing pulling velocity, the maximum forces decrease. The mixed unfolding pathway was represented by unfolding at both ends of the protein complex, each side being unfolded analogous to one of the main pathways.

Setup 1_m

Here, we used the mirrored probing protocol of Setup 1 (pulling $C_\alpha^{\text{bn}7}$ and fixing $C_\alpha^{\text{bs}86}$).

The Setup 1_m shows only one main unfolding pathway. This unfolding of Barnase from the N-terminus is characterized by a distribution of the unbinding distances $d_2^{\text{fast}} \sim 1.3$ nm, $d_2^{\text{medium}} \sim 1.0$ nm, and $d_2^{\text{slow}} \sim 0.9$ nm (Fig. 3 A, right). The maximum forces during the unfolding decrease, like in Setup 1, with the pulling speed. The average maximum forces are much lower than for Setup 1 (Table 1). Hence, the only speed dependency is shifting the unbinding event to lower pulling distances and lower forces, without switching the unbinding pathway, despite nearly identical simulation parameters.

Setup 2

Here, we used a different SMD simulation scheme and pulled at the center-of-mass (COM) of the two individual proteins (Fig. 1 C). This resulted in drastic changes in the choice of the pathway compared to Setups 1 and 1_m. A different set of specific contacts d_3 to d_5 describes the taken pathways (Fig. 3 B).

The main pathway of the COM pulling in Setup 2 was a two-step process. The two-dimensional histogram of the unbinding distances shows that the structural distortion of Barstar at $d_3 \sim 0.9$ nm is earlier than the unbinding at $d_5 \sim 1.7$ nm (Fig. 3 B). First, an internal rearrangement in Barstar moved the core of the protein away from the binding helix, leaving the binding site intact. This increased the separation d_3 until all side-chain interactions of the Barstar binding-helix with the core of the Barstar protein were broken. Second, the Barstar binding helix began to unbind from the binding pocket of Barnase, starting from its C-terminal end. This caused the partial unbinding of the complex, characterized by d_5 (Fig. 3 B). For medium and slow pulling, all trajectories unbind (all $d_4 > 0$ nm), whereas, at fast pulling speeds, some trajectories were not fully separated at the end of the simulation. Furthermore, for medium and slow pulling velocities, single trajectories show unbinding of the complex without complex distortions ($d_3 = 0$ nm).

Setup 3

In the third setup, the COM of the C_α -atoms of Barstar's binding helix was pulled (Fig. 1 D). This setup was designed to probe the binding site of the Barnase-Barstar complex directly.

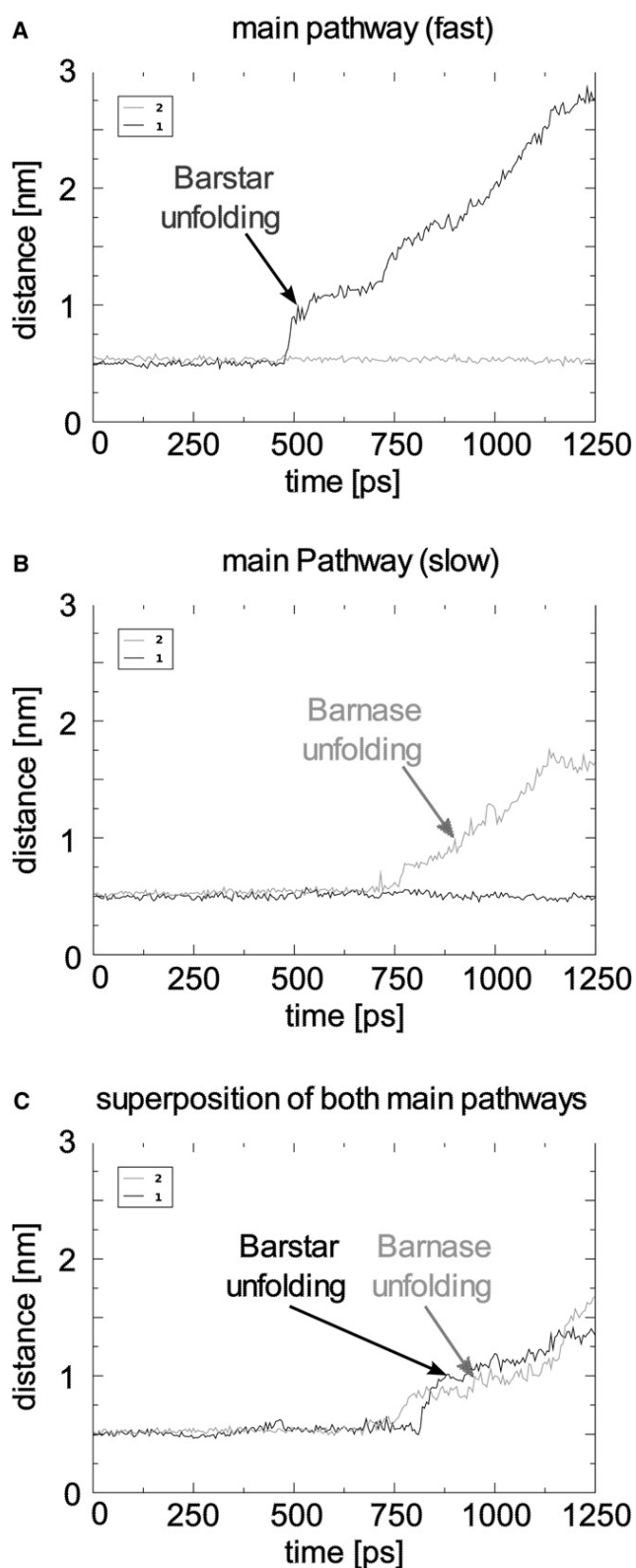


FIGURE 2 Setup 1. These representative distance curves show the development of the unfolding parameters d_1 (black) and d_2 (gray) representing the three different types of pathways taken during the experiment. The arrows mark the first time at which the contact showed an increased separation of

Here, the rupture of the Barnase-Barstar complex was described by a continuous unbinding event. It started at one end of Barstar's binding helix until a fully unbound state was reached. No major distortions in the protein structure of the binding partners were observed.

Unbinding that starts the separation at d_4 or d_5 can be observed. Thus, two unbinding pathways exist. For fast pulling, both pathways are overlapping. For medium pulling, a separation is indicated. For slow pulling, it can be observed in the two populations in the two-dimensional histogram (Fig. 3 C).

The main unbinding pathway shifts from starting separation at the C-terminal end of the Barstar binding helix d_5 at high pulling velocities, to starting with an N-terminal separation (d_4) for medium and slow pulling velocities (Fig. 3 C).

The forces during the trajectory increase to a maximum force of $\langle F_{\max} \rangle \sim 1.8$ nN. The comparison of the maximum forces depending on the selected pathway show no significant differences (Fig. 4 B). The median maximum forces of the major pathway with $\langle F_{\max, 5} \rangle = 1.75$ nN is only slightly smaller than $\langle F_{\max, 4} \rangle = 1.80$ nN for the minor pathway. The ruptures occurred after the maximum force peak (Fig. 4 A). We defined the rupture force in Setup 3 as the force $F(t_{\text{rupt}})$ at the time of the first separation ($t_{\text{rupt}} = \min(t_4, t_5)$). The median of the rupture forces of the major unbinding pathway was $\langle F_5 \rangle = 1056$ pN ($t_5 < t_4$) and, surprisingly, higher than of the minor pathway with $\langle F_4 \rangle = 786$ pN ($t_5 > t_4$) (Fig. 4 C). Since the force describes the slope of the energy landscape, this behavior can be explained with an energy landscape of the unbinding event being an energy funnel with a constantly decreasing slope after the point of the maximum force (Fig. 4 D). Hence, the main unbinding pathway has a steeper slope in the energy landscape at the point of breakage.

Viscous drag forces after separation

After the separation of the complex in Setups 2 and 3, the pulling forces exerted on the protein are needed to move the protein through the water. These drag forces F_{drag} were calculated by averaging the forces only after complete separation (Table 3). Additional drag forces during the actual unbinding process are not investigated. Therefore, the drag forces calculated here are only a lower limit of the drag forces during the separation. The total amount of the friction due to viscous drag forces of ~ 200 pN show that for all pulling velocities, these effects cannot be neglected (Table 3).

A transition from higher to lower drag forces can be seen if the pulling velocity is decreased from fast to medium pulling. No major reduction of the average drag forces can

0.5-nm larger than the equilibrium distance. This time is defined as the separation time t_1 or t_2 . The first graph represents the main pathway at fast pulling (A), whereas the second shows a typical minor pathway that will become important in the medium pulling (B). The third pathway (C) can be described as a superposition of the two main pathways (A and B).

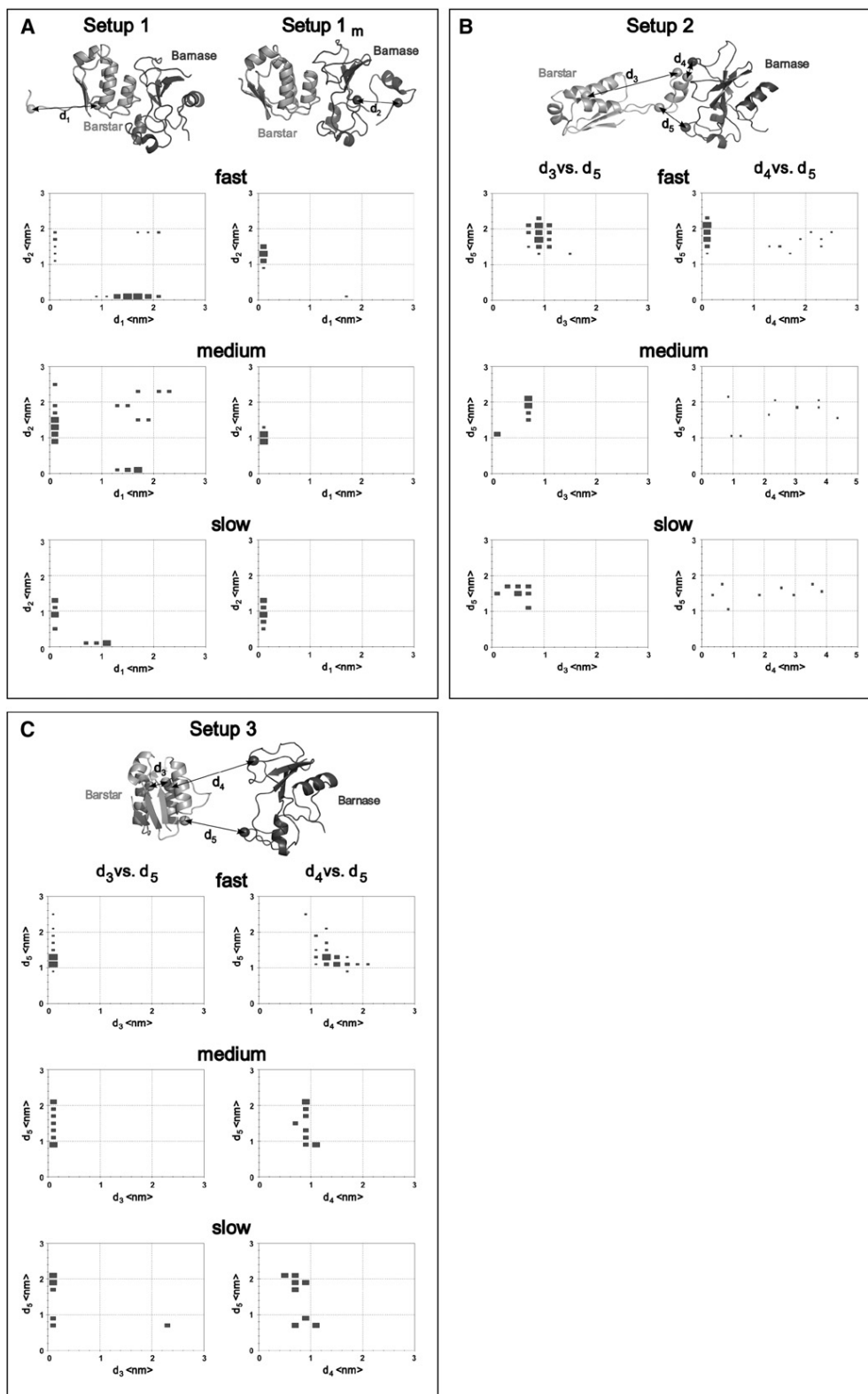


FIGURE 3 The unbinding and unfolding behavior of the Barnase-Barstar complex is shown by a typical snapshot of the unbinding/unfolding structure, as well as by histograms comparing the different pulling distances for the specific contacts d_1 – d_5 to rupture. The size of the boxes in the two-dimensional histograms is proportional to the number of events (binning in both directions is 0.2 nm). (A) Unfolding of Setups 1 and 1_m. (B) Unbinding of Setup 2. (C) Unbinding of Setup 3.

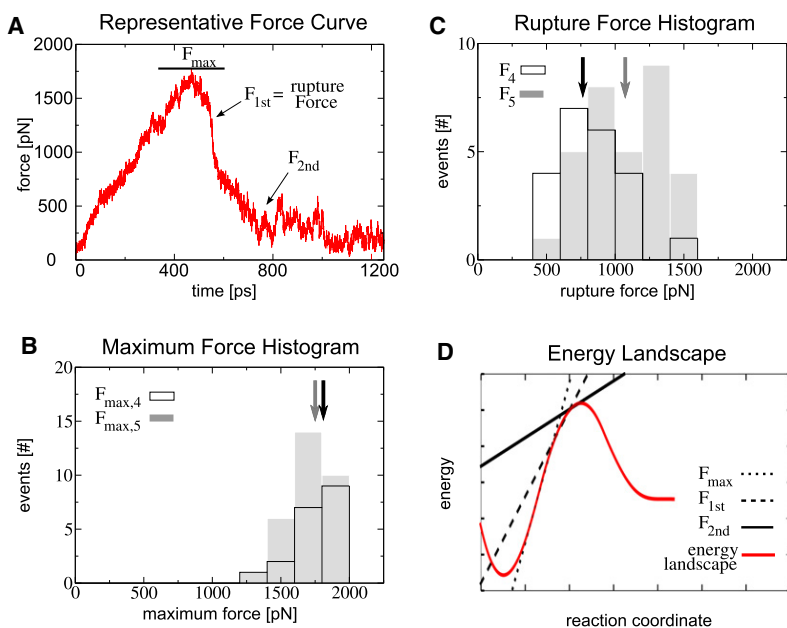


FIGURE 4 Setup 3. (A) Representative force time curve of the unbinding event in Setup 3. The maximum force F_{\max} occurs earlier than the rupture force (F_{1st}), defined by the force at the time of the first separation. The unbinding ends at a force F_{2nd} , which is in the range of the viscous drag forces after the separation. (B) The maximum force histogram shows that major ($F_{\max, 5}$, gray bars) and minor ($F_{\max, 4}$, white bars) pathways are similar. The median maximum forces of the maximum forces are marked as arrows in the histogram. The median of major ($\langle F_{\max, 5} \rangle = 1.75$ nN, gray arrow) and minor ($\langle F_{\max, 4} \rangle = 1.80$ nN, black arrow) pathways were comparable. (C) The rupture forces F_5 (gray bars) of the main pathway were, on average, higher than the rupture forces F_4 (white bars) of the minor pathway. The arrows, denoting the median rupture forces of the major ($\langle F_5 \rangle = 1056$ pN, gray arrow) and minor ($\langle F_{\max, 4} \rangle = 786$ nN, black arrow) pathways, show that for the major pathway higher forces were needed. (D) The continuous unbinding process can be described with a funnel-shaped energy landscape. With increased reaction coordinate, the forces, represented by the slope of the energy profile at a given reaction coordinate, diminish after F_{\max} was reached.

be detected when decreasing the pulling velocity from medium to slow speeds. In contrast to this, the average of the maximum pulling forces for Setups 2 and 3 decrease with every pulling velocity reduction (Table 1). The higher viscous drag forces of Setup 2 compared with Setup 3 during fast pulling can be attributed to the increased surface area of the Barstar in Setup 2 due to the extended protein distortions. However, even though the viscous drag forces are higher in Setup 2, Setup 3 shows the higher average maximum forces.

Effective work of the protein-protein separation

For Setups 2 and 3, the average effective work $\langle W_{\text{eff}}(x) \rangle$ on the protein complex depending on the reaction coordinate x (distance pulled) was calculated (Fig. 5, A and B). For both setups, lower pulling velocities result in lower work due to increased sampling of the energy landscape perpendicular to the reaction coordinate.

The comparison of Setups 2 and 3 shows that the final effective work of separation is comparable (Fig. 5, C–E). The work in Setup 2 is higher due to additional conforma-

tional distortions during the separation of the complex. To separate Barnase and Barstar, Setup 2 requires ~ 1 nm additional pulling distance, which leads to an increase in simulation time of $\sim 66\%$ compared to Setup 3.

DISCUSSION

Free, thermal, and forced unfolding

Free, thermal, and chemical unfolding are different from enforced unfolding (1,10,60). The spontaneous unfolding of Barnase, without the complexing Barstar, was shown to differ from the forced unfolding by the import machinery of the Mitochondria. The spontaneous unfolding starts at the center region of the protein; the forced unfolding starts at the N-terminal end without previously inducing a molten globule state at the import site (1,10), while thermal unfolding induced structural changes within the protein's core (11). These results are in line with our simulations in Setup 1 and Setup 1_m, where for slower pulling we also observe an unfolding starting from the N-terminus of Barstar independent of the force vector.

Barnase-Barstar in comparison to other proteins

AFM experiments on a fusion protein consisting of a Barnase domain fused to titin I27 domains showed that Barnase unfolds at lower forces than the titin domain. The chimera was pulled at the terminal ends of the proteins (11), leading to force vectors analogous to our Setup 1. To compare these experimental results with our simulation, we extrapolated the titin unfolding forces observed in previous simulations to the loading rates of our simulations. All forces were extrapolated due to their logarithmic dependency on the loading rate (9,61),

TABLE 3 The calculated drag forces of the pulled molecules through water after the complete separation of the protein complex

	$\langle F_{\text{drag}} \rangle / \text{pN}$	$\text{stdDev}(\langle F_{\text{drag}} \rangle) / \text{pN}$	No. of separations	No. of trajectories
Setup 2				
Fast	253	25	9	67
Medium	178	10	10	10
Slow	176	22	8	8
Setup 3				
Fast	207	20	55	55
Medium	173	7	10	10
Slow	171	5	8	8

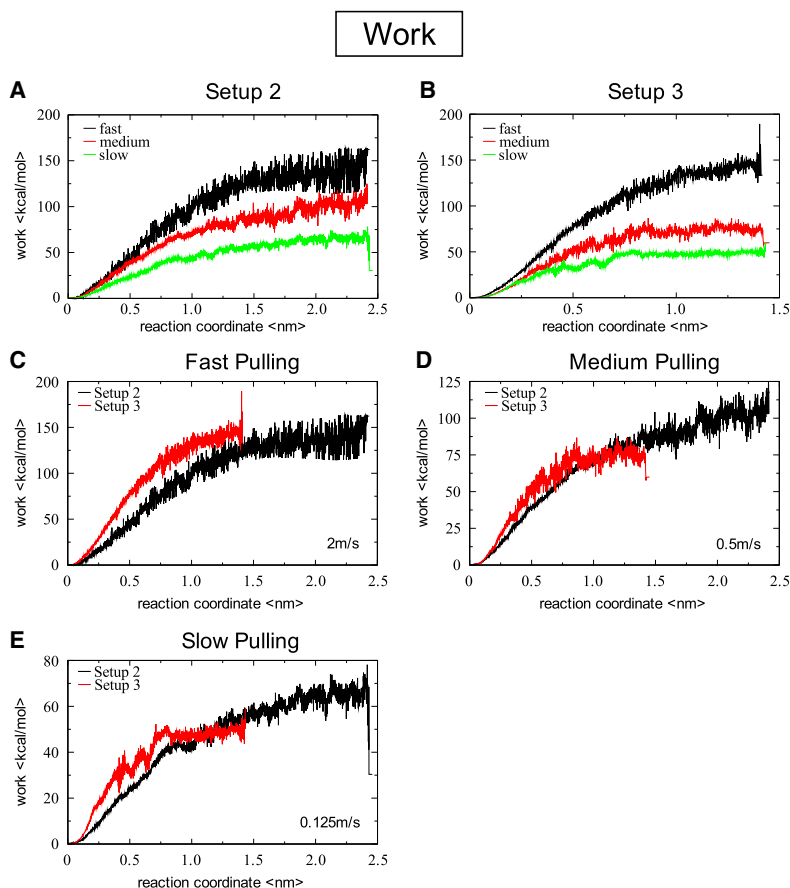


FIGURE 5 The effective work versus the pulled distance as reaction coordinate for Setup 2 (A) and Setup 3 (B) is shown. The work decreases with decreasing pulling velocity from fast pulling at 2 m/s (highest work curve), over medium pulling at 0.5 m/s (middle work curve), to slow pulling at 0.125 m/s (lowest work curve). The separation of the Barnase-Barstar complex is reached at comparable average effective work values for both setups, but for a separation in Setup 2 one needs ~ 1 nm additional pulling compared to Setup 3. The direct comparison of the work in Setup 2 and 3 for fast (C), medium (D), and slow (E) pulling is also shown. (Setup 2 ranges from 0–2.5 nm; Setup 3 from 0–1.5 nm).

$$F_{\text{rupt}} = \frac{k_B T}{\Delta x} \times \ln \left(\frac{v \times \Delta x}{k_{\text{off}}^0 \times k_B T} \right), \quad (3)$$

with the loading rate v , the potential width of the bond Δx , the Boltzmann constant k_B , the temperature T , and the natural off-rate k_{off}^0 . This leads to

$$F_{\text{rupt}}(v_1) - F_{\text{rupt}}(v_2) = \alpha \times \ln \left(\frac{v_1}{v_2} \right) \quad (4)$$

and results in an extrapolation formula for the rupture force of

$$F_{\text{extr}}(v) = \alpha \times \ln \frac{v}{v_1} + F_{\text{rupt}}(v_1) \quad (5)$$

with

$$\alpha = \frac{k_B T}{\Delta x} = \frac{F_{\text{rupt}}(v_1) - F_{\text{rupt}}(v_2)}{\ln \left(\frac{v_1}{v_2} \right)}, \quad (6)$$

where two data points ($v_i, F_{\text{rupt}}(v_i)$) need to be known. The loading rates in Eqs. 5 and 6 are dimensionless.

In agreement with experiment, the average maximum forces of the Barnase unfolding in Setup 1 (951 pN) and Setup 1_m (828 pN) are lower than the extrapolated unfolding forces of the titin domain I27 of 1228 pN (Table 4) (62). Also the unfolding forces of titin domain I1 in its oxidized

($F_{\text{extr}} = 1171$ pN) as well as its reduced form ($F_{\text{extr}} = 1022$ pN) are higher (Table 4). The pull-and-wait pulling protocol by Pabón and Amzel produced an even higher Force peak of 1440 pN (63). Since only one loading rate pair is known, this force was not extrapolated. The energy for the unfolding of the force-transmitting domain I27 of titin ($500 \frac{\text{kcal}}{\text{mol}}$) (64) is much higher than for the unbinding of the Barnase-Barstar system ($< 150 \frac{\text{kcal}}{\text{mol}}$ in Table 5). These data demonstrate the mechanical instability of the Barnase-Barstar system as opposed to the titin family, a family that is designed to operate in a force-exerting environment.

The extrapolated unbinding forces of reported data on Barnase unfolding (11) are comparable to our unbinding forces within the error, if not higher (Table 4). This indicates that due to the N-terminal unfolding of Barnase, the protein is not significantly stabilized by being complexed with Barstar.

Antibody-antigen interactions, where the antigen is a small helical peptide, showed lower unbinding forces compared to our results of Setups 2 and 3, but comparable forces to our unfolding forces (Tables 1 and 4). This demonstrates 1), the high affinity of the Barnase-Barstar complex; and 2), the low mechanical stability of the complex.

The rupture forces observed for the TCR-pMHC complex and cytochrome *c2* exceed the forces observed in our simulations (Table 4) (35,37).

TABLE 4 The unfolding/unbinding forces and loading rates of a variety of simulated and experimental data

System (reference)	Reference	Attachment	Force/pN	Loading rate/ $\frac{\text{pN}}{\text{ns}}$	Extrapolated force/pN
<i>Experimental unfolding</i>					
Barnase AFM	(11)		100	2.1×10^{-6}	
Barstar AFM	(65)		<50		
<i>Simulated unfolding</i>					
Barnase	(11)	C-C	507	1390	968
Barnase	(11)	C-C	269	695	968
Barstar	(65)	C-C	625		
Titin kinase activation	(32)	C-C(2springs)	500	332	988
Titin kinase activation	(32)	C-C(2springs)	1350	41500	988
Titin I27	(62)		2479	145000	1228
Titin I27	(62)		1870	29000	1228
Titin I27	(63)	Pull-and-wait	1440		
Titin I1 oxidized	(62)		2397	145000	1171
Titin I1 oxidized	(62)		1800	29000	1171
Titin I1 reduced	(62)		2090	145000	1022
Titin I1 reduced	(62)		1570	29000	1022
Ubiquitin	(26)	N-Term-C-Term	2000	41420	
Ubiquitin	(26)	Lys48-C-Term	1200	41420	
<i>Simulated deformation</i>					
α -Helix stretching			500		
β -Sheet longitudinal shear	(23)		1000		
β -Sheet lateral shear	(23)		40–120		
α -Helix longitudinal shear	(23)		65–150		
α -Helix lateral shear	(23)		200		
<i>Simulated unbinding in literature</i>					
TCR-pMHC	(37)	Individual	1660		
Streptavidin-biotin	(70)		800		
Antibody-antigen	(36)	C(N-Term)-COM	716	6640	
Antibody-antigen	(36)	C(Middle)-COM	1161	6640	
Antibody-antigen	(36)	C(C-Term)-COM	775	6640	
Cytochrome <i>c</i> 2	(35)	Absolute COM	1500	6943.5	

Extrapolated force peak values at the loading rate of our fast pulling experiments ($v = 5320 \frac{\text{pN}}{\text{ns}}$) were estimated according to Eq. 5. Two data points at different loading rates were used for the extrapolation.

In a biological context, the mechanical instability contrasts the equilibrium affinity of the complex. Under equilibrium conditions, the complex has an extremely low off-rate and virtually never unbinds. The equilibrium stability of the complex poses some conceptual problems: while within the cell, Barnase certainly needs to be complexed to ensure cell survival, and the complex somehow must be opened to export Barnase. The mechanical instability may be needed to unfold the complex during export of Barnase to the extracellular space, which would allow the inhibitor to unbind only at the point of export, and which is consistent with the N-terminal position of the signal peptide. This would pose an interesting balance between different aspects of mechanical-versus-equilibrium stability, which would ensure maximum protection of the cell while allowing for unbinding during export.

Influence of drag force

For fast probing, the complex is unfolding at different ends of the complex (Fig. 3 A) in Setups 1 and 1_m . Since all other parameters are identical, the reason for this different behavior is the opposite direction of the probing force vector.

The pulling force F_{pull} is compensated by the harmonic potential holding the protein (F_{hold}) and the opposing pressure of the solvent F_{solv} (viscous drag). The harmonic potentials (F_{pull} and F_{hold}) are invariant to the pulling direction. Therefore, in the absence of solvent, one would not expect differences between Setups 1 and 1_m . However, the solvent causes a strongly direction-dependent drag force, which is also sensitive to the attachment point of the force.

Due to the viscous drag, $F_{\text{pull}} > F_{\text{hold}}$ under nonequilibrium conditions. Therefore, in Setup 1, $F_{\text{bs}} > F_{\text{bn}}$ and in Setup 1_m , $F_{\text{bn}} > F_{\text{bs}}$. These differences in force caused by drag can explain the observed differences in the trajectories at high loading rates. At lower loading rates, the influence of the drag force is reduced (Table 3), rendering the simulations more similar (Fig. 3). For dual unfolding at both ends, two barriers need to be overcome, reducing the probability of such events.

Distortions in Setups 1 and 1_m

At fast loading rates, due to the unfolding of Barstar's final β -sheet, the structural core of the protein gets disturbed in Setup 1. The concerted motion of the helix away from the

TABLE 5 Computed energies of the Barnase-Barstar and comparable energies found in literature

System	Reference	Energy or work/ kcal/mol
<i>Experimental unfolding</i>		
Barstar free energy of unfolding ΔG	(43)	-5.28
Barnase unfolding stability ΔG	(11)	10.2
<i>Simulated unfolding</i>		
Titin I27 total interaction energy ΔW	(64)	500
<i>Simulated deformation energies</i>		
ΔE of secondary structure elements		
α -Helix stretching	(23)	50
β -Sheet longitudinal shear	(23)	40
β -Sheet lateral shear	(23)	40
α -Helix longitudinal shear	(23)	20
α -Helix lateral shear	(23)	20
Experimental binding energy		ΔG
Barnase-Barstar free energy of binding ΔG	(39)	-19
<i>Simulated unbinding</i>		
		Work ΔW
Barnase-Barstar Setup 2—fast		147
Barnase-Barstar Setup 3—fast		144
Barnase-Barstar Setup 2—medium		106
Barnase-Barstar Setup 3—medium		71
Barnase-Barstar Setup 2—slow		56
Barnase-Barstar Setup 3—slow		51
TCR-pMHC unbinding	(37)	380

structural core of Barnase, in contrast, leaves all the secondary structure elements intact. Only a few contacts between helix and structural core are broken (Fig. 6). The lateral unbinding of the N-terminal helix of Barnase is a gradual, zipperlike process, while the unfolding of the Barstar β -sheet is a catastrophic, cooperative event (Fig. 6). The shearing of a β -sheet has been implicated to be energetically more costly: it has been shown that the lateral shearing of helix pairs (comparable to the shearing away of Barnase's helix observed here) is energetically more favorable than the shearing of β -sheets (Tables 4 and 5) (23). Furthermore, Gräter et al. showed that the probed geometry of β -sheets is very stable (32). Our obser-

vations at slow pulling velocities, where the system has more time to relax orthogonally to the pulling vector and where the unfolding of the Barstar β -sheet is not observed, support this notion. At slower pulling velocities, only the shearing of the helix is observed, being the thermodynamically more favorable process. AFM experiments as well as theoretical considerations showed the mechanical lability of Barnase and Barstar (11,60,65) (Tables 4 and 5), in line with the unfolding observed here. In particular, Barnase was suggested to unfold during mitochondrial import at forces as low as ~ 10 pN (60). Hence, the unfolding of Barnase does not seem to be an artifact of the pulling velocities employed.

Distortions in Setups 2 and 3

To avoid unfolding in the simulations and to gain approximate insight into equilibrium barriers, different simulation schemes need to be employed (37). One possibility would be to go to significantly lower velocities approaching adiabatic conditions, which is hampered by the accompanied computational cost. Recently, Cuendet and Michielin developed an attractive simulation scheme, where the steering force acts only in the direction of the reaction coordinate (37). For the sake of simplicity, we changed the attachment of the probing force and pulled at the centers-of-mass of different groups of the complex. Unbinding simulations of complexes often used larger pulling/attachment groups for avoiding unfolding (35–37).

Attaching the pulling and holding forces to the COM of the molecules distributed the applied tension equally over the whole molecules (Setup 2). Although these simulations are not easily reproduced by AFM measurements, they nevertheless can give insight into aspects of the complex observable by other techniques like double mutant cycle or folding measurements. The resulting structural distortions of the Barstar show that the overall structural integrity of Barstar is weaker than that of Barnase, as also shown experimentally (Table 5).

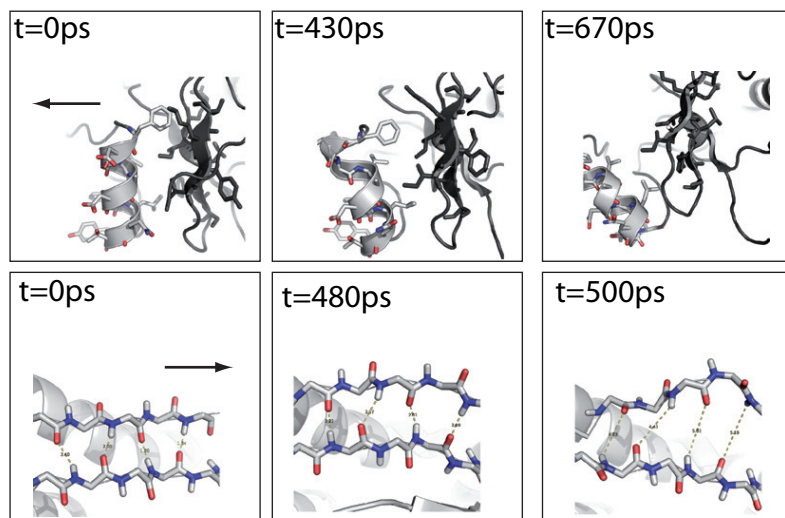


FIGURE 6 The unfolding trajectories of Setups 1 and 1_m are shown. (Upper panel) Shearing of Barnase helix. (Lower panel) Shearing of Barstar sheet. The arrows indicate the direction of the force vector.

We probe here the stability of the binding of this helix to Barnase, relative to the binding strength to its own protein core in a differential force assay. Since the here-probed off-rate of the complex is dominated by van der Waals interactions, our results demonstrate that these interactions of Barstar's binding helix with its own protein core are weaker than the interaction with the active side of the RNase Barnase. In an evolutionary point of view, the blocking of the active site of the Barnase is essential to prevent damage to its parental bacterium, while the interaction of Barstar's binding helix with its own protein core is only necessary for the orientation of its charges in the association process (66,67). These charges destabilized Barstar additionally, facilitating the unfolding of the inhibitor (43), in agreement with our results. For even lower pulling velocities than used here, the distortions will probably not be observed, as indicated by rare events at slow pulling velocities.

Directly addressing the pulling forces to Barstar's binding helix (Setup 3) results in unbinding without structural distortions. The stiffness of the helix (23) distributes the external mechanical tension over the binding interface. The majority of all direct Barnase-Barstar interactions are mediated by this helix.

Unbinding pathways

In Setup 3, unbinding pathways without structural distortions are observed. The high maximum forces (Table 1) point to a very strong binding of the inhibitor to its RNase. A closer examination of the complex unbinding reveals that the main unbinding pathway started separating the complex from the C-terminal end of Barstar's binding helix for fast pulling, and from the N-terminal for medium and slow pulling (Fig. 3 C, right).

For both pathways, the last contacts involve Arg_{bn}59, Asp_{bs}35, and Asp_{bs}39 (Fig. 7). These residues have been implicated to be important for the association pathway of the complex under equilibrium conditions, in particular the loop from residue 57 to residue 60 of Barnase (41,48). This indicates that the observed, enforced dissociation pathways are a good approximation of equilibrium association pathways. Based on Brownian dynamics simulations, the overlap of association and dissociation pathways has been suggested before (51). The agreement of our simulated dissociation pathway with proposed association pathways shows that the probing of the central helix allows us to sample essential barriers of the equilibrium trajectory. Even the effective work of enforced unbinding, with $W_{\text{eff}}^{\text{Setup 3}} = 51 \frac{\text{kcal}}{\text{mol}}$, is only

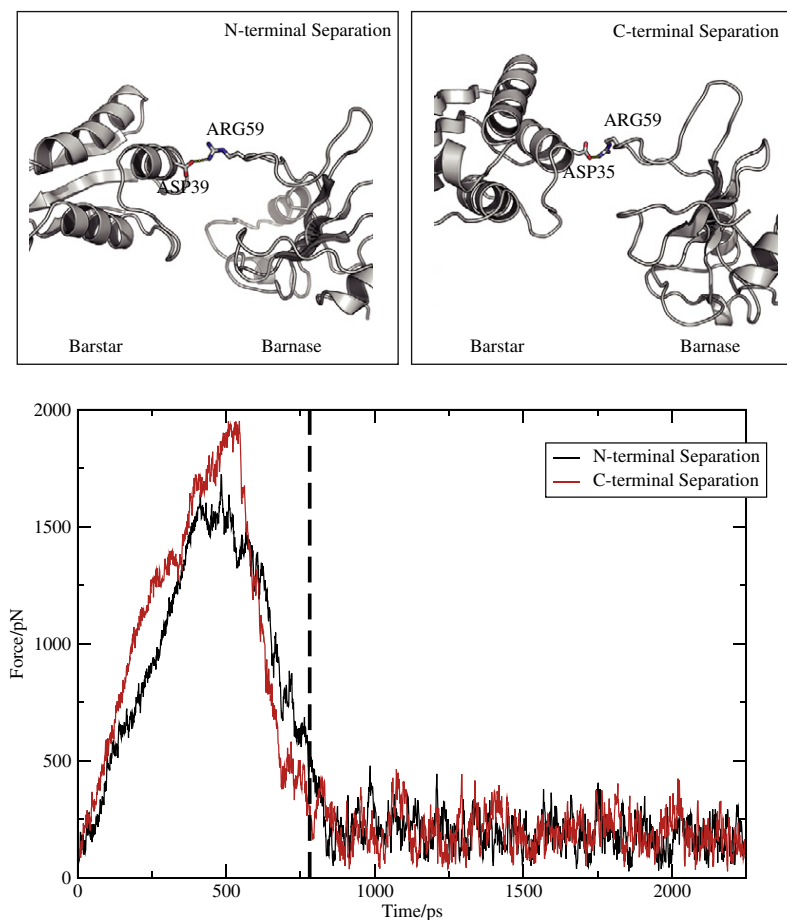


FIGURE 7 Typical last contacts for Setup 3 (upper panel) and the time of separation (dashed line in lower panel) of these last contacts in the force distance trace are shown.

2–3 times the experimentally determined binding energy of the complex of $\delta G_{\text{ass}} = -19 \frac{\text{kcal}}{\text{mol}}$ (39) (Table 5), being thus in a comparable range despite the nonequilibrium nature of our simulations. More complex nonequilibrium simulation schemes of a large protein-protein complex did not reach a better agreement (37). The effective work values of Setups 2 and 3 show that the conformational distortions in Setup 2 require additional work, especially for the faster and medium pulling velocities (Table 5).

We did not attempt to use nonequilibrium analysis schemes like the Jarzynski relation (68). These relations depend on the observation of rare events. The probability of these events becomes negligible with increasing dissipation and system size (69). Standard evaluation schemes use the cumulative expansion of the Jarzynski relation, which is dependent on a Gaussian distribution of work values (69). A Gaussian distribution is not usually observed in simulations with a limited number of trajectories (37).

CONCLUSION

The velocity and geometry of the force application have a strong effect on the evolution of a system. Rapidly changing a system may probe the lability of the energy landscape. This may be very different from slow changes, which test the stability of the system. Furthermore, the different attachment points of force have a severe influence on the final conformation. Summarizing, we showed that an atomistic understanding of unbinding or unfolding pathways needs the application of a variety of force protocols. The applied forces alter the energy landscape in a nontrivial way. The resulting propagation of the probed protein through phase space does not only critically depend on the geometry of force application, but equally on the velocity of force application. Therefore, for a thorough characterization of the effect of force on a protein complex, multiple simulations with different probing geometries and different velocities need to be performed, carefully testing the lability and stability of the system. Sophisticated attachment simulation schemes allow rapid, but approximate insight into the main barriers of the dissociation pathways, deepening our understanding of the observed system and helping in the design of experiments.

We thank R. D. Astumian and M. Höfling for helpful discussions.

Financial support from the Fonds der Chemischen Industrie, the Center for NanoScience, and the International Doctorate Program Nano-Bio-Technology of the Elitenetzwerk Bayern is acknowledged.

REFERENCES

- Huang, S., S. Murphy, and A. Matouschek. 2000. Effect of the protein import machinery at the mitochondrial surface on precursor stability. *Proc. Natl. Acad. Sci. USA.* 97:12991–12996.
- Sukharev, M., Betanzos, C. S. Chiang, and H. Guy. 2001. The gating mechanism of the large mechanosensitive channel MscL. *Nature.* 409:720–724.
- Bershadsky, A. D., N. Q. Balaban, and B. Geiger. 2003. Adhesion-dependent cell mechanosensitivity. *Annu. Rev. Cell Dev. Biol.* 19:677–695.
- Evans, E., A. Leung, V. Heinrich, and C. Zhu. 2004. Mechanical switching and coupling between two dissociation pathways in a P-selectin adhesion bond. *Proc. Natl. Acad. Sci. USA.* 101:11281–11286.
- Gumbart, J., M. C. Wiener, and E. Tajkhorshid. 2007. Mechanics of force propagation in TonB-dependent outer membrane transport. *Biophys. J.* 93:496–504.
- Nevo, R., V. Brumfeld, R. Kapon, P. Hinterdorfer, and Z. Reich. 2005. Direct measurement of protein energy landscape roughness. *EMBO Rep.* 6:482–486.
- Barsegov, V., and D. Thirumalai. 2005. Probing protein-protein interactions by dynamic force correlation spectroscopy. *Phys. Rev. Lett.* 95:168302.
- Kessler, M., K. E. Gottschalk, H. Janovjak, D. J. Muller, and H. E. Gaub. 2006. Bacteriorhodopsin folds into the membrane against an external force. *J. Mol. Biol.* 357:644–654.
- Evans, E., and K. Ritchie. 1997. Dynamic strength of molecular adhesion bonds. *Biophys. J.* 72:1541–1555.
- Huang, S., K. S. Ratliff, M. P. Schwartz, J. M. Spenser, and A. Matouschek. 1999. Mitochondria unfold precursor proteins by unraveling them from their N-termini. *Nat. Struct. Biol.* 6:1132–1138.
- Best, R. B., B. Li, A. Steward, V. Daggett, and J. Clarke. 2001. Can non-mechanical proteins withstand force? Stretching Barnase by atomic force microscopy and molecular dynamics simulation. *Biophys. J.* 81:2344–2356.
- Evans, E., K. Ritchie, and R. Merkel. 1995. Sensitive force technique to probe molecular adhesion and structural linkages at biological interfaces. *Biophys. J.* 68:2580–2587.
- Grubmüller, H., B. Heymann, and P. Tavan. 1996. Ligand binding: molecular mechanics calculation of the streptavidin-biotin rupture force. *Science.* 271:997–999.
- Rief, M., M. Gautel, F. Oesterhelt, J. M. Fernandez, and H. E. Gaub. 1997. Reversible unfolding of individual titin immunoglobulin domains by AFM. *Science.* 276:1109–1112.
- Lu, H., and K. Schulten. 1999. Steered molecular dynamics simulations of force-induced protein domain unfolding. *Proteins.* 35:453–463.
- Oesterhelt, F., D. Oesterhelt, M. Pfeiffer, A. Engel, H. E. Gaub, et al. 2000. Unfolding pathways of individual bacteriorhodopsins. *Science.* 288:143–146.
- Gao, M., D. Craig, V. Vogel, and K. Schulten. 2002. Identifying unfolding intermediates of FN-III(10) by steered molecular dynamics. *J. Mol. Biol.* 323:939–950.
- Grubmüller, H. 2005. Force probe molecular dynamics simulations. *Methods Mol. Biol.* 305:493–515.
- Gao, S., M. Sotomayor, E. Villa, E. H. Lee, and K. Schulten. 2006. Molecular mechanisms of cellular mechanics. *Phys. Chem. Chem. Phys.* 8:3692–3706.
- Kessler, M., and H. E. Gaub. 2006. Unfolding barriers in bacteriorhodopsin probed from the cytoplasmic and the extracellular side by AFM. *Structure.* 14:521–527.
- Vogel, V. 2006. Mechanotransduction involving multimodular proteins: converting force into biochemical signals. *Annu. Rev. Biophys. Biomol. Struct.* 35:459–488.
- Sotomayor, M., and K. Schulten. 2007. Single-molecule experiments in vitro and in silico. *Science.* 316:1144–1148.
- Rohs, R., C. Etchebest, and R. Lavery. 1999. Unraveling proteins: a molecular mechanics study. *Biophys. J.* 76:2760–2768.
- Bryant, Z., V. S. Pande, and D. S. Rokhsar. 2000. Mechanical unfolding of a β -hairpin using molecular dynamics. *Biophys. J.* 78:584–589.
- Brockwell, D. J., E. Paci, R. C. Zinober, G. S. Beddard, P. D. Olmsted, et al. 2003. Pulling geometry defines the mechanical resistance of a β -sheet protein. *Nat. Struct. Biol.* 10:731–737.

26. Carrion-Vazquez, M., H. Li, H. Lu, P. E. Marszalek, A. F. Oberhauser, et al. 2003. The mechanical stability of ubiquitin is linkage dependent. *Nat. Struct. Biol.* 10:738–743.
27. Li, P.-C., and D. E. Makarov. 2004. Simulation of the mechanical unfolding of ubiquitin: probing different unfolding reaction coordinates by changing the pulling geometry. *J. Chem. Phys.* 121:4826–4832.
28. Eyal, E., and I. Bahar. 2008. Toward a molecular understanding of the anisotropic response of proteins to external forces: insights from elastic network models. *Biophys. J.* 94:3424–3435.
29. Gee, E. P. S., D. E. Ingber, and C. M. Stultz. 2008. Fibronectin unfolding revisited: modeling cell traction-mediated unfolding of the tenth type-III repeat. *PLoS ONE.* 3:e2373.
30. Dietz, H., and M. Rief. 2004. Exploring the energy landscape of GFP by single-molecule mechanical experiments. *Proc. Natl. Acad. Sci. USA.* 101:16192–16197.
31. Dietz, H., and M. Rief. 2008. Elastic bond network model for protein unfolding mechanics. *Phys. Rev. Lett.* 100:098101.
32. Gräter, F., J. H. Shen, H. L. Jiang, M. Gautel, and H. Grubmüller. 2005. Mechanically induced titin kinase activation studied by force-probe molecular dynamics simulations. *Biophys. J.* 88:790–804.
33. Puchner, E. M., A. Alexandrovich, A. L. Kho, U. Hensen, L. V. Schäfer, et al. 2008. Mechanoenzymatics of titin kinase. *Proc. Natl. Acad. Sci. USA.* 105:13385–13390.
34. Gräter, F., and H. Grubmüller. 2007. Fluctuations of primary ubiquitin folding intermediates in a force clamp. *J. Struct. Biol.* 157:557–569.
35. Autenrieth, F., E. Tajkhorshid, K. Schulten, and Z. Luthey-Schulten. 2004. Role of water in transient cytochrome *c*2 docking. *J. Phys. Chem. B.* 108:20376–20387.
36. Morfill, J., J. Neumann, K. Blank, U. Steinbach, E. M. Puchner, et al. 2008. Force-based analysis of multidimensional energy landscapes: application of dynamic force spectroscopy and steered molecular dynamics simulations to an antibody fragment-peptide complex. *J. Mol. Biol.* 381:1253–1266.
37. Cuendet, M. A., and O. Michielin. 2008. Protein-protein interaction investigated by steered molecular dynamics: the TCR-pMHC complex. *Biophys. J.* 95:3575–3590.
38. Hartley, R. W. 1989. Barnase and Barstar: two small proteins to fold and fit together. *Trends Biochem. Sci.* 14:450–454.
39. Schreiber, G., and A. R. Fersht. 1995. Energetics of protein-protein interactions: analysis of the Barnase-Barstar interface by single mutations and double mutant cycles. *J. Mol. Biol.* 248:478–486.
40. Schreiber, G., C. Frisch, and A. R. Fersht. 1997. The role of Glu-73 of Barnase in catalysis and the binding of Barstar. *J. Mol. Biol.* 270:111–122.
41. Frisch, C., A. R. Fersht, and G. Schreiber. 2001. Experimental assignment of the structure of the transition state for the association of Barnase and Barstar. *J. Mol. Biol.* 308:69–77.
42. Matouschek, A. 2003. Protein unfolding—an important process in vivo? *Curr. Opin. Struct. Biol.* 13:98–109.
43. Schreiber, G., A. M. Buckle, and A. R. Fersht. 1994. Stability and function: two constraints in the evolution of Barstar and other proteins. *Structure.* 2:945–951.
44. Schreiber, G., and A. R. Fersht. 1996. Rapid, electrostatically assisted association of proteins. *Nat. Struct. Biol.* 3:427–431.
45. Vijayakumar, M., K. Y. Wong, G. Schreiber, A. R. Fersht, A. Szabo, et al. 1998. Electrostatic enhancement of diffusion-controlled protein-protein association: comparison of theory and experiment on Barnase and Barstar. *J. Mol. Biol.* 278:1015–1024.
46. Schreiber, G., Y. Shaul, and K. E. Gottschalk. 2006. Electrostatic design of protein-protein association rates. *Methods Mol. Biol.* 340:235–249.
47. Dong, F., M. Vijayakumar, and H.-X. Zhou. 2003. Comparison of calculation and experiment implicates significant electrostatic contributions to the binding stability of Barnase and Barstar. *Biophys. J.* 85:49–60.
48. Gabdoulline, R. R., and R. C. Wade. 1997. Simulation of the diffusional association of Barnase and Barstar. *Biophys. J.* 72:1917–1929.
49. Gabdoulline, R. R., and R. C. Wade. 2001. Protein-protein association: investigation of factors influencing association rates by Brownian dynamics simulations. *J. Mol. Biol.* 306:1139–1155.
50. Camacho, C. J., Z. Weng, S. Vajda, and C. DeLisi. 1999. Free energy landscapes of encounter complexes in protein-protein association. *Biophys. J.* 76:1166–1178.
51. Spaar, A., C. Dammer, R. R. Gabdoulline, R. C. Wade, and V. Helms. 2006. Diffusional encounter of Barnase and Barstar. *Biophys. J.* 90:1913–1924.
52. Buckle, A. M., G. Schreiber, and A. R. Fersht. 1994. Protein-protein recognition: crystal structural analysis of a Barnase-Barstar complex at 2.0-Å resolution. *Biochemistry.* 33:8878–8889.
53. Lindahl, E., B. Hess, and D. van der Spoel. 2001. GROMACS 3.0: a package for molecular simulation and trajectory analysis. *J. Mol. Model.* 7:306–317.
54. van der Spoel, D., E. Lindahl, B. Hess, G. Groenhof, A. E. Mark, et al. 2005. GROMACS: fast, flexible, and free. *J. Comput. Chem.* 26:1701–1718.
55. Berendsen, H. J. C., J. R. Grigera, and T. P. Straatsma. 1987. The missing term in effective pair potentials. *J. Phys. Chem.* 91:6269–6271.
56. Jorgensen, W. L., D. S. Maxwell, and J. Tirado-Rives. 1996. Development and testing of the OPLS all-atom force field on conformational energetics and properties of organic liquids. *J. Am. Chem. Soc.* 118:11225–11236.
57. Hess, B., H. Bekker, H. J. C. Berendsen, and J. G. E. M. Fraaije. 1997. LINCS: a linear constraint solver for molecular simulations. *J. Comp. Chem.* 18:1463–1472.
58. Berendsen, H., J. Postma, W. van Gunsteren, A. Dinola, and J. Haak. 1984. Molecular dynamics with coupling to an external bath. *J. Chem. Phys.* 81:3684–3690.
59. Ewald, P. P. 1921. Die Berechnung optischer und elektrostatischer Gitterpotentiale. *Ann. Phys.* 64:253–287.
60. Shariff, K., S. Ghosal, and A. Matouschek. 2004. The force exerted by the membrane potential during protein import into the mitochondrial matrix. *Biophys. J.* 86:3647–3652.
61. Friedsam, C., A. K. Wiehle, F. Kuhner, and H. E. Gaub. 2003. Dynamic single-molecule force spectroscopy: bond rupture analysis with variable spacer length. *J. Phys. Cond. Mat.* 15:S1709–S1723.
62. Gao, M., M. Wilmanns, and K. Schulten. 2002. Steered molecular dynamics studies of titin I1 domain unfolding. *Biophys. J.* 83:3435–3445.
63. Pabón, G., and L. M. Amzel. 2006. Mechanism of titin unfolding by force: insight from quasi-equilibrium molecular dynamics calculations. *Biophys. J.* 91:467–472.
64. Lu, H., B. Isralewitz, A. Krammer, V. Vogel, and K. Schulten. 1998. Unfolding of titin immunoglobulin domains by steered molecular dynamics simulation. *Biophys. J.* 75:662–671.
65. Sharma, D., G. Feng, D. Khor, G. Z. Genchev, H. Lu, et al. 2008. Stabilization provided by neighboring strands is critical for the mechanical stability of proteins. *Biophys. J.* 95:3935–3942.
66. Selzer, T., and G. Schreiber. 1999. Predicting the rate enhancement of protein complex formation from the electrostatic energy of interaction. *J. Mol. Biol.* 287:409–419.
67. Selzer, T., S. Albeck, and G. Schreiber. 2000. Rational design of faster associating and tighter binding protein complexes. *Nat. Struct. Biol.* 7:537–541.
68. Chernyak, V., M. Chertkov, and C. Jarzynski. 2005. Dynamical generalization of nonequilibrium work relation. *Phys. Rev. E Stat. Nonlin. Soft Matter Phys.* 71:025102.
69. Park, S., and K. Schulten. 2004. Calculating potentials of mean force from steered molecular dynamics simulations. *J. Chem. Phys.* 120:5946–5961.
70. Izrailev, S., S. Stepaniants, M. Balsera, Y. Oono, and K. Schulten. 1997. Molecular dynamics study of unbinding of the avidin-biotin complex. *Biophys. J.* 72:1568–1581.

The Integrin-Talin Complex under Force

Jan Neumann¹ & Kay-Eberhard Gottschalk^{2*}

- 1) Lehrstuhl für Angewandte Physik, Ludwig-Maximilians-Universität München
2) Lehrstuhl für Experimentelle Physik, Universität Ulm

*corresponding author:

Prof. Dr. Kay E. Gottschalk
Institut für Experimentelle Physik
Universität Ulm
D-89069 Ulm

Tel.: +49 731 50 23012
Fax: +49 731 50 23036
kay.gottschalk@uni-ulm.de

Abstract

Integrins are the major transmembrane (TM) cellular adhesion receptors. They bind the extracellular matrix and transduce forces to the intracellular space. Talin binds to the cytoplasmic β -tail of the integrin with its head domain and links them to the actin cytoskeleton with its rod domain. Hence, the integrin-talin complex acts as the force linkage between the extracellular matrix and the cytoskeleton of the cell. In this study, we show that the associated conformation of the integrin transmembrane domains in the integrins resting state can interact with talin without steric clashes. Therefore, talin binding alone may not be sufficient for integrin activation. However, a small force of 20 pN applied to the integrin talin complex breaks a salt bridge between the integrins α - and β -subunit. The salt bridge has previously been shown to lock the integrin in its resting state. Therefore, we propose that the integrin activation by talin is force-assisted. The application of constant forces in the range of 20 - 500 pN to the integrin-talin complex leads to (partial) dissociation of the complex. The pathway of dissociation depends on the direction of the force vector. Forces parallel to the membrane lead to a zipper-like unbinding. Forces normal to the membrane induce strengthening of the complex by formation of a talin-binding beta strand in the integrin tail. This mechanism strengthens the integrin-talin complex at the leading edge of the cell, where forces normal to the membrane facilitate integrin activation. Our results indicate that the integrin-talin complex is physiologically optimized to be strengthened by applied forces only at certain locations within the cell.

Author Summary

Cells can adhere to the extracellular matrix in the bloodstream, they migrate, and they feel and respond to the mechanical properties of their environment. In all these tasks, cells are either exposed to external forces or exert forces to their environment. This requires protein complexes optimized for withstanding forces. One of these complexes is the intracellular complex of integrin, a cell adhesion receptor, with talin, an adaptor protein that links integrins

to the cytoskeleton and to many signaling molecules. During the mechanical cycle of cell migration, talin needs to bind strongly to integrins at certain location of the cell and to be released from integrins at other locations of the cell. By using computational simulations of the integrin-talin complex under force, we show here that the direction of force application on this vector alters the resistance of this complex to forces. This implies that by altering the vector of forces acting on the complex, the cell can regulate the strength of the complex and tune it to the needs at a specific cellular location.

Introduction

Forces impact biological life on different length scales ranging from whole organisms to individual proteins. Force is a vectorial quantity, which acts directionally on proteins. Its effect on proteins is not only dependent on the magnitude of the force, but also on the direction of the force vector [1-5]. Recently, forces are recognized as important regulatory mechanisms in cellular events like cell adhesion and cell migration [6,7]. Both experiments and computation showed that the extracellular matrix protein fibronectin and the rod domain of the intracellular adaptor protein talin unfold partially under physiological stress to expose hidden binding sites [8,9]. For these force-triggered signaling events, forces must be transduced from the extracellular matrix to the cytoskeleton. The most important family of proteins to transduce forces through the cellular membrane are the integrins. Integrins form mechanical and signaling connections from the extracellular matrix over the talin adaptor proteins to the actin cytoskeleton [10-15].

Integrin affinity to extracellular ligands is regulated by the binding of intracellular adaptor proteins like talin or kindlin [16-21]. The activation of integrins is accompanied by a conformational change of its extracellular domain [22]. This conformational change is triggered by separating the transmembrane helices of the integrins' α - and β -subunit for inside-out signaling [6]. Helix separation is supposedly caused by talin binding to the intracellular domain of the integrin β -subunit, pushing away the α -subunit [23]. Forces have

been identified as an additional regulatory mechanism for the conformation of the integrins extracellular domains, depending on the direction of the applied forces [24].

The integrin-activating protein talin binds the cytoplasmic integrin β -tails predominantly with its FERM domain and actin with its rod domain [25,26]. Hence, talin acts as a force clamp between the integrin and the cytoskeleton. Figure 1A shows schematically how forces are propagated between the extracellular domain and the cytoskeleton through the integrin-talin complex.

Here, we are interested in the effect of forces to the integrin-talin complex. To investigate this, we firstly equilibrate the recently published complex structure of talin-2 FERM F3 domain binding the integrin β_{1D} cytoplasmic tail in a 100 ns molecular dynamics simulation [27]. Alignment of our 100 ns equilibrated structure with the recently solved transmembrane complex of the integrin $\alpha_{IIb}\beta_3$ shows that talin binding does not sterically replace the α -subunit of the integrin complex. Secondly, we probe the integrin- β_{1D} talin-F3 FERM subdomain complex with constant forces in molecular dynamics simulations. Further, we study the impact of forces on this complex. Our simulations show that physiological forces of 20 pN induce a conformational change, which potentially activates the integrin. This is the force range at which the talin rod starts to decrypt its vinculin binding sites [9]. Single molecule force measurements with laser tweezers and atomic force microscopes measured peak rupture forces of the integrin-fibronectin complex of 80-100 pN and 120 pN respectively [28,29]. Since integrin activation timescales are in the order of seconds, our simulations feature higher forces (up to 500 pN) to speed up dissociation processes.

Applying constant force in different directions, we identify the sequence of intermediate dissociation states for forces parallel and normal to the membrane. For forces normal to the membrane we observe a force induced strengthening of the integrin-talin complex. This is caused by the formation of a force-resistant β -sheet between talin and integrin. We further show that when free to rotate the complex orients such that the force vector allows the formation of this β -sheet. This constitutes a self-enforcing mechanism of the integrin-talin bond.

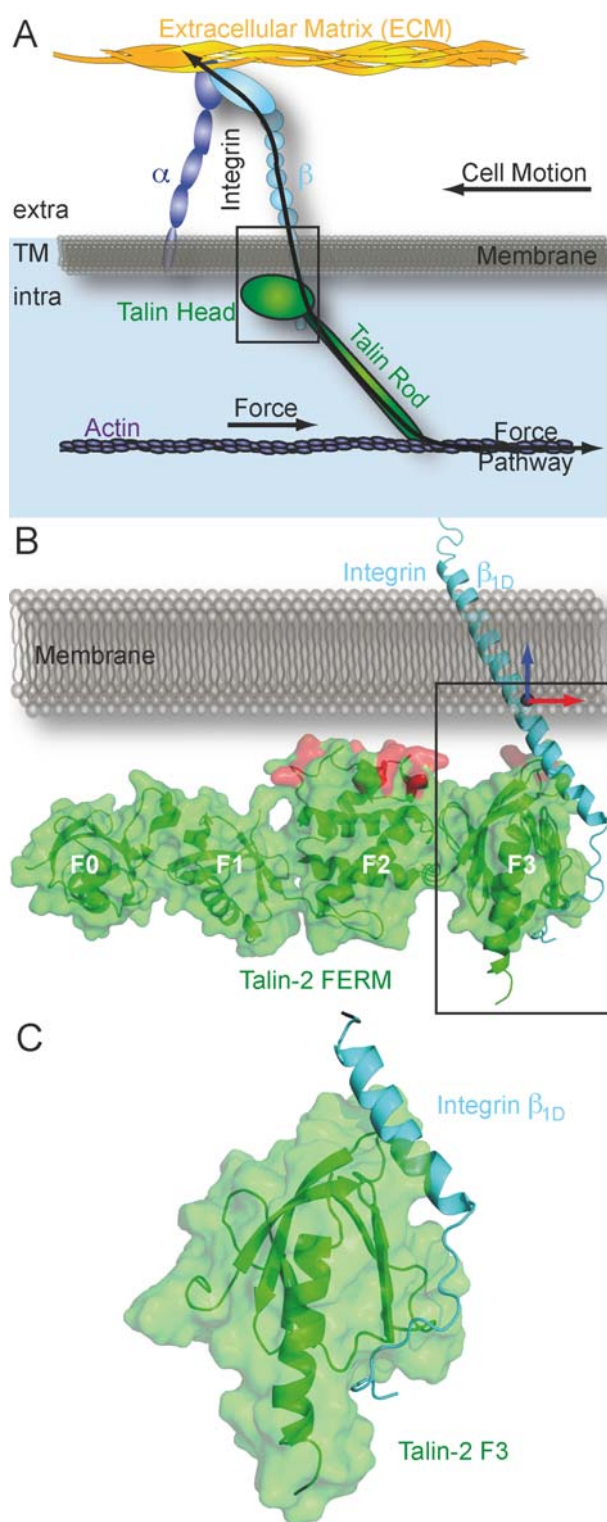


Figure 1: (A) Schematic of force linkage from cytoskeleton (violet) to the extracellular matrix (orange) through the talin (green) integrin (cyan/blue) complex. The blue box indicates the structure in (B). (B) Structural representation of the talin-2 FERM domain (green) binding the cytoplasmic tail of the integrin β_{1D} -tail. The transmembrane region of the β_3 integrin (pdb:2K9J) is fitted to the structure. The membrane binding talin residues of F2&F3 are highlighted in red. The plane of the membrane is added as grey box. The C $_{\alpha}$ -atom to which constant force was applied during simulations is marked as black sphere. The force vectors normal (blue) and parallel (red) to the membrane are indicated. The blue box highlights the simulated structure shown in (C). (C) Representative structure of the most populated cluster during complex equilibration of the talin-2 F3 (cyan) integrin β_{1D} -tail (green) complex.

Results

Equilibrium Simulation

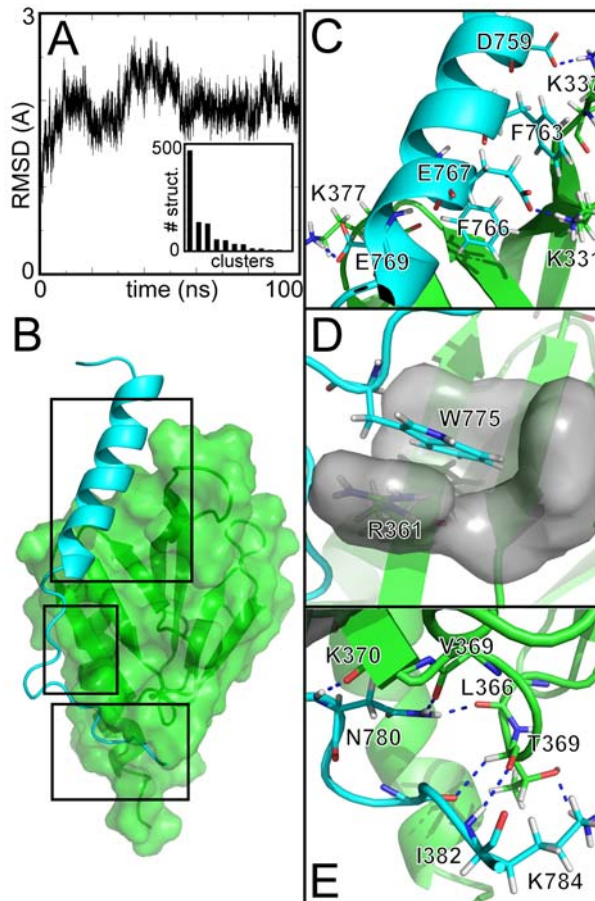


Figure 2: (A) The graph shows the root mean square displacement (rmsd) of the C_{α} -Atoms of the protein. The inlay shows the sizes of the largest clusters resulting from clustering of the equilibration.

(B) Representative structure of the most populated cluster of 100 ns equilibration of the talin-2 F3 (green) integrin β_{1D} -tail (cyan) complex. The black boxes indicate the positions of the zoom in graphs (C-E).

Here, we study the interface of the integrin-talin complex consisting of the cytoplasmic integrin β_{1D} -tail bound to the talin-2 F3 FERM subdomain. Figure 1B highlights the position of the simulated system in context with the membrane position and the complete talin-2 FERM domain. Figure 2A shows the time-development of the root mean square displacement (RMSD) of the C_{α} -atoms of the protein. The 100 ns equilibrium simulation reaches a stable plateau at an RMSD of ~ 0.2 nm (Figure 2a). The structures from the equilibration run are clustered. One cluster dominates (Figure 2a - inset). A representative conformation of this cluster has been chosen as start conformation for further simulations. Based on the analysis of the root mean square fluctuations of the individual amino acids during the equilibrium simulation, the binding interface of the simulated complex can be divided into three modular

regions. The first is the integrin's membrane proximal helix region. It is stabilized by hydrophobic interactions of the phenylalanines β_{1D} -F⁷⁶³ and β_{1D} -F⁷⁶⁶ as well as by the hydrogen bonds of the charged amino acids β_{1D} -D⁷⁵⁹, β_{1D} -E⁷⁶⁷ and β_{1D} -E⁷⁶⁹ (Figure 2C). The second region is located at the integrin tryptophane β_{1D} -W⁷⁷⁵. This tryptophane is bound into a deep hydrophobic binding pocket and may be additionally stabilized via a cation- π interaction with the talin's β_{1D} -R³⁶¹ (Figure 2D). The third region stabilizes the integrin β_{1D} -⁷⁸⁰NPIY⁷⁸³ motif via a network of hydrogen bonds (Figure 2E). All those tight binding amino acids show low root mean square fluctuation (RMSF) during the 100 ns equilibration of the talin-2 F3 integrin β_{1D} complex (Figure 3A). The regions between the integrins' binding modules have higher flexibility and may therefore be of less importance for binding. To further analyse the importance of these residues, we perform a multiple sequence alignment. The tight binding amino acids are highly conserved, underlining the importance for integrity of the complex (Figure 3B).

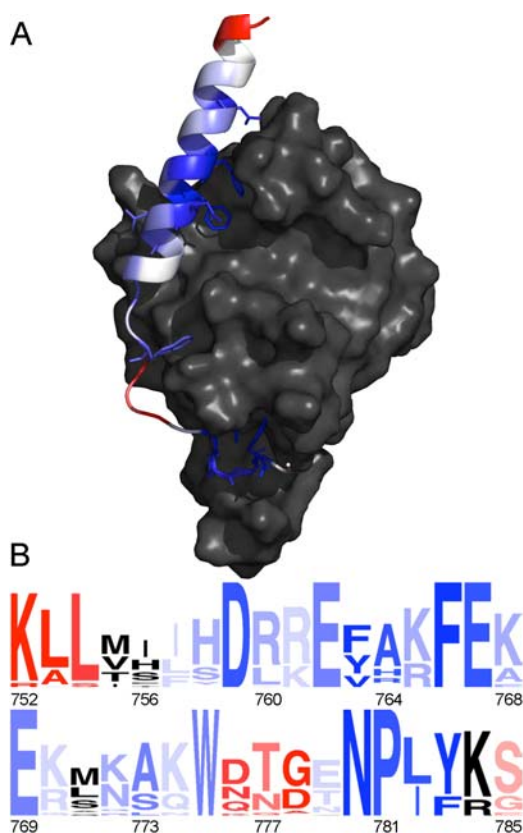


Figure 3: (A) Average amino acid root mean square fluctuations (RMSF) of 100 ns free equilibration color coded onto structure (red=high, white=intermediate and blue=low RMSF). (B) The integrin's amino acid sequence is colored according to its conservation like in 3A (except for white being replaced by black). The height of the letters indicates their evolutionary conservation.

To analyze our simulated fragment in a larger structural context, we align current structures of the transmembrane complex of integrin $\alpha_{IIb}\beta_3$ [27] and of the whole talin FERM domain [30] with our simulated fragment of the the talin-2 F3/integrin β_{1D} complex (Figure 4). Surprisingly, the talin head binding to the integrin β -tail does not sterically disturb the binding between the integrin's α - β -TM-helices.

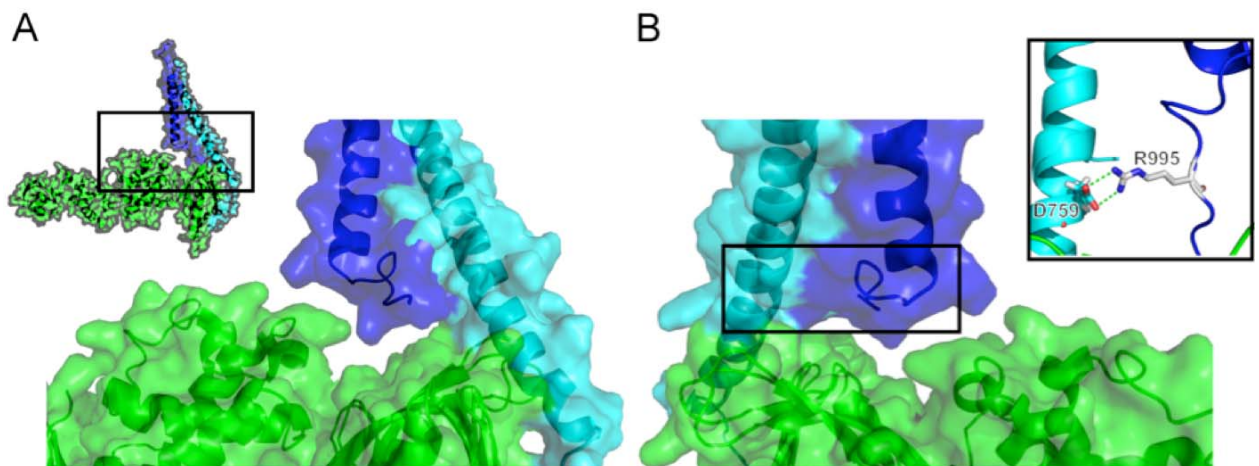


Figure 4: The figures show the talin (green) binding the integrin β -tail (cyan). (A) and (B) show both sides of the complex. The talin does not interfere with the integrin α -tail (blue). Inlay in (A) shows the position of the zoomed in structures. Inlay (B) shows an essential transmembrane salt-bridge.

Directional Force Probing Simulations

The full-length integrin structure continues N-terminally through the membrane to its ECM binding site. The C-terminus of the talin F3 domain is attached through the talin rod domain to the actin cytoskeleton of the cell. Cellular forces acting on the cytoskeleton are transduced through the integrin-talin complex to the ECM (Figure 1A). Applying 20 pN between the integrin's C- and the talin's N-terminus to reproduce physiological conditions lead to talin F3 subdomain rotation, if the forces are applied end-to-end in a direction parallel to the putative

plane of the membrane (Figure 5). After rotation, the forces correspond to a vector normal to the putative plane of the membrane. No rotation is observed if the forces are applied normal to the plane of the membrane (Figure 5). Hence, in the absence of a membrane the complex orients itself such that forces normal to the putative plane of the membrane act on it. A rotational movement may be hampered in the cell by interactions with the cell membrane and stabilizing influence of the F2 FERM domain. Furthermore, we are interested in the question how different force vectors influence the complex. Therefore, to prevent talin from rotation, we constrained the C_{α} -atoms of the talin F3 domain by a weak force. The constant force is applied only to the integrin N-terminus.

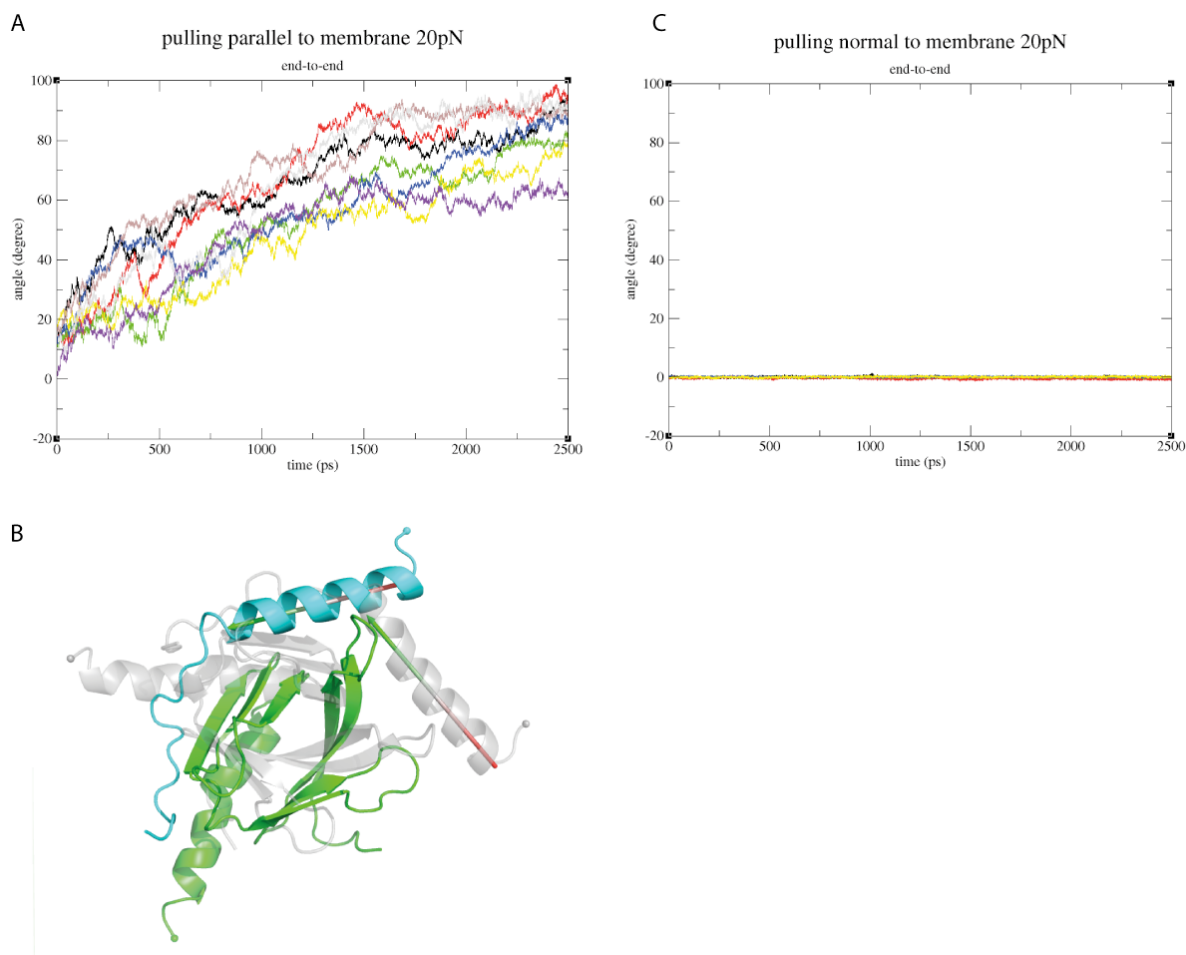


Figure 5: Effect of different force vectors to the relative orientation of the complex over time. A&C: Angle of the vector between the N-terminal C_{α} of Integrin and the C-terminal C_{α} of Talin during 2.5 ns of simulation at a force of 20 pN is shown with respect to the vector at time zero. B: The rotation of the complex during parallel force application is shown.

Constant forces between 20 and 500 pN are applied parallel (P) and normal (N) to the putative plane of the cell membrane (Fig. 2B). To analyze the enforced dissociation, we have

chosen the integrin-talin COM-COM distance as a reaction coordinate. Figures 6C and D show its time evolution for all trajectories at 200 pN for normal and parallel forces. From these time traces normalized histograms are generated. The normalized histograms of the integrin-talin COM-COM distances are calculated for each probing force and direction (Figures 6A and B). The peaks indicate stable intermediate states. The ground state shows a stable and sharp probability distribution at 20 - 50 pN for normal pulling. The parallel pulling is less stable and already starts destabilizing at 50 pN.

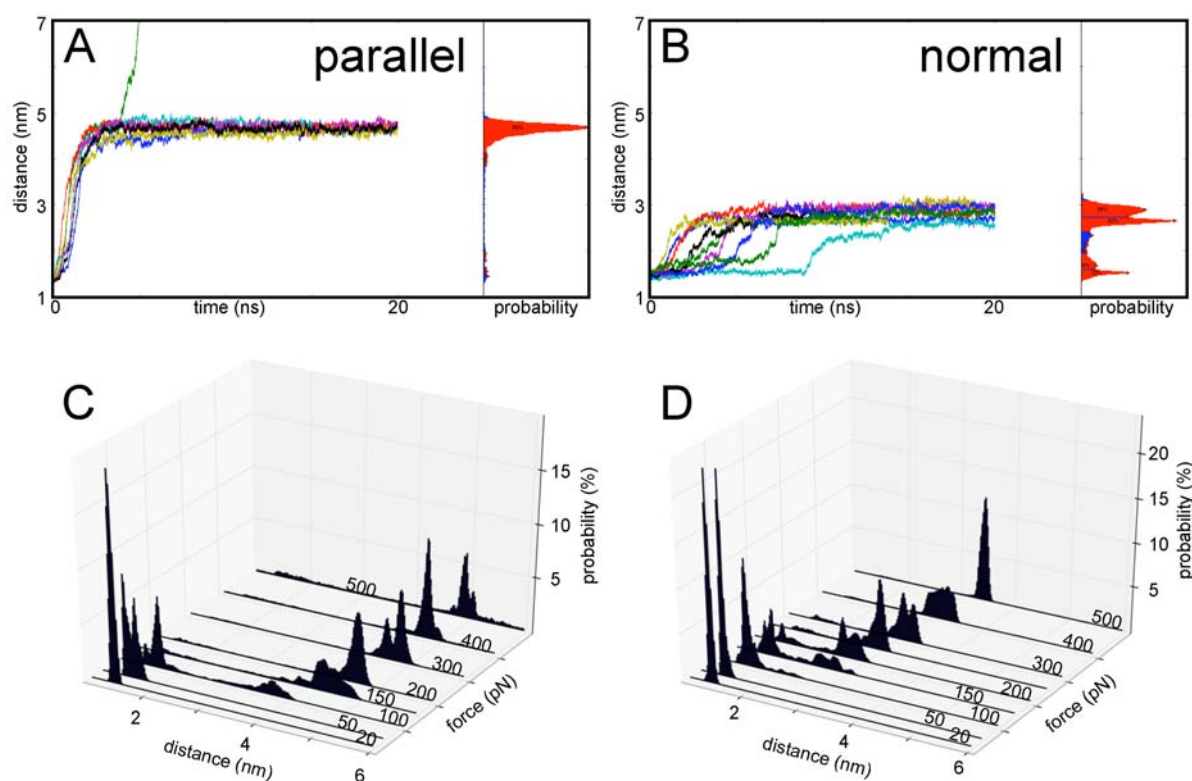


Figure 6: (A) and (B) show the reaction coordinate for multiple trajectories at 200 pN as well as the corresponding histograms for parallel and normal pulling respectively. The red areas in the histograms were identified as regions representing different dissociation states. (C) and (D) show the probability histograms of the talin integrin COM-COM distance depending on the applied constant force for parallel and normal pulling respectively.

Both setups show two prominent intermediate peaks before dissociation. The dissociation within 20 ns starts at 200 pN for parallel forces and at 400 pN for normal forces. Thus, the talin integrin complex is more resistant to the application of forces normal to the plane of the membrane.

To understand the dependence of the complex stability on the direction of the force, we reconstructed the dissociation pathways. The states are determined by an automated peak detection in the COM-COM histograms for each force at each probing direction. A representative structure for each peak is obtained. Based on these structures we reconstruct the dissociation pathways (Figures 7 and 8).

Figure 7: Force dissociation pathway with force parallel to membrane

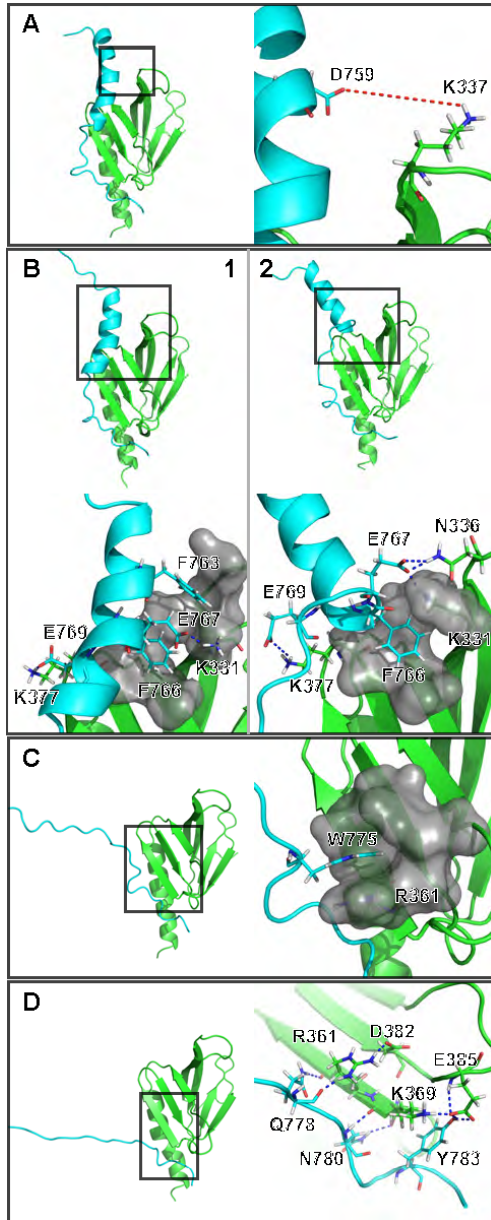
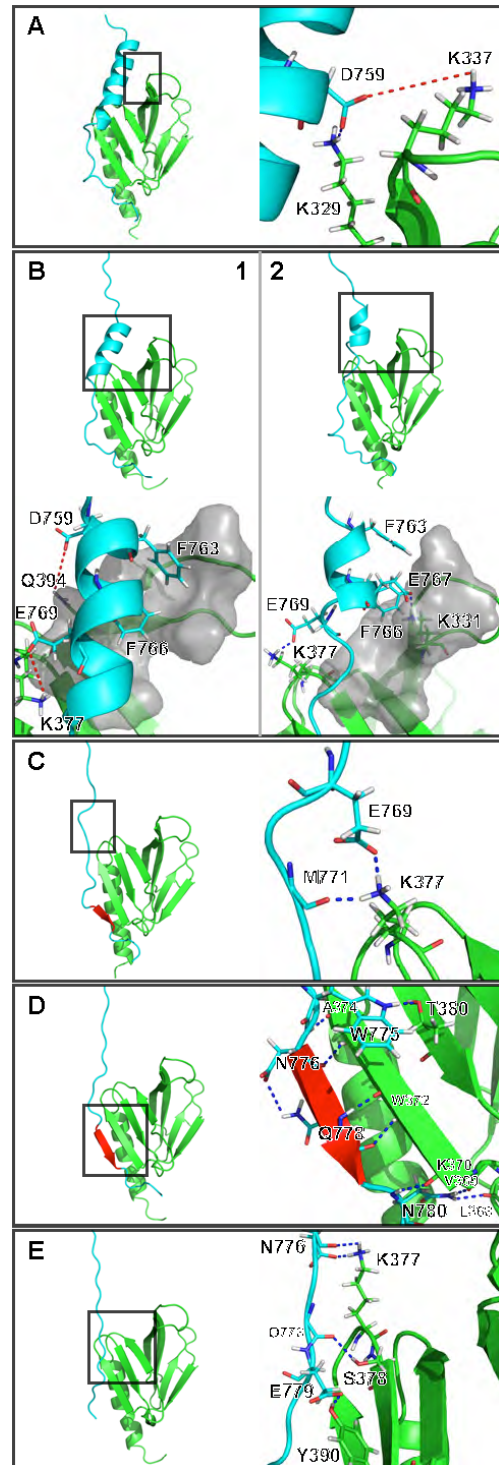


Figure 8: Force dissociation pathway with force normal to membrane



Figures 7 and 8: each box shows the general state of the protein complex with a box marking the position of the zoom in figure with the important amino acids and their labels. Hydrogen bonds are shown in blue. Opened hydrogen bonds are indicated in red. Gray surfaces represent van-der-Waals surfaces.

Dissociation Pathway under Forces Parallel to Membrane

Forces parallel to the membrane cause the integrin dissociation from the talin in four main steps (Figure 7). First, the integrin helix bends away from the talin and the H-bond between $\beta_{1D}\text{-D}^{759}$ and F3-K^{337} ruptures (Fig. 7A). For the second step, two pathways exist: either the N-terminal integrin helix loop unfolds (Fig. 7B-1) or the integrin helix dissociates cooperatively (Fig 7B-2). For this cooperative dissociation $\beta_{1D}\text{-E}^{767}$ to $\beta_{1D}\text{-E}^{769}$ form a hinge axis around which the helix rotates. The $\beta_{1D}\text{-F}^{763}$ unbinds from its hydrophobic talin binding pocket. Third, the integrin helix dissociates completely and the $\beta_{1D}\text{-W}^{775}$ binding site is probed directly (Fig. 7C). Stable $\beta_{1D}\text{-W}^{775}$ binding to its pocket can be observed up to 100 pN. After the unbinding of the $\beta_{1D}\text{-W}^{775}$ the hydrogen bond network around the $\beta_{1D}\text{-}^{780}\text{NPxY}^{783}$ motif (Fig 7D) is the only binding module left. The integrin residues $\beta_{1D}\text{-Q}^{778}$, $\beta_{1D}\text{-N}^{780}$ and $\beta_{1D}\text{-Y}^{783}$ each bind to talin by at least two H-bonds. Thus, each has an increased rebinding probability if one hydrogen bond ruptures. The talin F3-R^{361} directly couples F3-D^{382} to $\beta_{1D}\text{-Q}^{778}$ and the $\beta_{1D}\text{-Y}^{783}$ H-bond network connects to F3-K^{369} and F3-E^{385} . Thus, forces can be distributed to multiple strands of the talin molecule in parallel.

In the integrin-talin COM-COM time trace in Figure 6A, the last plateau corresponds to the state in which only the integrin's NPxY motif is bound. At 200 pN the plateau is reached after 2-3 ns, but only one out of seven trajectories shows total dissociation within 20 ns. Thus, the hydrogen bond network around the NPxY motif is the most stable binding module in this setup.

Normal dissociation pathway

Applying forces normal to the membrane causes a different dissociation behavior. Five steps lead to dissociation. Two pathways are found.

First, the $\beta_{1D}\text{-D}^{759}$ unbinds from F3-K^{337} and - in contrast to parallel force application - rebinds to F3-K^{329} (Fig 8A). The second step shows again two possible pathways: either the hydrophobic interaction of the phenylalanines $\beta_{1D}\text{-F}^{763}$ and $\beta_{1D}\text{-F}^{766}$ (Fig. 8B-2) or the hydrogen bonds of the glutamic acids $\beta_{1D}\text{-E}^{767}$ and $\beta_{1D}\text{-E}^{769}$ (Fig 8B-1) are stable. The two N-

terminal integrin helix loops as well as the β_{1D-D}^{759} unbind in either case. In case of stable hydrogen bonds, the axis β_{1D-E}^{767} to β_{1D-E}^{769} acts as a hinge to allow a reorientation of the integrin helix along the direction of the force. The C-terminal loop of the helix opens to allow this rotation.

In the third step, the integrin helix dissociates completely except for the β_{1D-E}^{769} still binding to F3-K³⁷⁷. The integrin helix is now completely unfolded. This N-terminal integrin tail aligns with the force direction. This allows the β_{1D-M}^{771} backbone to bind to the F3-K³⁷⁷. Here, the applied mechanical work is partly dissipated into the talin. The β_{1D-W}^{775} binding site is probed partially, but the integrin's flexible $\beta_{1D-}^{776}DTQ^{778}$ loop is not yet stretched. This allows the β_{1D-Q}^{778} to induce a β -sheet binding with the talin (Fig 8C red).

Next, F3-K³⁷⁷ and then β_{1D-W}^{775} unbind. Stable β_{1D-W}^{775} binding in the hydrophobic pocket can be found up to 250pN. After its dissociation the integrin tail is stretched along the talin. This reorientation facilitates the growth of the β -sheet between talin and integrin (Fig 8D). In addition, the β_{1D-W}^{775} can form an additional stabilizing hydrogen bond to F3-T³⁸⁰. The combination of the talin integrin β -sheet binding and the three hydrogen bonds of the β_{1D-N}^{780} to talin form a very stable complex. Complete dissociation of the integrin-talin complex within 20 ns starts only at 400 pN.

After the first dissociation of the talin integrin complex, the integrin shows rebinding to the talin via four hydrogen bonds (Figure 8E). Again F3-K³⁷⁷ is very important. This state is short lived.

Discussion

The integrin-talin interaction is an essential part of the force transduction network from the ECM to the cellular cytoskeleton (Figure 1). Here, we highlight two main aspects resulting from our simulations. First, we discuss the structural alignment of talin-head binding to the integrin TM helix bundle without distortions. Second, we show that the integrin-talin complex can be understood as a sensor of the direction of the applied forces important for cellular motion.

Structural Discussion

Integrins bi-directionally signal across the cell membrane. This involves TM helix dissociation [31-34], which then causes conformational changes in the integrins extracellular domain [24,35]. Recently, the structure of the integrin $\alpha_{IIb}\beta_3$ -TM complex has been solved [27]. This complex is stabilized by the inner membrane clasp consisting of two main interactions. These are the inter-helical hydrophobic core $\alpha_{IIb}^{992}FF^{993}$ with β_3-W^{715} and the salt bridge $\alpha_{IIb}-R^{995}$ to β_3-D^{723} . This salt bridge is thought to be disrupted by the F3 talin head binding to the integrin tail [23,36]. In our work, we create a structural model encompassing the integrin α - β -TM-helices and the complete talin head. This model shows that the talin head domain can bind the integrin α - β -TM-helix bundle without disturbing the inner membrane clasp interactions. Therefore, a purely sterical mechanism of activation may not be sufficient. The $\beta_{1D}-D^{759}/F3-K^{337}$ interaction can cause a conformational change to replace the $\alpha_{IIb}-R^{995}/\beta_3-D^{723}$ salt bridge as suggested earlier [36]. Hence, talin offers competing interaction partners and with this thermodynamically de-stabilizes the integrin TM complex. Yet, the energetic difference between a $\beta_{1D}-D^{759}/F3-K^{337}$ and a $\alpha_{IIb}-R^{995}/\beta_3-D^{723}$ is probably small, which might cause not complete structural re-arrangements. Therefore, further mechanisms enhancing such a mechanism may be desirable. Our simulations show that the integrin helix loops connecting the two essential amino acids β_3-W^{715} and β_3-D^{723} are one of the first regions of secondary structures to unfold even at the physiologically low forces of 20 pN. This may in fact be a lower estimate of the forces needed, since stabilizing membrane components are missing. In a context of an intact TM complex of the integrins' α - and β -subunits, this unfolding would disrupt the α - β -TM-helix interactions (Figure 9). Therefore, a small force applied to the integrin-talin complex results in the breakage of the salt bridge $\alpha_{IIb}-R^{995}$ to β_3-D^{723} . This destabilizes the integrins' α - β -TM-helix interactions. Hence, our results indicate that full integrin activation is facilitated by a small force acting at the integrin talin complex. The rotation of the talin head by $\sim 20^\circ$ to enable the binding of talin's positively charged residues to the cell membrane proposed earlier causes a mechanical stress. This stress might already be sufficient to cause the required forces for integrin activation [36,37].

In addition, forces acting normal to the membrane enable β_3 -D⁷²³ to bind to F3-K³²⁹. This hydrogen bond is more stable at higher forces (up to 50 pN) than the initial β_{1D} -D⁷⁵⁹/F3-K³³⁷ interaction.

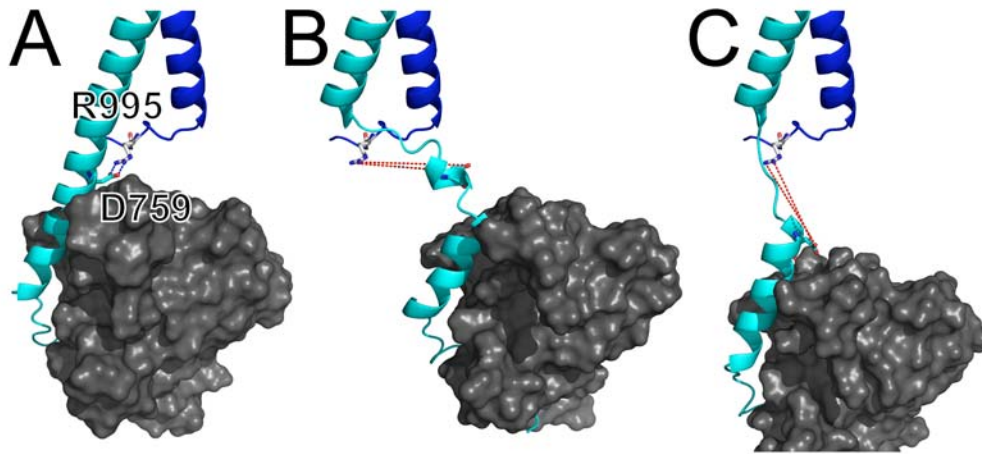


Figure 9: (A) Integrin α -TM helix (blue) binds integrin β -TM-helix (cyan). Outer salt bridge β_{1D} -D⁷⁵⁹ to α_{1b} -R⁹⁹⁵ shown as sticks. Both parallel (B) and normal (C) forces open salt bridge (red lines).

Force response of the talin integrin complex

Integrins are the major force sensors of cells. They convert the physical stimulus ‘force’ into a biochemical signal. How the forces stimulate cellular responses is still debated. Talin is one of the key players in force sensing [11,38-40]. It has been proposed that forces applied to talin lead to local unfolding which exposes hidden binding sites [9]. Previously, Puklin-Faucher et al. proposed that force applied to the integrin-talin complex can both activate and de-activate the integrins [41]. During this cycle, forces activate integrins in the leading edge, while they de-activated them in the trailing edge.

Our results show that the complex dissociation under force depends on the direction of the applied force. The complex dissociation is more stable against pulling normal to the membrane than parallel to it. Under physiological conditions, this effect would be enhanced by the attractive coulomb interactions between talin and the phospholipids of the cell membrane [30]. Since the binding free energy of a complex does not change with the unbinding force direction, the integrin-talin complex has direction dependent binding and unbinding barriers.

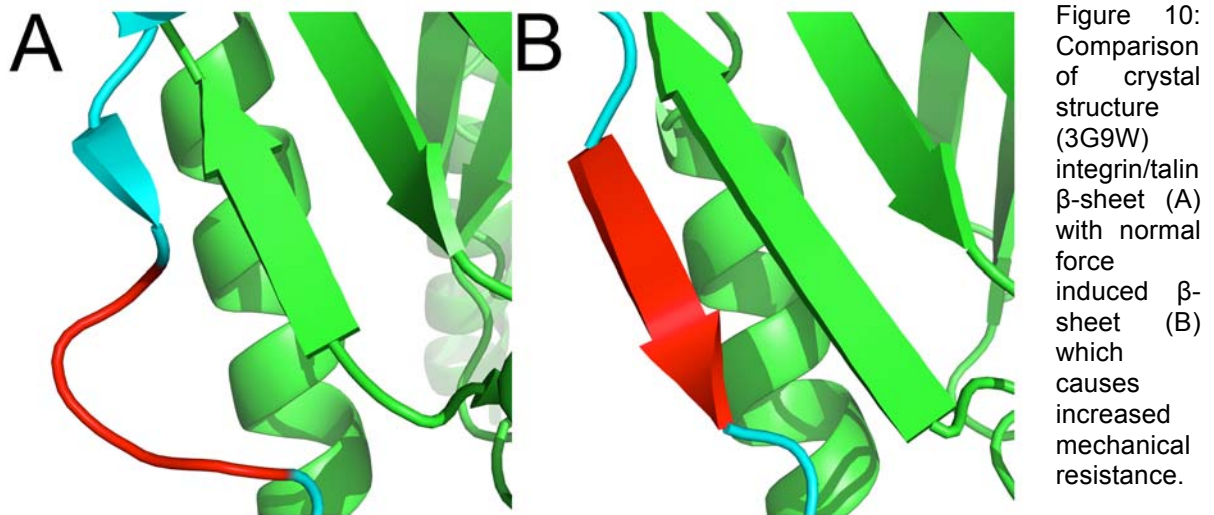
We will discuss the three modular interaction sites of the integrin-talin complex individually before the general biological implications are considered (Figure 2).

The membrane proximal integrin helix is bound via the hydrophobic interactions of $\beta_{1D}\text{-F}^{763}$ and $\beta_{1D}\text{-F}^{766}$ as well as via hydrogen bonds of $\beta_{1D}\text{-D}^{759}$, $\beta_{1D}\text{-E}^{767}$ and $\beta_{1D}\text{-E}^{769}$. All these are highly conserved and their low fluctuations indicate strong binding (Figure 3B). The corresponding hydrophobic interactions for the β_3 -integrin tail were found to be important for activation in the first chimerical structure of the membrane proximal integrin β_3 -tail binding to the talin-1 F3-domain [23]. The higher stability in normal force setups at low forces results from the rebinding of the $\beta_{1D}\text{-D}^{759}$ to another lysine F3-K³²⁹. The hydrogen bonds of the $\beta_{1D}\text{-E}^{767}$ and $\beta_{1D}\text{-E}^{769}$ are strong enough, that they can act as a hinge region in case of a cooperative unbinding of the integrin helix. This hinge region would be a reasonable mechanism for the cooperative rotation of the integrin helix by $\sim 20^\circ$ as proposed in the integrin activation by Anthis et al. [36].

The membrane distal region has two modular binding sites separated by the very flexible $\beta_{1D}\text{-}^{776}\text{DTQ}^{778}$ loop: the $\beta_{1D}\text{-W}^{775}$ and the $\beta_{1D}\text{-}^{780}\text{NPIY}^{783}$ region (Figure 2). The tryptophane $\beta_{1D}\text{-W}^{775}$ is bound in its hydrophobic pocket and may be stabilized by a cation- π interaction with the parallel F3-R³⁶¹ [25,42]. The $\beta_{1D}\text{-W}^{775}$ binding site is again direction dependent. Forces parallel to the membrane pull the tryptophane on the most direct way out of its binding pocket. For normal forces the binding can resist 2.5 times higher forces. This may result from pulling the tryptophane into the direction of the wall instead of out of its binding pocket.

The binding module around the NPxY motif consists of many hydrogen bonds and is very stable in both pulling directions. Mutational studies underline the importance of this region: the mutation Y782A abolishes binding [43]. The fundamental key interaction is the force induced formation of a β -sheet between integrin and talin (Figure 10). It is initiated by $\beta_{1D}\text{-Q}^{778}$ if normal forces are applied. Such a β -sheet is known to be very force resistant if probed in a shear modus. A prominent example would be the direction dependent force resistant of the ubiquitin [44-46]. The most recent discovery of biological proteins using β -sheets for force

resistance is the spider silk [47,48]. Here, we describe for force-induced binding strengthening. Our results further show that, if free to rotate, the complex orients such that this enforcement of the complex is possible. Hence, the integrin-talin complex is optimized as a self-re-enforcing complex. Interestingly, mutations very close to this region drastically improve the affinity of the integrin β_{1D} - talin-2 complex [43].



Integrins are activated in the lamellipodium. Here, forces act on the cell membrane due to the fast assembly of actin pushing the cell membrane forward and the actin network backwards [49,50]. These retrograde forces are necessary to initiate focal complexes [51]. The direction of the forces necessary for activation of the integrins is currently under discussion. While some recent simulations showed an activating conformational change with forces diagonal to the membrane [24]. Puklin-Faucher et al. argument that forces normal to the membrane are required [41]. The angle of the force transduction changes with the distance of the adhesion site to the lamellipodium. This is caused because the speed of the actin network changes as the focal adhesion mature and the actin flow slows down [51]. Recent iPalm measurements recaptured in Figure 9 show the same angle dependence of the talin linkage between integrin and actin [15]. Our simulations show that the talin integrin complex has the intrinsic ability to react to different force vectors with a force induced strengthening of the complex. Thus, for the activation of the integrin in the leading edge, which requires forces normal to the membrane, the integrin-talin complex is strengthened by the formation of a force resistant β -sheet between integrin and talin. With time, the integrin

adhesion matures. The total force resistance in mature focal adhesions may be increased by ligands. All integrins not part of a focal adhesion as well as many nascent adhesion sites are deactivated. Our mechanism predicts, that for non-reinforced integrins, the unbinding is facilitated if the integrins are probed more parallel to the membrane as further away from the lamellipodium. This mechanism adds a molecular description to the mechanical cycle of integrins [41]. Hence, we show that the initial integrin-talin complex senses the distance to the lamellipodium due to the direction of applied force.

In our simulations, as well as in recent structures of the complex, a membrane component is missing. This membrane might be important for further stabilization of the complex through favorable electrostatic interactions between talin and the cell membrane as well as the integrin helix being anchored in the membrane. The effect of the membrane will be tested in future computational studies involving membrane components.

Conclusion

We have shown, that the talin head binding to the integrin does not sterically disturb the integrin to force a dissociation of the integrins α - β -TM-helices. Further, we propose a model in which small forces cause a stretching of the integrin β_{1D} 's membrane proximal helix. This stretching leads to the dissociation of the essential salt bridge α_{11b} -R⁹⁹⁵ to β_3 -D⁷²³ between the integrin's α -/ β -TM helices. Thus, it facilitates an inside-out activation of the integrin.

Our simulations show force induced strengthening of the complex for forces normal to the membrane by the formation of a β -sheet between the complex partners. The directional dependence of the force resistance of the integrin-talin bond supports the biological needs for strong nascent adhesion in the leading edge and easily de-activated integrins in the rear of the cell.

Methods

Structure

The studied integrin-talin complex consists of the cytoplasmic integrin β_{1D} -tail and the talin-2 F3 FERM subdomain. A subset of the 3G9W structure [27] without the talin F2 FERM subdomain is used to optimize for computational speed.

Molecular Dynamics Simulations

All MD simulations are done using the software package GROMACS Version 4.05-4.07 [52-55] with periodic boundary conditions using the OPLS-AA force field [56]. The structure is solvated in SPC water [57] with 150mMol NaCl. The energy is minimized using steepest descent method with a maximum step size of 0.01nm. The water has been relaxed for 200 ps while the heavy atoms of the protein have been restrained by a strong harmonic potential of 1.66 nN/nm. The electrostatics for the position restraint simulation is calculated using a 1nm Coulomb cutoff. Solvent and protein are separately coupled to external heat baths at 300K with a time constant of 0.1ps using Berendsen temperature coupling [58].

Afterwards, the system is equilibrated without restraints for 100 ns resulting in a stable complex. The equilibration structures every 100 ps are clustered using the gromos clustering method of the Gromacs MD software package [59] with a RMSD cutoff of 0.15 nm. The representative structure of the dominating cluster is used as an initial structure for further simulations.

Figure 2A shows the structure of the talin-2 F3 FERM subdomain (red) binding the integrin β_{1D} -tail (green) resulting from 100 ns free equilibration. The RMSF shown in Figure 3A is determined using `g_rmsf` from the Gromacs MD software package.

Structure Alignment

The fully equilibrated structure is aligned with the integrin TM α_{11b} - β_3 -bundle (2K9J) [27] and the complete talin head domain (3IVJ) [30] binding the integrin β_{1D} -tail. All alignments

are made to the equilibrated structure using pymol alignment. The resulting model is shown in Figures 2B and 4.

Setup Structures

The simulation boxes are generated by resolving the representative equilibrated structure (Figure 2B) in different water boxes for each type of pulling setup. For each box, energy minimization, position restraint and a 200 ps long free equilibration simulation analog to the one previously described are done. Each constant force molecular dynamics simulation is preceded by another 100 ps free equilibration with freshly initiated velocity profiles.

Constant Force Molecular Dynamics Simulations

Constant forces in the range of 20 pN to 500 pN are simulated. The forces are applied to the integrin's C-terminal C_{α} -atom is probed with a constant force either parallel (P) or normal (N) to the putative plane of the cellular membrane. The plane of the membrane is perpendicular to the connection from integrin's C-terminal to talin's N-terminal C_{α} -atoms. In Figure 1B the force vectors are indicated. The positively charged membrane binding talin residues are indicated in red. To these residues a plane can be fitted which is the approximately parallel to the putative plane of the membrane. To avoid rotations of the talin, all C_{α} -atoms of the talin complex are restrained with a weak position restrained (400 pN/nm).

Representative Structures

For each setup at each force the probability distribution of the integrin-talin COM-COM distances is generated. The extrema of these distributions are determined. All structures with COM-COM distances between to minima are attributed to the peak in between these minima. Their structures are added to one trajectory. Each peak represents a (semi)stable intermediate state. For all peaks with at least 8% population, the representative structure is determined by clustering approximately 1000 equally distributed structures within the trajectory corresponding to the peak. The gromos clustering method is used with a cutoff of

0.3nm and three required nearest neighbors [59]. From these representative structures the dissociation pathways for normal and parallel forces are determined.

Evolutionary Conservation

For the determination of the evolutionary conservation of the integrin residues, 27 mammalian integrin beta sequences ($\beta_1, \beta_2, \beta_3, \beta_6, \beta_7$) from the UniProtKB database are aligned to the β_{1D} sequence of our structure using ClustalW [60]. The sequence logo visualization of the conservation is done with weblogo 2.8.2 [61,62].

References

1. Li P-C, Makarov DE (2004) Simulation of the mechanical unfolding of ubiquitin: probing different unfolding reaction coordinates by changing the pulling geometry. *J Chem Phys* 121: 4826-4832.
2. Dietz H, Rief M (2004) Exploring the energy landscape of GFP by single-molecule mechanical experiments. *Proc Natl Acad Sci U S A* 101: 16192-16197.
3. Dietz H, Berkemeier F, Bertz M, Rief M (2006) Anisotropic deformation response of single protein molecules. *Proc Natl Acad Sci U S A* 103: 12724-12728.
4. Gee EPS, Ingber DE, Stultz CM (2008) Fibronectin unfolding revisited: modeling cell traction-mediated unfolding of the tenth type-III repeat. *PLoS ONE* 3: e2373.
5. Neumann J, Gottschalk K-E (2009) The effect of different force applications on the protein-protein complex Barnase-Barstar. *Biophysical Journal* 97: 1687-1699.
6. Luo B-H, Springer TA, Takagi J (2004) A specific interface between integrin transmembrane helices and affinity for ligand. *PLoS Biol* 2: e153.
7. Alon R, Dustin ML (2007) Force as a facilitator of integrin conformational changes during leukocyte arrest on blood vessels and antigen-presenting cells. *Immunity* 26: 17-27.
8. Smith ML, Gourdon D, Little WC, Kubow KE, Eguiluz RA, et al. (2007) Force-induced unfolding of fibronectin in the extracellular matrix of living cells. *PLoS Biol* 5: e268.
9. del Rio A, Perez-Jimenez R, Liu R, Roca-Cusachs P, Fernandez JM, et al. (2009) Stretching single talin rod molecules activates vinculin binding. *Science* 323: 638-641.
10. Critchley DR (2000) Focal adhesions - the cytoskeletal connection. *Curr Opin Cell Biol* 12: 133-139.
11. Geiger B, Bershadsky A, Pankov R, Yamada KM (2001) Transmembrane crosstalk between the extracellular matrix--cytoskeleton crosstalk. *Nat Rev Mol Cell Biol* 2: 793-805.
12. Hynes R (2002) Integrins:: Bidirectional, Allosteric Signaling Machines. *Cell* 110: 673-687.
13. Moes M, Rodius S, Coleman SJ, Monkley SJ, Goormaghtigh E, et al. (2007) The integrin binding site 2 (IBS2) in the talin rod domain is essential for linking integrin beta subunits to the cytoskeleton. *J Biol Chem* 282: 17280-17288.
14. Schmitz J, Gottschalk K (2008) Mechanical regulation of cell adhesion. *Soft Matter* 4: 1373-1387.
15. Kanchanawong P, Shtengel G, Pasapera AM, Ramko EB, Davidson MW, et al. (2010) Nanoscale architecture of integrin-based cell adhesions. *Nature* 468: 580-584.
16. Tadokoro S, Shattil SJ, Eto K, Tai V, Liddington RC, et al. (2003) Talin binding to integrin beta tails: a final common step in integrin activation. *Science* 302: 103-106.
17. Calderwood DA (2004) Talin controls integrin activation. *Biochem Soc Trans* 32: 434-437.
18. Arnaout MA, Goodman SL, Xiong J-P (2007) Structure and mechanics of integrin-based cell adhesion. *Curr Opin Cell Biol* 19: 495-507.
19. Moser M, Nieswandt B, Ussar S, Pozgajova M, Fässler R (2008) Kindlin-3 is essential for integrin activation and platelet aggregation. *Nat Med* 14: 325-330.
20. Wegener KL, Campbell ID (2008) Transmembrane and cytoplasmic domains in integrin activation and protein-protein interactions (review). *Mol Membr Biol* 25: 376-387.
21. Moser M, Legate KR, Zent R, Fässler R (2009) The tail of integrins, talin, and kindlins. *Science* 324: 895-899.

22. Takagi J, Petre B, Walz T, Springer T (2002) Global conformational rearrangements in integrin extracellular domains in outside-in and inside-out signaling. *Cell* 110: 599-611.
23. Wegener KL, Partridge AW, Han J, Pickford AR, Liddington RC, et al. (2007) Structural basis of integrin activation by talin. *Cell* 128: 171-182.
24. Zhu J, Luo B-H, Xiao T, Zhang C, Nishida N, et al. (2008) Structure of a complete integrin ectodomain in a physiologic resting state and activation and deactivation by applied forces. *Mol Cell* 32: 849-861.
25. Garcia-Alvarez B, Pereda JMd, Calderwood DA, Ulmer TS, Critchley DR, et al. (2003) Structural determinants of integrin recognition by talin. *Mol Cell* 11: 49-58.
26. Tanentzapf G, Brown NH (2006) An interaction between integrin and the talin FERM domain mediates integrin activation but not linkage to the cytoskeleton. *Nat Cell Biol* 8: 601-606.
27. Lau T-L, Kim C, Ginsberg MH, Ulmer TS (2009) The structure of the integrin α IIb β 3 transmembrane complex explains integrin transmembrane signalling. *EMBO J* 28: 1351-1361.
28. Li F, Redick SD, Erickson HP, Moy VT (2003) Force measurements of the α 5 β 1 integrin-fibronectin interaction. *Biophysical Journal* 84: 1252-1262.
29. Litvinov R, Shuman H, Bennett J, Weisel J (2002) Binding strength and activation state of single fibrinogen-integrin pairs on living cells. *Proceedings Of The National Academy Of Sciences Of The United States Of America* 99: 7426-7431.
30. Elliott PR, Goult BT, Kopp PM, Bate N, Grossmann JG, et al. (2010) The Structure of the talin head reveals a novel extended conformation of the FERM domain. *Structure* 18: 1289-1299.
31. Hughes PE, Diaz-Gonzalez F, Leong L, Wu C, McDonald JA, et al. (1996) Breaking the integrin hinge. A defined structural constraint regulates integrin signaling. *J Biol Chem* 271: 6571-6574.
32. Kim H, Arakawa H, Osada T, Ikai A (2003) Quantification of cell adhesion force with AFM: distribution of vitronectin receptors on a living MC3T3-E1 cell. *Ultramicroscopy* 97: 359-363.
33. Gottschalk K-E (2005) A coiled-coil structure of the α IIb β 3 integrin transmembrane and cytoplasmic domains in its resting state. *Structure* 13: 703-712.
34. Li W, Metcalf DG, Gorelik R, Li R, Mitra N, et al. (2005) A push-pull mechanism for regulating integrin function. *Proc Natl Acad Sci U S A* 102: 1424-1429.
35. Xiao T, Takagi J, Collier BS, Wang J-H, Springer TA (2004) Structural basis for allostery in integrins and binding to fibrinogen-mimetic therapeutics. *Nature* 432: 59-67.
36. Anthis NJ, Wegener KL, Ye F, Kim C, Goult BT, et al. (2009) The structure of an integrin/talin complex reveals the basis of inside-out signal transduction. *EMBO J* 28: 3623-3632.
37. Kalli AC, Wegener KL, Goult BT, Anthis NJ, Campbell ID, et al. (2010) The structure of the talin/integrin complex at a lipid bilayer: an NMR and MD simulation study. *Structure* 18: 1280-1288.
38. Galbraith CG, Yamada KM, Sheetz MP (2002) The relationship between force and focal complex development. *The Journal of cell biology* 159: 695-705.
39. Giannone G, Jiang G, Sutton DH, Critchley DR, Sheetz MP (2003) Talin1 is critical for force-dependent reinforcement of initial integrin-cytoskeleton bonds but not tyrosine kinase activation. *J Cell Biol* 163: 409-419.
40. Vogel V, Sheetz M (2006) Local force and geometry sensing regulate cell functions. *Nat Rev Mol Cell Biol* 7: 265-275.
41. Puklin-Faucher E, Sheetz MP (2009) The mechanical integrin cycle. *J Cell Sci* 122: 179-186.
42. Gallivan JP, Dougherty DA (1999) Cation- π interactions in structural biology. *Proceedings Of The National Academy Of Sciences Of The United States Of America* 96: 9459-9464.

43. Anthis NJ, Wegener KL, Critchley DR, Campbell ID (2010) Structural diversity in integrin/talin interactions. *Structure* 18: 1654-1666.
44. Gellman SH (1998) Minimal model systems for beta sheet secondary structure in proteins. *Curr Opin Chem Biol* 2: 717-725.
45. Brockwell DJ, Paci E, Zinober RC, Beddard GS, Olmsted PD, et al. (2003) Pulling geometry defines the mechanical resistance of a beta-sheet protein. *Nat Struct Biol* 10: 731-737.
46. Carrion-Vazquez M, Li H, Lu H, Marszalek PE, Oberhauser AF, et al. (2003) The mechanical stability of ubiquitin is linkage dependent. *Nature Structural Biology* 10: 738-743.
47. Cetinkaya M, Xiao S, Gräter F (2011) Bottom-up computational modeling of semi-crystalline fibers: from atomistic to continuum scale. *Physical chemistry chemical physics : PCCP* 13: 10426-10429.
48. Cetinkaya M, Xiao S, Markert B, Stacklies W, Gräter F (2011) Silk fiber mechanics from multiscale force distribution analysis. *Biophysical Journal* 100: 1298-1305.
49. Raucher D, Sheetz MP (2000) Cell spreading and lamellipodial extension rate is regulated by membrane tension. *The Journal of cell biology* 148: 127-136.
50. Dubin-Thaler BJ, Hofman JM, Cai Y, Xenias H, Spielman I, et al. (2008) Quantification of Cell Edge Velocities and Traction Forces Reveals Distinct Motility Modules during Cell Spreading. *PLoS ONE* 3: e3735.
51. Alexandrova AY, Arnold K, Schaub S, Vasiliev JM, Meister J-J, et al. (2008) Comparative dynamics of retrograde actin flow and focal adhesions: formation of nascent adhesions triggers transition from fast to slow flow. *PLoS ONE* 3: e3234.
52. Berendsen H, Van der Spoel D, Drunen Rv (1995) GROMACS: a message-passing parallel molecular dynamics implementation. *Computer Physics Communications*: 43-56.
53. Lindahl E, Hess B, Van der Spoel D (2001) GROMACS 3.0: a package for molecular simulation and trajectory analysis. *J Mol Model* 7: 306-317.
54. Van der Spoel D, Lindahl E, Hess B, Groenhof G, Mark A, et al. (2005) GROMACS: Fast, flexible, and free. *Journal Of Computational Chemistry* 26: 1701-1718.
55. Hess B, Kutzner C, van der Spoel D, Lindahl E (2008) GROMACS 4: Algorithms for highly efficient, load-balanced, and scalable molecular simulation. *Journal of Chemical Theory and Computation* 4: 435-447.
56. Jorgensen WL, Maxwell DS, TiradoRives J (1996) Development and testing of the Opls all-atom force field on conformational energetics and properties of organic liquids. *Journal Of The American Chemical Society* 118: 11225-11236.
57. Berendsen H, Postma J, Gunsteren Wv, Hermans J (1981) Interaction models for water in relation to protein hydration. *Intermolecular Forces*.
58. Berendsen H, Postma J, VANGUNSTEREN W, Dinola A, Haak J (1984) MOLECULAR-DYNAMICS WITH COUPLING TO AN EXTERNAL BATH. *Journal of Chemical Physics* 81: 3684-3690.
59. Daura X, Gademann K, Jaun B, Seebach D, van Gunsteren W, et al. (1999) Peptide folding: When simulation meets experiment. *Angew Chem Int Edit* 38: 236-240.
60. Larkin MA, Blackshields G, Brown NP, Chenna R, McGettigan PA, et al. (2007) Clustal W and Clustal X version 2.0. *Bioinformatics* 23: 2947-2948.
61. Schneider TD, Stephens RM (1990) Sequence logos: a new way to display consensus sequences. *Nucleic Acids Res* 18: 6097-6100.
62. Crooks GE, Hon G, Chandonia J-M, Brenner SE (2004) WebLogo: a sequence logo generator. *Genome Res* 14: 1188-1190.

Driving and controlling molecular surface rotors with a Terahertz electric field

Jan Neumann,¹ Kay E. Gottschalk,¹ R. Dean Astumian^{2*}

¹Chair for applied Physics, Ludwig-Maximilians-University Munich,
Amalienstr. 54, Munich, 80799, Germany

²University of Maine, Orono, Maine, USA

*To whom correspondence should be addressed; E-mail: astumian@maine.edu.

Molecular rotation is important for many biomolecular machines as well as for synthetic brownian molecular motors. Here we describe molecular dynamics studies of a diethylsulfide rotor on a gold (111) surface driven by a high frequency oscillating electric field normal to the surface. This molecular system has been experimentally studied with low temperature scanning/tunneling microscopy (STM) experiments (1). In vacuum, the diethylsulfide molecule can exist in either a trans- configuration, or a higher energy cis-configuration. Here, we show that on a three-fold symmetric gold surface both cis and trans forms are split into two distinct configurations (trans-1 and trans-2, and cis-1 and cis-2) that differ by a phase angle in their rotational free-energy profiles. A high frequency (THz) AC (alternating current) electric field applied normal to the surface drives directed rotation of the trans states of the diethylsulfide rotor, with the two configurations rotating in opposite direction. The maximum directed rotation rate is 10^{10} rotations per second, significantly faster than the rotation of previously reported directional molecular rotors. Understanding the fundamental basis of directed motion of surface rotors is essential for the further development of efficient

externally driven artificial rotors. Our results represent a first step towards the design of a surface-bound molecular rotary motor with a tunable rotation frequency and direction.

Control and direction of motion at the molecular level is one of the great overarching themes of nanoscience (2, 3). Captivated by the mechanisms of biological molecular motors and rotors, synthetic chemists have recently made great progress in the design and synthesis of molecular machines, including motors (4), steppers (5), and rotors (6), many of which function as brownian machines (7) that take advantage of, rather than fight against, ineluctably present thermal noise. Most of these, however, operate only relatively slowly, well below the MHz regime. Recently, Garcia-Garibay and colleagues (8) reported on synthesis and characterization of a halogen bonded crystal with a rotational degree of freedom having a rotation rate in the GHz. The rotation is directionless, with equal probability in the clockwise and counterclockwise directions. A key goal in construction of a functional molecular machine is to design a mechanism for inputting energy to drive rapid directed rotation. Chemical driving (9) suffers from diffusional limitations and seems limited to the 10-100 kHz range, consistent with biomolecular machines driven by, e.g., hydrolysis of ATP. Light (10) offers another possibility (11), but optically driven devices may be limited by the finite number of excitation/de-excitation cycles a molecule can undergo before breaking down. Here we discuss driving directed rotation with externally applied high frequency electric fields.

Inspired by low temperature single-molecule STM experiments on the rotational dynamics of thioether surface rotors (1, 12) we carried out room temperature (300 K) molecular dynamics studies (13, 14) of a diethylsulfide (DES) rotor on a gold (111) surface under the influence of a high frequency (THz) oscillating electric field normal to the gold surface. The AC field can drive directed rotation that depends on the conformational state of the molecule and on the frequency and amplitude of the field. We interpret the mechanism of the field induced directed rotation in terms of the dependence of the energy landscape of the different rotor conformations on the static electric field strength. Cycling through in

itself symmetric energy landscapes allows to create a time dependent asymmetry in the population of the rotor angles. The frequency dependence can be well fit by a response function that is the sum of an out-of-phase component at the characteristic frequency of the rotor and an in-phase component at twice the characteristic frequency of the rotor. The THz field induces GHz rotation of the molecular rotor making it the fastest rotor (by far) described to date.

The motion of a diethylsulfide (DES) rotor on a gold (111) surface was investigated using molecular dynamics (MD) simulations with DFT optimized GolP parameters (15). The sulfur was bound in an fcc position to the gold thus forming a stationary rotation axis (Fig 1A). By analyzing the free rotation of the rotor we identified four major conformations, two trans- and two cis-isomers, by (Fig 1A) that can be classified by two dihedral angles, $\delta_1(C^1 - C^2 - S - C^3)$ and $\delta_2(C^2 - S - C^3 - C^4)$, along the backbone of the DES molecule ($C^1H_3 - C^2H_2 - S - C^3H_2 - C^4H_3$). The two cis-forms, cis-1 ($\delta_1 < 0, \delta_2 > 0$) and cis-2 ($\delta_1 > 0, \delta_2 < 0$), are inter-converted by rotation about an axis normal to the gold surface. The two trans-isomers are trans-1 ($\delta_1 < 0, \delta_2 < 0$) and trans-2 ($\delta_1 > 0, \delta_2 > 0$) cannot be converted into one another by rotation about an axis normal to the gold surface. Simulations of free rotation for several different static field strength ranging from -9 V/nm to +9 V/nm were carried out. The mean lifetimes in the cis and trans states varied significantly with the field as shown in Table I. These data were calculated by analysis of a number of trajectories with a total time of 0.2 ms.

In our initial studies of the rotational motion under the influence of an oscillating field we noticed that sometimes the rotor turned clockwise, sometimes counter-clockwise, and sometimes the rotation was not directed at all. Generally the direction of rotation remained the same during an entire trajectory, although we sometimes observed that the direction of rotation would abruptly change. At first we ascribed this behavior to

a residual inertial effect and the switching of the direction to the effects of noise, but this explanation was ruled out by showing that the net rotation in all cases stopped very quickly when the field was turned off. Eventually we were able to correlate the behavior at a given frequency with the conformational state of the molecule. Because of the length of simulation possible with the oscillating field (5 ns) the conformation was generally, but not always, constant during simulation of a single trajectory. Due to computational constraints it was not practical to simulate a long enough trajectory that the molecule undergoes many conformational transitions during a single run. Thus we decided to investigate the behavior of the different conformational states of the molecule separately where during a single trajectory the dihedral angle of the rotor was restrained to within $\pm\pi/9$ radians to prevent transition to a different conformational state. This allowed us to focus on the almost 1-D motion of the rotor around an axis perpendicular to the gold surface piercing the center of the sulfur atom. The equation of motion for a 1-D surface rotor with noise is $I\ddot{\theta} + \Gamma\dot{\theta} - U'(\theta) = \xi(t)$ (16). In order to determine the energy landscape $U(\theta)$ we obtained the long-time averaged “equilibrium” occupancy of the rotor as a function of the torsional angle for the different rotor conformations by simulating 11.4 ms trajectories with restrained dihedral angles to prevent the switching between different conformations. The energy landscapes for rotation are then given by relation $k_B T \ln \rho(\theta) \propto U(\theta)$. The landscapes for the two trans- configurations are six-fold symmetric, with trans-2 shifted by $\pi/6$ rad relative to the trans-1 configuration (Fig. 1B), and the landscape for the two cis- configurations are three-fold symmetric, with cis-2 shifted by $\pi/3$ degrees relative to cis-1 (Fig. 1C).

The interaction between the rotor and the gold surface is influenced by a static electric field E_z perpendicular to the gold surface. The partial charges of the DES rotor are distributed such that the negative partial charge of the sulfur ($\delta q_- = -0.335e$) is com-

compensated by the two adjacent methylene groups (each $\delta q_+ = +0.1675e$), leaving the outer methyl groups uncharged. Figure 1B illustrates that since the sulfur is in the rotational axis bound to the gold, the main contribution of the static electric field influencing the rotation is due to a force on the methylene groups. A negative electric field pulls the ethylene away from the gold surface reducing the torsional barriers slightly compared to the field free state, while a positive electric field presses the methylene groups closer to the gold surface thus increasing the torsional barriers. Additionally, the field influences the position of the minima and maxima of the energy for the trans-states, with the phase varying by approximately $\pi/60$ radians from -9 V/nm to $+9$ V/nm Figs. 2a and 2b. The amplitude of the energy profile depends on the field for the cis-states but the phase does not shift.

The energy landscape for the trans-states is a simple cosine function $U(\theta, E_z) = A(E_z) \cos[n\theta + \phi(E_z)]$ ($n = 3$ for cis- and $n = 6$ for trans- states) at each value of the field, where the field dependent amplitude is well fit by the relation $A(E_z) = A(0)(1 + aE_z + \dots)$ and we keep only the first correction, with $a = .058$ nm/V and with $A(0) = k_B T$. The phase relative to the zero-field case is given by $\phi(E_z) = bE_z$, with $b = \pm .146$ (nm/V) where we take the minus sign for trans-1 and the plus sign for trans-2. An oscillating electric field normal to the gold surface leads to a time dependent potential in which both the amplitude $A(E_z(t))$ and phase $\phi(E_z(t))$ vary in time through the external field $E_z(t) = E_0 \cos(\omega t)$. In our study the amplitude E_0 ranged from 0.75 to 9 V/nm and the oscillation frequency ω ranged from 1.5 THz to 7.5 THz.

Stimulation of the surface rotor by a time dependent field gives rise to a very rich and complex set of behaviors of the rotor. Neither of the two cis-states undergo directional rotation at any field strength or frequency. The effective rotational diffusion rate, however, does depend significantly on the field parameters. Both trans-1 and trans-2 are driven

to undergo directed rotation in a strongly frequency dependent way. At each frequency the magnitude of the driven rotation is a monotonic function of field amplitude up to about 9 V/nm so in this paper we focus on the largest field amplitude as we consider the frequency response of the system.

The net rotation rate approaches zero in the zero frequency limit. As the frequency is increased to greater than THz the rotor begins to undergo net rotation, first one way, and then the next, passing through zero. The rotation rate falls back to near zero at slightly higher frequencies. Then, as the frequency increases further there is a large peak in the net rotational rate. Significantly, the frequency at which the maximum of the high frequency peak occurs is precisely twice the frequency at which the net rotation goes through zero in switching between clockwise and counterclockwise rotation at the lower frequency feature. We can gain insight into this complex behavior by numerically solving the deterministic equation of motion, which for our sinusoidally oscillating field can be rewritten

$$\ddot{\theta} + \tau^{-1}\dot{\theta} + \omega_0^2 [1 + aE_0 \cos(\omega t)] [\sin(\theta + bE_0 \cos(\omega t))] = 0 \quad (1)$$

There are two relevant characteristic frequencies, the damping frequency $\tau^{-1} = \frac{\Gamma}{I}$, and the characteristic librational frequency of the molecule near the minima of the sinusoidal potential $\omega_0 = 2\pi\sqrt{\frac{A(0)}{I}}/(\pi/3)$. For small molecular rotors the librational frequency is typically of order 10^{13} radians/sec (θ). Using a moment arm $r = 1$ nm, reduced mass of 15 amu, and an amplitude $A_0 = 4 \times 10^{-21}$ J $\approx k_B T$, we calculate $\omega_0 = 2.4$ THz. Judging by the number of overshoots seen in simulations starting with non-zero initial velocity the damping frequency τ^{-1} seems to be a bit less than half the librational frequency.

The numerical solution of the deterministic differential equation (1) already foreshadows many of the features observed in the molecular dynamics simulation of the surface rotor. Most notably, for sufficiently large stimulation and for sufficiently small damp-

ing, when the external frequency approaches twice the characteristic frequency there is a period doubling transition close to $\omega = 2\omega_0$ indicative of parametric resonance. The amplitude of oscillation in the position builds over several periods of the external field, finally reaching a maximum amplitude. The period doubling is similar to the half synchronous rotation described by Horinek and Michl (17) although here the amplitude of oscillation - not the rotation rate of the rotor - has twice the period of the external stimulation. Inertia is essential for the parametrically driven oscillation and there is neither period doubling nor increase in amplitude of the oscillation if the damping is too strong. However, in the absence of driving, inertial effects are damped very quickly, within about 4 overshoot periods ($\approx 10^{-12}$ s $^{-1}$) with the parameter values we used, as shown in the inset of Fig. 2D, consistent with what we observed in the MD simulations. The behavior demonstrated by solving the deterministic equation (1) is not in itself sufficient to explain the observed directed rotation - the AC field acting alone does not provide sufficient energy to overcome the barrier. We propose that the rotation is a noise assisted stochastic pumping process (18) where the asymmetric oscillation in position leads to a greater chance for thermal activation over the barrier in the clockwise direction than in the counterclockwise direction for the trans-1 state. To emphasize the diffusional character of the motion we calculated the probability density near the top of the barrier in both high (positive, Fig. 3A) and low (negative) field. The net currents can be calculated in terms of the simple diffusion at the top of the barrier averaged over a cycle of the field.

Inspired by the Lorentz model for a bound electron in an oscillating field and by the behavior of a parametric oscillator (19), we search for a theoretical description of the observed features of the induced net rotation in the simulations by cobbling together a linear out-of-phase response function at the characteristic frequency, and an in-phase

response function at twice the characteristic frequency,

$$J = J_{\max} \left\{ \frac{\tau^{-1}(\omega - \omega_0)}{1 + [2\tau^{-1}(\omega - \omega_0)]^2} + \frac{1}{1 + [2\tau^{-1}(\omega - 2\omega_0)]^2} \right\} \quad (2)$$

Rather amazingly this theory describes the frequency dependence of the net rotation quite well as shown in Fig. 3C. The response at the characteristic frequency arises from a direct driving of the phase (the equilibrium position in a harmonic approximation, Fig. 2B) while the response at twice the characteristic frequency arises from parametric modulation of the amplitude (the spring constant in a harmonic approximation, Fig. 2B). The essential symmetry breaking occurs because in the trans-1 state the amplitude relative to that at zero-field is large when the phase is negative relative to that at zero field and small when the phase is positive relative to that at zero field, and *vice versa* for trans-2. If either a or b is zero in Eq. (1) the oscillation is perfectly symmetric under all conditions and there can be no directed rotation even though energy is continually fed into the system via the external perturbation.

In the linear driving regime the net rotation is the difference between a large rotation rate in one direction and an even larger rate in the other direction (Fig. 3E). On the other hand, in the parametric driving regime the rotation is almost deterministic, with only very infrequent reverse rotations. At still higher frequency both directed and diffusional rotation essentially vanish.

We have demonstrated by molecular dynamic simulations that THz applied fields can be used to drive directed motion, and to control both net rotation and rotational diffusion, of a diethylsulfide molecule on a gold surface. Near a characteristic frequency (2.8 THz) that can be calculated from molecular parameters the rotor can be switched between clockwise and counterclockwise rotational modes by small changes in the frequency of the applied field. The frequency of the net rotation is relatively small (3 GHz), and the

Peclet number (the magnitude of the difference divided by the sum of the clockwise and counterclockwise rates) is about 0.5. At twice this characteristic frequency (5.6 THz) the rotor is parametrically pumped to undergo directional rotation at a larger rate (10 GHz) and the Peclet number approaches unity since there are essentially no backward rotations. A simple deterministic model Eq. (1) captures qualitatively the observed parametric pumping, but the rotation of the molecule requires thermal noise to provide energy for overcoming the barrier once the large asymmetric oscillation is engendered by the applied field. The frequency response is well described by a simple theory for the response function with an out-of-phase component at the characteristic frequency and an in-phase component at twice the characteristic frequency.

The maximal stimulated net rotation at 10 GHz is very much faster than any other directional rotor with which we are familiar. Although the high frequency seems more likely to have significant technological application, it will be impossible to experimentally access directionality by use of previous mechanisms for sensing directional rotation such as the tunneling current to the surface from an AFM tip. However, the rotating partial charge on the inner methyl groups will cause a magnetic field $\vec{B} = \mu_0 \delta q_+ / (T r)$, where μ_0 is the magnetic permeability, and T is the period of the rotation. For maximal rotation rate of 10 GHz this works out to be greater than 10 mG which should be relatively easily measurable. Conversely, the rotation rate should depend on any magnetic fields, allowing this rotor to act as a molecular compass (20)

The two distinct trans-states, trans-1 and trans-2, rotate in opposite directions at every frequency and amplitude. With an equal mixture of these two forms on a surface there would be no net rotation. Designing some means of switching the relative stability of the two states would provide a very powerful mechanism for switching the net rotational direction. An interesting possibility is to use a magnetic field normal to the gold surface

in combination with a THz field to dynamically favor one state over another, depending on the direction of the magnetic field, even under conditions where the two conformers are *a priori* energetically equivalent. The electric field breaks microscopic reversibility (21), and the magnetic field then breaks “macroscopic reversibility”. A detailed study of the conformational dynamics during stimulation would provide important insight into how to proceed in this direction but such a study will be very computationally intensive.

We have described a molecular dynamics simulation of a very fast surface rotor that can be sensitively driven and controlled by an external THz AC electric field. We anticipate that this work will provide stimulation for experimental as well as for further theoretical work toward the design of controllable rotors that can be used as components in the design of integrated molecular machines

References and Notes

1. A. Baber, H. Tierney, E. Sykes, *ACS nano* **2**, 2385 (2008).
2. W. H. B. C. Stipe, M. A. Rezaei, *Science* **279**, 1907 (1998).
3. J. Gimzewski, *et al.*, *Science* **281**, 531 (1998).
4. E. R. Kay, D. A. Leigh, F. Zerbetto, Synthetic molecular motors and mechanical machines (2007).
5. M. von Delius, D. A. Leigh, *Chem. Soc. Rev.* (2011).
6. G. S. Kottas, L. I. Clarke, D. Horinek, J. Michl, *Chem. Rev.* **105**, 1281 (2005).
7. R. D. Astumian, *Science* **276**, 917 (1997).
8. C. Lemouchi, *et al.*, *J. Am. Chem. Soc.* **133**, 6371 (2011).

9. T. Kelly, H. D. Silva, R. Silva, *Nature* **401**, 150 (1999).
10. N. Koumura, R. Zijlstra, R. Delden, N. Harada, B. Feringa, *Nature* **401**, 152 (1999).
11. V. Balzani, A. Credi, M. Venturi, *Chem. Soc. Rev.* **38**, 1542 (2009).
12. H. Tierney, A. Baber, E. Sykes, *J. Phys. Chem. C* **113**, 10913 (2009).
13. J. Vacek, J. Michl, *Adv. Funct. Mat.* **115**, 730 (2007).
14. A. Akimov, A. Kolomeisky, *J. Phys. Chem. C* **115**, 125 (2011).
15. F. Iori, R. D. Felice, E. Molinari, S. Corni, *J. Comput. Chem.* **30**, 1465 (2009).
16. J. Gimzewski, *et al.*, *Science* **281**, 531 (1998).
17. D. Horinek, J. Michl, *Proc. Natl. Acad. Sci. U S A* **102**, 14175 (2005).
18. R. D. Astumian, *Ann. Revs. Biophys.* **40**, 289 (2011).
19. J. Tan, G. Gabrielse, *Physical Review A* **48**, 3105 (1993).
20. Z. Dominguez, *et al.*, *Journal of the American Chemical Society* **125**, 8827 (2003).
PMID: 12862478.
21. D. Blackmond, *Angew. Chem. Int. Ed.* **48**, 2648 (2009).
22. B. Hess, C. Kutzner, D. van der Spoel, E. Lindahl, *J. Chem. Theory Comput.* **4**, 435 (2008).
23. F. Iori, S. Corni, *J. Comput. Chem.* **29**, 1656 (2008).
24. W. Jorgensen, D. Maxwell, J. Tirado-Rives, *J. Am. Chem. Soc.* **118**, 11225 (1996).
25. M. Tachibana, K. Yoshizawa, A. Ogawa, *J. Phys. Chem. B* **106**, 12727 (2002).

26. P. P. Ewald, *Annalen der Physik* **369**, 253 (1921).

27. G. Bussi, D. Donadio, M. Parrinello, *J. Chem. Phys.* **126**, 1 (2007).

Acknowledgements

28. We thank the German Humboldt Foundation for conferral of a Humboldt Prize to RDA and the Elitenetzwerk Bayern for financial support.

Table 1: Lifetimes vs. Field

Field	τ_{cis}	τ_{trans}
-9 V/nm	1.2 ps	7.52 ps
-6 V/nm	1.97 ps	11.45 ps
-3 V/nm	3.48 ps	20.38 ps
0 V/nm	7.7 ps	51 ps
+3 V/nm	15.81 ps	94.27 ps
+6 V/nm	51.79 ps	262.60 ps
+9 V/nm	295.45 ps	850.06 ps

Figure 1

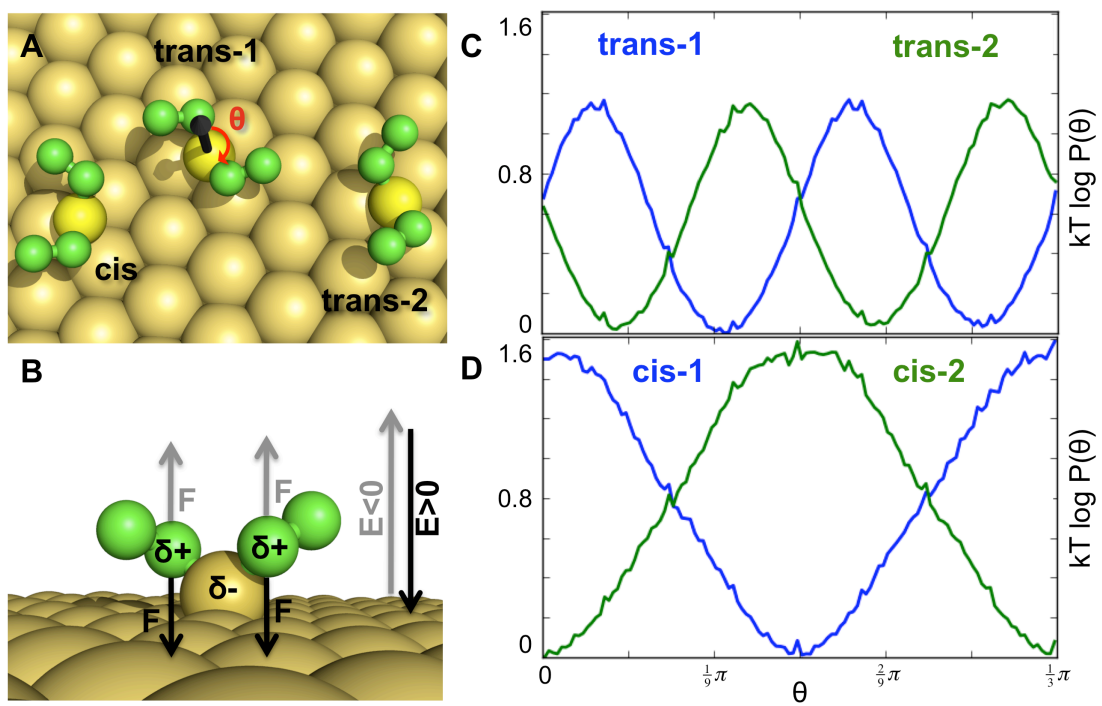


Figure 2

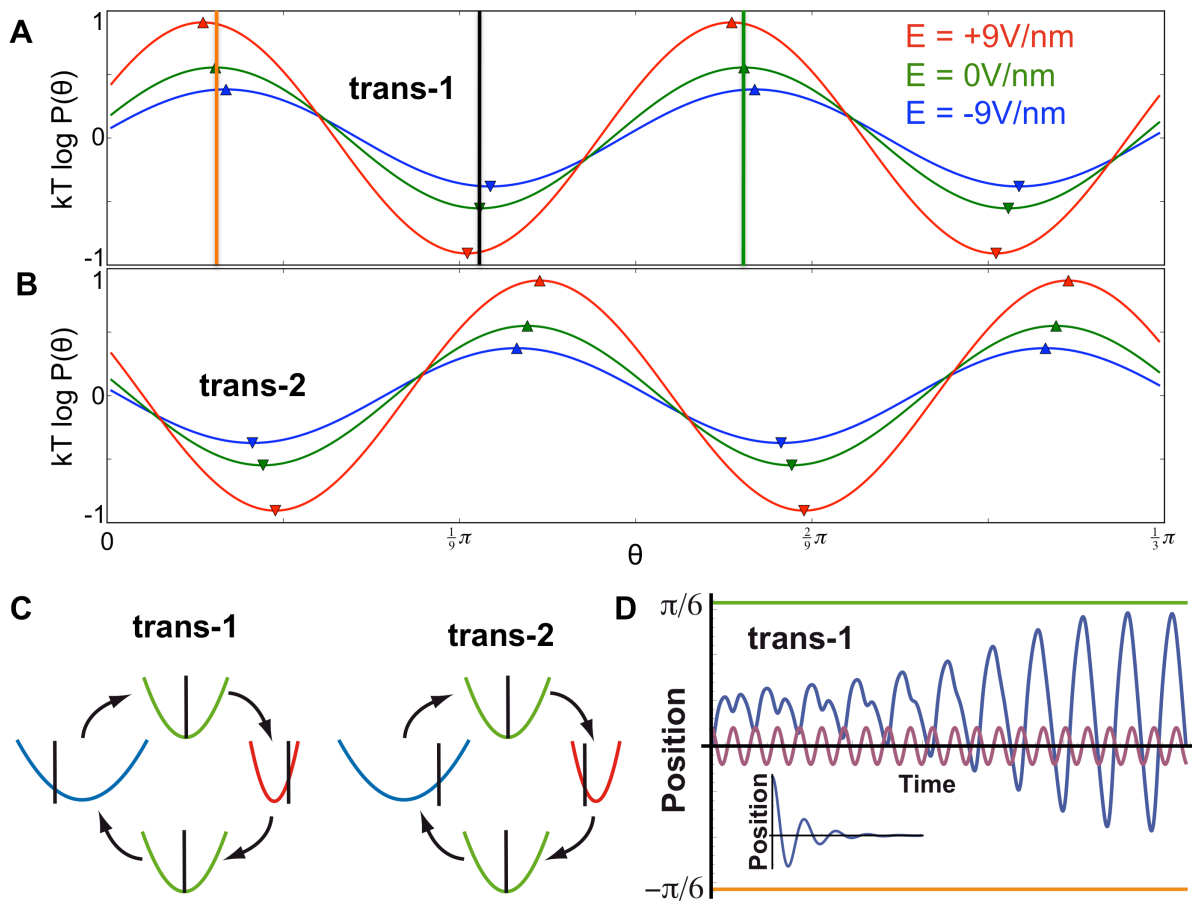


Figure 3

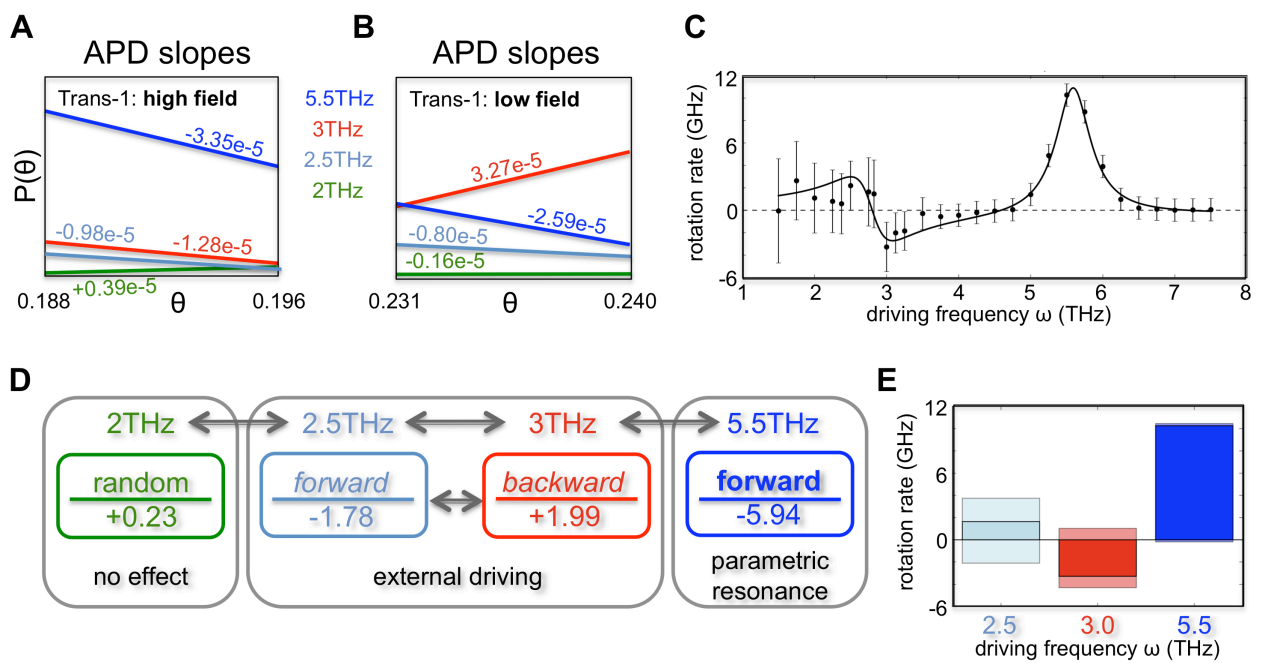


Fig. 1. (A) conformations (cis, trans-1 and trans-2) of the diethylsulfid rotor bound in an fcc position to the gold (111) surface. The angle θ (red) around the rotation axis (black) is explicitly illustrated for the trans-1 conformation. (B) An electric field acts on the partial charges of the rotor to force the rotor arms slightly away from or toward the surface. (C) Plot of the logarithm of the probability density, and hence of the free energy landscape, of the freely rotating trans-1 (blue) and trans-2 (green) conformations. (D) Plot of the logarithm of the probability density of freely rotating cis-1 (blue) and cis-2 (green) conformations.

Fig. 2. Free energy landscapes at $E=+9V/nm$ (red), at $E= 0 V/nm$ (green) and at $E=-9V/nm$ (blue) for trans-1 (A) and trans-2 (B) are shown. The electric field shifts the phase (i.e., the positions of minima and maxima) and modifies the amplitude. The orange, black and green line correspond to the $-\pi/6$, 0 and $\pi/6$ positions and are reflected in (D). (C) Schematic illustration of the motion of an energy minimum in the harmonic approximation. For trans-1 the minimum shifts to the left when the spring constant is large and to the right when the spring constant is small. For trans-2 the minimum shifts to the right when the spring constant is large and to the left when the spring constant is small. (D) Deterministic simulation of eq. (1). External driving field (violet) and angle position of the rotor (blue) are shown. The inset shows the damped relaxation of the rotor position when the field is turned off.

Fig. 3. (A & B) The angle probability distributions (APD) of the rotor at different frequency oscillating electric fields (2THz:green, 2.5THz light blue, 3THz:red, 5.5THz:blue) at the position of the barrier maximum for $E=+9V/nm$ at $\theta = 13.5^\circ \pm 0.25^\circ$ (A) and for $E = -9V/nm$ at $\theta = 11.0^\circ \pm 0.25^\circ$ (B). The colored numbers on the lines are the calculated gradients of the APDs. (C) Each point represents the average response of the rotor in trans-1 conformation over multiple trajectories including the error. The rotor

dependence on the driving frequency can be described with eq. (2) (solid curve). **(D)** Scheme correlating the driving frequency to the resulting direction of rotation and the sum of slopes at high and low fields for conformation trans-1. **(E)** Bar graph illustrating clockwise (positive) and counterclockwise (negative) rotations (pastel colors) and net rotations (vivid colors).

Supplemental: Materials and Methods

General

All simulations of the DiEthylSulfid (DES) rotor on a gold (111) surface are performed with the MD simulation software GROMACS (Vers. 4.0.x) (22). The GolP force field is used (23). It is optimized for gold (111)surface simulations and based on the OPLS-AA force field (24). The diethylsulfid parameters have been DFT optimized for this GolP force field by the group of Stephano Corni (15). The system is simulated in vaccum with periodic boundary conditions.

The gold is 5 atom layers thick with a surface area of $3.23 \times 3.56nm^2$. The DES is positioned on the surface with the sulfur in an fcc position on the gold $0.258nm$ away from each of its three neighboring gold atoms (25). The position of the sulfur is frozen in space to simulate the sulfur gold bond and to form a stable axis for the stationary rotation on the gold. The gold surface and the DES are both neutrally charged. The partial charge distribution of the DES on the gold can be found in Table 2.

Table 2: The outer two methyl groups are neutrally charged, while the inner two methylen groups are positively charged, each with half the opposite charge of the central sulfur atom. Every hydrogen atom holds the same partial charged of $+0.06e$.

Group	CH_3	CH_2	S	each H
Charge [e]	0	+0.1675	-0.335	+0.06

System Preparation

An energy minimization of the system is simulated using steepest descent with a maximum step size of $0.01nm$. A cut-off radius of $1.1nm$ is used for Coulomb interactions and $1.0nm$ for van-der-Waals interactions. This energy minimized structure is used as starting

structure for field free simulations.

All simulations are done at 300K. For all further simulations electrostatics are calculated with Fast Particle-Mesh Ewald electrostatics (PME) (26) with an order of four and a cutoff for coulomb and van-der-Waals interactions of 1.0nm. Temperature coupling is done by a velocity rescaling thermostat (27) coupled to the whole system.

Angle Definition

The rotation angle α is calculated using the vector \mathbf{v} connecting the two inner C_α atoms by $\alpha = \arctan(\frac{v_x}{v_y}) - \text{sign}(v_y) * 90^\circ + n_{cyc} \times 360^\circ$ with n_{cyc} being the number of full rotations.

Relative Energies

The free energies are calculated from the population of the angles α by $\delta E(\alpha) = -k_B T \times \ln(\frac{N(\alpha)}{N_{\min}}) - \min(E(\alpha))$, with the rotation angle α (from 0° to 120°), the number of timesteps $N(\alpha)$ in which the angle is populated and the minimum population count of all angles N_{\min} .

Initial Structures for free rotation

For further simulations including an electric field, a set of 10 structures have been chosen from the final structures of the free rotation simulations with 200ns simulation each, altogether representing a sample of different rotation angles α to increase sampling especially at high fields. A new starting velocity distribution is generated for each new simulation.

Initial Structures for restrained simulations

For the restrained simulations, the structures of a 200ns long undisturbed rotation trajectory are clustered. The six prominent clusters (every 60°) of each trans conformation

are chosen as initial structures. In addition two prominent clusters for each cis state are simulated.

Restrained simulations

The dihedral angle restraints allows a free development of the system in a range of $\pm 20^\circ$ around the energy minimum of the dihedral angle distributions. Thus, the rotor could freely explore its energy landscape in the restraint conformation preventing switching to unwanted conformations.

External Electric Field

An external electric field is applied perpendicular to the gold surface in z-direction. The electrical field is positive if it points from the rotor to the surface (Fig. 1B). The electric field strength ranges from -9 to +9 V/nm. The simulation time is 2ns per trajectory. In the highest field regimes the partial charge distribution of the molecular rotor might be subject to additional polarization effects, not taken into account by the DFT derived partial charge distribution.

External Oscillating Electric Field

We apply an oscillating field

$$E(t) = E_0 \times \cos(\omega t) \times \hat{e}_z$$

perpendicular to the gold surface with \hat{e}_z pointing from the rotor to the gold surface. The strength of the oscillating field E_0 ranges from 0.75 to $9 \frac{V}{nm}$, while the oscillation frequency of the electric field ω ranges from 1.5 to 7.5 THz. Lower oscillation frequencies interpolated the behavior of the rotor between zero field and 1.5 THz driving, showing

no additional features. Higher frequencies strongly arrest the rotor on the surface and no further rotation is observed.

References

1. Christof B Mast and Dieter Braun. Thermal trap for dna replication. *Physical Review Letters*, 104(18):188102, May 2010.
2. G Hammes. Multiple conformational changes in enzyme catalysis. *Biochemistry*, 41(26):8221–8228, Jan 2002.
3. Anthony Mittermaier and Lewis E Kay. New tools provide new insights in nmr studies of protein dynamics. *Science*, 312, Jan 2006.
4. R Bruschweiler. New approaches to the dynamic interpretation and prediction of nmr relaxation data from proteins. *Current Opinion In Structural Biology*, 13:175–183, Jan 2003.
5. Elan Z Eisenmesser, Oscar Millet, Wladimir Labeikovsky, Dmitry M Korzhnev, Magnus Wolf-Watz, Daryl A Bosco, Jack J Skalicky, Lewis E Kay, and Dorothee Kern. Intrinsic dynamics of an enzyme underlies catalysis. *Nature*, 438:117–121, Jan 2005.
6. Kevin D G Pflieger and Karin A Eidne. Illuminating insights into protein-protein interactions using bioluminescence resonance energy transfer (bret). *Nature Methods*, 3(3):165–174, Jan 2006.
7. Katherine Henzler-Wildman and Dorothee Kern. Dynamic personalities of proteins. *Nature*, 450:964–972, Jan 2007.
8. Ben N Giepmans, Stephen R Adams, Mark H Ellisman, and Roger Y Tsien. The fluorescent toolbox for assessing protein location and function. *Science*, 312:217–224, Jan 2006.
9. Benjamin Schuler and William A Eaton. Protein folding studied by single-molecule fret. *Current Opinion In Structural Biology*, 18:16–26, Jan 2008.
10. F Oesterhelt, D Oesterhelt, M Pfeiffer, A Engel, Hermann E Gaub, and D J Müller. Unfolding pathways of individual bacteriorhodopsins. *Science*, 288(5463):143–146, Apr 2000.
11. Max Kessler, Kay E Gottschalk, Harald Janovjak, Daniel J Mueller, and Hermann E Gaub. Bacteriorhodopsin folds into the membrane against an external force. *Journal Of Molecular Biology*, 357:644–654, Jan 2006.
12. M S Kellermayer, S B Smith, H L Granzier, and C Bustamante. Folding-unfolding transitions in single titin molecules characterized with laser tweezers. *Science*, 276(5315):1112–6, May 1997.
13. Jan Philipp Junker, Fabian Ziegler, and Matthias Rief. Ligand-dependent equilibrium fluctuations of single calmodulin molecules. *Science*, 323(5914):633–637, Jan 2009.

14. J Hsin, M Sotomayor, G Comellas, and K Schulten. Discovery through the computational microscope. *Structure*, 17:1295–1306, Jan 2009.
15. G Moore. Cramming more components onto integrated circuits. *Electronics*, 38(8), Jan 1965.
16. G Moore. Lithography and the future of moore’s law. *Proceedings of SPIE*, 2437:1–8, Jan 1995.
17. Vincent A Voelz, Gregory R Bowman, Kyle Beauchamp, and Vijay S Pande. Molecular simulation of ab initio protein folding for a millisecond folder nt19(1-39). *Journal Of The American Chemical Society*, 132(5):1526–8, Feb 2010.
18. Peter L Freddolino, Anton S Arkhipov, Steven B Larson, Alexander McPherson, and Klaus Schulten. Molecular dynamics simulations of the complete satellite tobacco mosaic virus. *Structure*, 14(3):437–49, Mar 2006.
19. Mareike Zink and Helmut Grubmueller. Mechanical properties of the icosahedral shell of southern bean mosaic virus: A molecular dynamics study. *Biophysical Journal*, 96(4):1350–1363, Jan 2009.
20. K Y Sanbonmatsu and C-S Tung. High performance computing in biology: multimillion atom simulations of nanoscale systems. *Journal of Structural Biology*, 157(3):470–80, Mar 2007.
21. Elizabeth Villa, Jayati Sengupta, Leonardo G Trabuco, Jamie LeBarron, William T Baxter, Tanvir R Shaikh, Robert A Grassucci, Poul Nissen, Mans Ehrenberg, Klaus Schulten, and Joachim Frank. Ribosome-induced changes in elongation factor tu conformation control gtp hydrolysis. *Proc Natl Acad Sci U S A*, 106(4):1063–1068, Jan 2009.
22. Yuji Sugita and Yuko Okamoto. Replica-exchange molecular dynamics method for protein folding. *Chemical physics letters*, 314, Jan 1999.
23. Nina Singhal, C Snow, and V Pande. Using path sampling to build better markovian state models: Predicting the folding rate and mechanism of a tryptophan zipper beta hairpin. *The Journal of Chemical Physics*, 121(1):415–425, Jan 2004.
24. H Grubmüller. Predicting slow structural transitions in macromolecular systems: Conformational flooding. *Physical Review E*, 52(3):2893–2906, Jan 1995.
25. M Ceriotti and M Parrinello. A self-learning algorithm for biased molecular dynamics. *Proc Natl Acad Sci U S A*, 107(41):17509–17514, Jan 2010.
26. H Lu and K Schulten. The key event in force-induced unfolding of titin’s immunoglobulin domains. *Biophysical Journal*, 79(1):51–65, Jul 2000.

-
27. Julia Morfill, Jan Neumann, Kerstin Blank, Uta Steinbach, Elias M Puchner, Kay-Eberhard Gottschalk, and Hermann E Gaub. Force-based analysis of multidimensional energy landscapes: Application of dynamic force spectroscopy and steered molecular dynamics simulations to an antibody fragment-peptide complex. *J Mol Biol*, 381:1253–1266, Jun 2008.
 28. VP Hytonen and Viola Vogel. How force might activate talin’s vinculin binding sites: Smd reveals a structural mechanism. *PLoS Comput Biol*, 2(4):e24, Jan 2008.
 29. Armando del Rio, Raul Perez-Jimenez, Ruchuan Liu, Pere Roca-Cusachs, Julio M Fernandez, and Michael P Sheetz. Stretching single talin rod molecules activates vinculin binding. *Science*, 323(5914):638–41, Jan 2009.
 30. Mariano Carrion-Vazquez, Hongbin Li, Hui Lu, Piotr E Marszalek, Andres F Oberhauser, and Julio M Fernandez. The mechanical stability of ubiquitin is linkage dependent. *Nature Structural Biology*, 10(9):738–43, Sep 2003.
 31. Daniel K West, David J Brockwell, Peter D Olmsted, Sheena E Radford, and Emanuele Paci. Mechanical resistance of proteins explained using simple molecular models. *Biophysical Journal*, 90(1):287–97, Jan 2006.
 32. Robert B Best, Emanuele Paci, Gerhard Hummer, and Olga K Dudko. Pulling direction as a reaction coordinate for the mechanical unfolding of single molecules. *The journal of physical chemistry B*, 112(19):5968–76, May 2008.
 33. Hendrik Dietz and Matthias Rief. Exploring the energy landscape of gfp by single-molecule mechanical experiments. *Proc Natl Acad Sci U S A*, 101(46):16192–16197, Nov 2004.
 34. Hendrik Dietz, Felix Berkemeier, Morten Bertz, and Matthias Rief. Anisotropic deformation response of single protein molecules. *Proc Natl Acad Sci U S A*, 103(34):12724–12728, Aug 2006.
 35. H Dietz and M Rief. Elastic bond network model for protein unfolding mechanics. *Physical Review Letters*, 100(7):098101, Jan 2008.
 36. M Rief, M Gautel, A Schemmel, and H E Gaub. The mechanical stability of immunoglobulin and fibronectin iii domains in the muscle protein titin measured by atomic force microscopy. *Biophysical Journal*, 75(6):3008–14, Dec 1998.
 37. M Rief, M Gautel, F Oesterhelt, J M Fernandez, and Hermann E Gaub. Reversible unfolding of individual titin immunoglobulin domains by afm. *Science*, 276(5315):1109–1112, May 1997.

38. E Puchner, G Franzen, M Gautel, and H Gaub. Comparing proteins by their unfolding pattern. *Biophysical Journal*, 95:426–434, Jan 2008.
39. Ronen Alon and Michael L Dustin. Force as a facilitator of integrin conformational changes during leukocyte arrest on blood vessels and antigen-presenting cells. *Immunity*, 26(1):17–27, Jan 2007.
40. Benjamin Geiger, Joachim P Spatz, and Alexander D Bershadsky. Environmental sensing through focal adhesions. *Nat Rev Mol Cell Biol*, 10(1):21–33, Jan 2009.
41. E Puklin-Faucher and M Sheetz. The mechanical integrin cycle. *Journal of cell science*, 122:179–186, Jan 2009.
42. R Hynes. Integrins:: Bidirectional, allosteric signaling machines. *Cell*, 110:673–687, Jan 2002.
43. O Vinogradova, A Velyvis, A Velyviene, B Hu, TA Haas, EF Plow, and J Qin. A structural mechanism of integrin alpha(iib)beta(3) "inside-out" activation as regulated by its cytoplasmic face. *Cell*, 110(5):587–597, Jan 2002.
44. S Shattil, C Kim, and M Ginsberg. The final steps of integrin activation: the end game. *Nat Rev Mol Cell Biol*, 11:288–300, Jan 2010.
45. Nicholas J Anthis and Iain D Campbell. The tail of integrin activation. *Trends in Biochemical Sciences*, 36(4):191–198, Jan 2011.
46. Catherine G Galbraith, Kenneth M Yamada, and Michael P Sheetz. The relationship between force and focal complex development. *The Journal of cell biology*, 159(4):695–705, Nov 2002.
47. Pakorn Kanchanawong, Gleb Shtengel, Ana M Pasapera, Ericka B Ramko, Michael W Davidson, Harald F Hess, and Clare M Waterman. Nanoscale architecture of integrin-based cell adhesions. *Nature*, 468(7323):580–4, Nov 2010.
48. David A Calderwood. Talin controls integrin activation. *Biochem Soc Trans*, 32(Pt3):434–437, Jun 2004.
49. Vesa P Hytönen and Viola Vogel. How force might activate talin's vinculin binding sites: Smd reveals a structural mechanism. *PLoS Comput Biol*, 4(2):e24, Feb 2008.
50. Tong-Lay Lau, Chungho Kim, Mark H Ginsberg, and Tobias S Ulmer. The structure of the integrin alpha*iib*beta3 transmembrane complex explains integrin transmembrane signalling. *EMBO J*, 28(9):1351–61, May 2009.

-
51. Nicholas J Anthis, Kate L Wegener, Feng Ye, Chungho Kim, Benjamin T Goult, Edward D Lowe, Ioannis Vakonakis, Neil Bate, David R Critchley, Mark H Ginsberg, and Iain D Campbell. The structure of an integrin/talin complex reveals the basis of inside-out signal transduction. *EMBO J*, 28(22):3623–32, Nov 2009.
 52. Paul R Elliott, Benjamin T Goult, Petra M Kopp, Neil Bate, J Günter Grossmann, Gordon C K Roberts, David R Critchley, and Igor L Barsukov. The structure of the talin head reveals a novel extended conformation of the ferm domain. *Structure*, 18(10):1289–99, Oct 2010.
 53. S Furuike, M Hossain, Y Maki, K Adachi, and T Suzuki. Axle-less f1-atpase rotates in the correct direction. *Science*, 319:955–958, Jan 2008.
 54. Siebe B van Albada, Sorin Tanase-Nicola, and Pieter Rein ten Wolde. The switching dynamics of the bacterial flagellar motor. *Mol Syst Biol*, 5:316, Jan 2009.
 55. R Dean Astumian. Design principles for brownian molecular machines: how to swim in molasses and walk in a hurricane. *Physical chemistry chemical physics : PCCP*, 9(37):5067–83, Oct 2007.
 56. E Purcell. Life at low reynolds number. *Am. J. Phys*, 45(1):3–11, Jan 1977.
 57. A Baber, H Tierney, and E Sykes. A quantitative single-molecule study of thioether molecular rotors. *ACS nano*, Jan 2008.
 58. M P Allen and D J Tildeseley. Computer simulation of liquids. *Clarendon Press, Oxford*, Jan 1989.
 59. Daan Frenkel and Berend Smit. Understanding molecular simulation: from algorithms to applications. *Academic Press, London*, Jan 2002.
 60. R Oppenheimer. Zur quantentheorie der molekeln. *Annalen der Physik*, 84(4):458–484, Jan 1927.
 61. P Ehrenfest. Bemerkung über die angenäherte gültigkeit der klassischen mechanik innerhalb der quantenmechanik. *Zeitschrift für Physik A Hadrons and Nuclei*, pages 455–457, Jan 1927.
 62. RW Hockney, SP Goel, and JW Eastwood. Quiet high-resolution computer models of a plasma. *Journal of Computational Physics*, 14(2):148–158, Jan 1974.
 63. B Hess, H Bekker, HJC Berendsen, and JGEM Fraaije. Lincs: A linear constraint solver for molecular simulations. *Journal Of Computational Chemistry*, 18(12):1463–1472, Jan 1997.

64. William L Jorgensen and Julian Tirado-Rives. Potential energy functions for atomic-level simulations of water and organic and biomolecular systems. *Proc Natl Acad Sci U S A*, 102(19):6665–70, May 2005.
65. W Jorgensen, D Maxwell, and J Tirado-Rives. Development and testing of the opls all-atom force field on conformational energetics and properties of organic liquids. *J. Am. Chem. Soc.*, 118:11225–36, Jan 1996.
66. F Iori, R Di Felice, E Molinari, and S Corni. Golph: an atomistic force-field to describe the interaction of proteins with au(111) surfaces in water. *Journal of Computational Chemistry*, 30(9):1465–76, Jul 2009.
67. H Berendsen, D Van der Spoel, and R van Drunen. Gromacs: a message-passing parallel molecular dynamics implementation. *Computer Physics Communications*, 91:43–56, Jan 1995.
68. E Lindahl, B Hess, and D Van der Spoel. Gromacs 3.0: a package for molecular simulation and trajectory analysis. *J Mol Model*, 7(8):306–317, Jan 2001.
69. D Van der Spoel, E Lindahl, B Hess, G Groenhof, AE Mark, and HJC Berendsen. Gromacs: Fast, flexible, and free. *Journal Of Computational Chemistry*, 26(16):1701–1718, Jan 2005.
70. Berk Hess, Carsten Kutzner, David van der Spoel, and Erik Lindahl. Gromacs 4: Algorithms for highly efficient, load-balanced, and scalable molecular simulation. *Journal of Chemical Theory and Computation*, 4(3):435–447, Jan 2008.
71. David Van Der Spoel, Erik Lindahl, Berk Hess, Carsten Kutzner, Aldert R van Buuren, Emile Apol, Pieter J Meulenhoff, D Peter Tieleman, Alfons L T M Sijbers, K Anston Feenstra, Rudi van Drunen, and Herman J C Berendsen. Gromacs user manual version 4.0. *www.gromacs.org*, Jan 2005.
72. M Saito. Molecular dynamics simulations of proteins in solution: Artifacts caused by the cutoff approximation. *The Journal of Chemical Physics*, 101(5):4055–4061, Jan 1994.
73. P P Ewald. Die berechnung optischer und elektrostatischer gitterpotentiale. *Annalen der Physik*, 369(3):253–287, Jan 1921.
74. U Essmann, L Perera, M Berkowitz, Tom Darden, Hsing Lee, and Lee G Pedersen. A smooth particle mesh ewald method. *J. Chem. Phys.*, 103(19):8577–93, Jan 1995.
75. HJC Berendsen, JPM Postma, W F van Gunsteren, A Dinola, and JR Haak. Molecular-dynamics with coupling to an external bath. *Journal of Chemical Physics*, 81(8):3684–3690, Jan 1984.

-
76. T Morishita. Fluctuation formulas in molecular-dynamics simulations with the weak coupling heat bath. *J. Phys. Chem.*, 113(8):2976–82, Jan 2000.
77. Giovanni Bussi, Davide Donadio, and Michele Parrinello. Canonical sampling through velocity rescaling. *The Journal of Chemical Physics*, 126(1):014101, Jan 2007.
78. Wikipedia-User:LadyofHats. http://en.wikipedia.org/wiki/file:main_protein_structure_levels_en.svg.
79. Bruce Alberts, Alexander Johnson, Julian Lewis, Martin Raff, Keith Roberts, and Peter Walter. Molecular biology of the cell. *Taylor & Francis Inc (United States)*, Jan 2002.
80. T Pogorelov and Z Luthey-Schulten. Ab initio protein structure prediction. *Current Opinion In Structural Biology*, 12:176–181, Jan 2002.
81. Carlos Simmerling, Bentley Strockbine, and Adrian E Roitberg. All-atom structure prediction and folding simulations of a stable protein. *Journal Of The American Chemical Society*, 124:11258–9, Jan 2002.
82. C Snow, M Shirts, and V Pande. Simulation of folding of a small alpha-helical protein in atomistic detail using worldwide-distributed computing. *Journal Of Molecular Biology*, 323:927–937, Jan 2002.
83. Philip Bradley, Kira M S Misura, and David Baker. Toward high-resolution de novo structure prediction for small proteins. *Science*, 309:1868–71, Jan 2005.
84. O Schueler-Furman, C Wang, P Bradley, Kira M S Misura, and David Baker. Progress in modeling of protein structures and interactions. *Science*, 310:638–642, Jan 2005.
85. Peter L Freddolino, Feng Liu, Martin Gruebele, and Klaus Schulten. Ten-microsecond molecular dynamics simulation of a fast-folding ww domain. *Biophysical Journal*, 94(10):L75–L77, Jan 2008.
86. J Kendrew, G Bodo, H Dintzis, R G Parrish, and H Wyckoff. A three-dimensional model of the myoglobin molecule obtained by x-ray analysis. *Nature*, 181:662–666, Jan 1958.
87. C B Anfinsen. Principles that govern the folding of protein chains. *Science*, 181(96):223–30, Jul 1973.
88. Ken A Dill, S Banu Ozkan, M Scott Shell, and Thomas R Weikl. The protein folding problem. *Annual review of biophysics*, 37:289–316, Jan 2008.

89. KA Dill and HS Chan. From levinthal to pathways to funnels. *Nature Structural Biology*, 4(1):10–19, Jan 1997.
90. R Zwanzig, A Szabo, and Biman Bagchi. Levinthal’s paradox. *Proceedings of the National Academy of Sciences*, 89(1):20–22, Jan 1992.
91. J Onuchic, N Socci, and P Wolynes. Funnels, pathways, and the energy landscape of protein folding: A synthesis. *Proteins-Structure, Function, and Genetics*, 21:167–195, Jan 1995.
92. José Nelson Onuchic and Peter G Wolynes. Theory of protein folding. *Current Opinion In Structural Biology*, 14:70–75, Jan 2004.
93. H Frauenfelder, SG Sligar, and P Wolynes. The energy landscapes and motions of proteins. *Science*, 254:1598–1603, Jan 1991.
94. M Karplus and J Kuriyan. Molecular dynamics and protein function. *Proc Natl Acad Sci U S A*, 102(19):6679–85, Jan 2005.
95. Kay E. Gottschalk. Impact of the strength and affinity of the integrin-talin interaction on the force-persistence of cell adhesion. *DFG Antrag*, 2008.
96. S Arrhenius. Uber die reaktionsgeschwindigkeit bei der inversion von rohrzucker durch sauren. *Zeitschrift für physikalische Chemie*, 4:226–248, Jan 1889.
97. M van’t Hoff. Etudes de dynamique chimique. *Recueil des Travaux Chimiques des Pays- . . .*, Jan 1884.
98. George I Bell. Models for the specific adhesion of cells to cells. *Science*, 200:618–627, Jan 1978.
99. Evan Evans and Ken Ritchie. Dynamic strength of molecular adhesion bonds. *Biophysical Journal*, 72:1541–1555, Jan 1997.
100. E Evans. Probing the relation between force-lifetime-and chemistry in single molecular bonds. *Annual Review of Biophysics and Biomolecular Structure*, 30:105–128, Jan 2001.
101. C Friedsam, A Wehle, Ferdinand Kühner, and Hermann E Gaub. Dynamic single-molecule force spectroscopy: bond rupture analysis with variable spacer length. *Journal of Physics: Condensed Matter*, 15:1709–23, Jan 2003.
102. William J Greenleaf, Michael T Woodside, and Steven M Block. High-resolution, single-molecule measurements of biomolecular motion. *Annu Rev Biophys Biomol Struct*, 36:171–90, Jan 2007.

-
103. A Ashkin. Optical trapping and manipulation of neutral particles using lasers. *Proc Natl Acad Sci U S A*, 94(10):4853–60, May 1997.
 104. R Merkel, P Nassoy, A Leung, K Ritchie, and E Evans. Energy landscapes of receptor-ligand bonds explored with dynamic force spectroscopy. *Nature*, 397(6714):50–3, Jan 1999.
 105. Steven B Smith, Laura Finzi, and Carlos Bustamante. Direct mechanical measurements of the elasticity of single dna molecules by using magnetic beads. *Science*, 258:1122–26, Jan 1992.
 106. C Albrecht, K Blank, M Lalic-Multhaler, S Hirler, T Mai, I Gilbert, S Schiffmann, T Bayer, H Clausen-Schaumann, and Hermann E Gaub. Dna: a programmable force sensor. *Science*, 301:367–370, Jan 2003.
 107. Ernst-Ludwig Florin, Vincent T Moy, and Hermann E Gaub. Adhesion forces between individual ligand-receptor pairs. *Science*, 264:415–417, Jan 1994.
 108. Matthias Rief, Filipp Oesterhelt, Berthold Heymann, and HE Gaub. Single molecule force spectroscopy on polysaccharides by atomic force microscopy. *Science*, 275(5304):1295–1297, Jan 1997.
 109. Michel Grandbois, Martin Beyer, Matthias Rief, Hauke ClausenSchaumann, and Hermann E Gaub. How strong is a covalent bond? *Science*, 283, Jan 1999.
 110. David Halliday, J Richard Christman, Robert Resnick, and Jearl Walker. Fundamentals of physics, 6th edition. *John Wiley and Sons, Inc*, Jan 2001.
 111. Gregg S Kottas, Laura I Clarke, Dominik Horinek, and Josef Michl. Artificial molecular rotors. *Chemical Reviews*, 105(4):1281–376, Apr 2005.
 112. D Horinek and J Michl. Molecular dynamics simulation of an electric field driven dipolar molecular rotor attached to a quartz glass surface. *J. Am. Chem. Soc*, Jan 2003.
 113. R Landauer and J A Swanson. Frequency factors in the thermally activated process. *Physical Review*, 121(6):1668–74, Jan 1961.
 114. Julia Morfill, Kerstin Blank, Christian Zahnd, Beatrice Luginbühl, Ferdinand Kühner, Kay-E Gottschalk, Andreas Plückthun, and Hermann E Gaub. Affinity-matured recombinant antibody fragments analyzed by single-molecule force spectroscopy. *Biophysical Journal*, 93(10):3583–90, Nov 2007.

115. Christian Zahnd, Silvia Spinelli, Béatrice Luginbühl, Patrick Amstutz, Christian Cambillau, and Andreas Plückthun. Directed in vitro evolution and crystallographic analysis of a peptide-binding single chain antibody fragment (scfv) with low picomolar affinity. *J Biol Chem*, 279(18):18870–7, Apr 2004.
116. R Hartley. Barnase and barstar: two small proteins to fold and fit together. *Trends in Biochemical Sciences*, 14, Jan 1989.
117. A M Buckle, G Schreiber, and A R Fersht. Protein-protein recognition: crystal structural analysis of a barnase-barstar complex at 2.0-Å resolution. *Biochemistry*, 33(30):8878–8889, Aug 1994. X ray structure with 2Å resolution.
118. R Hartley. Directed mutagenesis and barnase-barstar recognition. *Biochemistry*, 32, Jan 1993.
119. Gideon Schreiber and Alan R Fersht. Rapid, electrostatically assisted association of proteins. *Nature Structural & Molecular Biology*, 3(5):427–431, Jan 1996.
120. M Vijayakumar, K Y Wong, G Schreiber, A R Fersht, A Szabo, and H X Zhou. Electrostatic enhancement of diffusion-controlled protein-protein association: comparison of theory and experiment on barnase and barstar. *J Mol Biol*, 278(5):1015–1024, May 1998.
121. Feng Dong, M Vijayakumar, and Huan-Xiang Zhou. Comparison of calculation and experiment implicates significant electrostatic contributions to the binding stability of barnase and barstar. *Biophysical Journal*, 85(1):49–60, Jan 2003.
122. C J Camacho, Z Weng, S Vajda, and C DeLisi. Free energy landscapes of encounter complexes in protein-protein association. *Biophys J*, 76(3):1166–1178, Mar 1999.
123. Alexander Spaar, Christian Dammer, Razif R Gabdouliline, Rebecca C Wade, and Volkhard Helms. Diffusional encounter of barnase and barstar. *Biophysical Journal*, 90(6):1913–1924, Mar 2006.
124. BG Feagan, GR Greenberg, G Wild, RN Fedorak, P Pare, JWD McDonald, R Dube, A Cohen, AH Steinhart, S Landau, RA Aguzzi, IH Fox, and MK Vandervoort. Treatment of ulcerative colitis with a humanized antibody to the alpha(4)beta(7) integrin. *New England Journal of Medicine*, 352(24):2499–2507, Jan 2005.
125. DH Miller, OA Khan, WA Sheremata, LD Blumhardt, GPA Rice, MA Libonati, AJ Willmer-Hulme, CM Dalton, KA Miszkiel, and PW O'Connor. A controlled trial of natalizumab for relapsing multiple sclerosis. *New England Journal of Medicine*, 348(1):15–23, Jan 2003.

-
126. R Haubner, WA Weber, AJ Beer, E Vabulienė, D Reim, M Sarbia, KF Becker, M Goebel, R Hein, HJ Wester, H Kessler, and M Schwaiger. Noninvasive visualization of the activated alpha v beta 3 integrin in cancer patients by positron emission tomography and [f-18]galactogrd. *PLoS Medicine*, 2(3):244–252, Jan 2005.
 127. Roger Stupp and Curzio Ruegg. Integrin inhibitors reaching the clinic. *Journal of clinical oncology*, 25(13):1637–1638, Jan 2007.
 128. James Arthos, Claudia Cicala, Elena Martinelli, Katilyn Macleod, Donald Van Ryk, Danlan Wei, Zhen Xiao, Timothy D Veenstra, Thomas P Conrad, Richard A Lempicki, Sherry McLaughlin, Massimiliano Pascuccio, Ravindra Gopaul, Jonathan McNally, Catherine C Cruz, Nina Censo-plano, Eva Chung, Kristin N Reitano, Shyam Kottlil, Diana J Goode, and Anthony S Fauci. Hiv-1 envelope protein binds to and signals through integrin alpha(4)beta(7), the gut mucosal homing receptor for peripheral t cells. *Nat Immunol*, 9(3):301–309, Jan 2008.
 129. M Barczyk, S Carracedo, and D Gullberg. Integrins. *Cell Tissue Res*, Jan 2010.
 130. Bing-Hao Luo, Christopher V Carman, and Timothy A Springer. Structural basis of integrin regulation and signaling. *Annual review of immunology*, 25:619–647, Jan 2007.
 131. M Amin Arnaut, Simon L Goodman, and Jian-Ping Xiong. Structure and mechanics of integrin-based cell adhesion. *Curr Opin Cell Biol*, 19(5):495–507, Oct 2007.
 132. Janet A Askari, Patrick A Buckley, A Paul Mould, and Martin J Humphries. Linking integrin conformation to function. *Journal of cell science*, 122(Pt 2):165–70, Jan 2009.
 133. David S Goodsell. Integrin conformation figure. *RCSB PDB*, Molecule of the month(Feb), 2011.
 134. J Takagi, BM Petre, T Walz, and TA Springer. Global conformational rearrangements in integrin extracellular domains in outside-in and inside-out signaling. *Cell*, 110(5):599–611, Jan 2002.
 135. Brian D Adair and Mark Yeager. Three-dimensional model of the human platelet integrin alpha iibbeta 3 based on electron cryomicroscopy and x-ray crystallography. *Proc Natl Acad Sci U S A*, 99(22):14059–64, Oct 2002.
 136. Kay-Eberhard Gottschalk and Horst Kessler. Evidence for hetero-association of transmembrane helices of integrins. *FEBS letters*, 557(1-3):253–8, Jan 2004.
 137. Kay-Eberhard Gottschalk. A coiled-coil structure of the alpha iibbeta3 integrin transmembrane and cytoplasmic domains in its resting state. *Structure*, 13(5):703–12, May 2005.

138. Bing-Hao Luo, Timothy A Springer, and Junichi Takagi. A specific interface between integrin transmembrane helices and affinity for ligand. *PLoS Biol*, 2(6):e153, Jun 2004.
139. Seiji Tadokoro, Sanford J Shattil, Koji Eto, Vera Tai, Robert C Liddington, Jose M de Pereda, Mark H Ginsberg, and David A Calderwood. Talin binding to integrin beta tails: a final common step in integrin activation. *Science*, 302(5642):103–106, Oct 2003.
140. Kate L Wegener, Anthony W Partridge, Jaewon Han, Andrew R Pickford, Robert C Liddington, Mark H Ginsberg, and Iain D Campbell. Structural basis of integrin activation by talin. *Cell*, 128(1):171–182, Jan 2007.
141. P E Hughes, F Diaz-Gonzalez, L Leong, C Wu, J A McDonald, S J Shattil, and M H Ginsberg. Breaking the integrin hinge. a defined structural constraint regulates integrin signaling. *J Biol Chem*, 271(12):6571–4, Mar 1996.
142. Tsan Xiao, Junichi Takagi, Barry S Collier, Jia-Huai Wang, and Timothy A Springer. Structural basis for allostery in integrins and binding to fibrinogen-mimetic therapeutics. *Nature*, 432(7013):59–67, Nov 2004.
143. Jianghai Zhu, Bing-Hao Luo, Tsan Xiao, Chengzhong Zhang, Noritaka Nishida, and Timothy A Springer. Structure of a complete integrin ectodomain in a physiologic resting state and activation and deactivation by applied forces. *Mol Cell*, 32(6):849–861, Jan 2008.
144. Ronen Zaidel-Bar, Shalev Itzkovitz, Avi Ma’ayan, Ravi Iyengar, and Benjamin Geiger. Functional atlas of the integrin adhesome. *Nature cell biology*, 9(8):858–868, Jan 2007.
145. Begoña Garcia-Alvarez, JM de Pereda, David A Calderwood, TS Ulmer, David R Critchley, Iain D Campbell, Mark H Ginsberg, and RC Liddington. Structural determinants of integrin recognition by talin. *Mol Cell*, 11(1):49–58, Jan 2003.
146. Guy Tanentzapf and Nicholas H Brown. An interaction between integrin and the talin ferm domain mediates integrin activation but not linkage to the cytoskeleton. *Nat Cell Biol*, 8(6):601–606, Jun 2006.
147. R O McCann and S W Craig. The i/lweq module: a conserved sequence that signifies f-actin binding in functionally diverse proteins from yeast to mammals. *Proc Natl Acad Sci U S A*, 94(11):5679–84, May 1997.
148. Mohamed Bouaouina, Yatish Lad, and David A Calderwood. The n-terminal domains of talin cooperate with the phosphotyrosine binding-like domain to activate beta1 and beta3 integrins. *J Biol Chem*, 283(10):6118–25, Mar 2008.

149. Antreas C Kalli, Kate L Wegener, Benjamin T Goult, Nicholas J Anthis, Iain D Campbell, and Mark S P Sansom. The structure of the talin/integrin complex at a lipid bilayer: an nmr and md simulation study. *Structure*, 18(10):1280–8, Oct 2010.
150. David J Brockwell, Emanuele Paci, Rebecca C Zinober, Godfrey S Beddard, Peter D Olmsted, D Alastair Smith, Richard N Perham, and Sheena E Radford. Pulling geometry defines the mechanical resistance of a beta-sheet protein. *Nat Struct Biol*, 10(9):731–737, Sep 2003.
151. R Dean Astumian. Thermodynamics and kinetics of a brownian motor. *Science*, 276(5314):917–22, May 1997.
152. H Noji, R Yasuda, M Yoshida, and K Kinosita. Direct observation of the rotation of f1-atpase. *nature.com*, 386:299–302, Jan 1997.
153. K Fahrner, W Ryu, and H Berg. Biomechanics: bacterial flagellar switching under load. *Nature*, 423:938, Jan 2003.
154. T R Kelly, H De Silva, and R A Silva. Unidirectional rotary motion in a molecular system. *Nature*, 401(6749):150–2, Sep 1999.
155. D Horinek and J Michl. Surface-mounted altitudinal molecular rotors in alternating electric field: Single-molecule parametric oscillator molecular dynamics. *Proc Natl Acad Sci U S A*, 102(40):14175–14180, Jan 2005.
156. Heather L Tierney, Ashleigh E Baber, E. Charles H Sykes, Alexey Akimov, and Anatoly B Kolomeisky. Dynamics of thioether molecular rotors: Effects of surface interactions and chain flexibility. *J Phys Chem C*, 113(25):10913–10920, Jan 2009.

CV - Jan Neumann

Personal Data

Name Jan Neumann
Place of Birth Wolfenbüttel
Citizenship German



Education

3/2007 to present **PhD in Physics**
Thesis advisor: Kay E. Gottschalk
Chair for Applied Physics (Hermann E. Gaub)
Ludwig-Maximilians-University, Munich, Germany

10/2001 - 2/2007 **Diploma in Physics**
Diploma thesis: Protein-Protein Interactions with Molecular Dynamics Simulations
Thesis advisor: Kay E. Gottschalk
Chair for Applied Physics (Hermann E. Gaub)
Ludwig-Maximilians-University, Munich, Germany

6/2000 **Allgemeine Hochschulreife**
Katharinen Gymnasium Ingolstadt, Germany

Honors and Awards

11/2008 CENS Publication Award 2008

10/2007 Scholarship of the Elitenetzwerk Bayern in the IDK NanoBio-Technology

06/2000 Award of the German Physical Society (DPG)

06/2000 Award of the city of Ingolstadt for the best Allgemeine Hochschulreife 2000 at my Grammar School

03/2000 Winning Team Member at the Day-of-Mathematics 2000 at the University of Ulm

15. June 2011

Acknowledgement

Finally, I want to thank everyone who contributed and supported me during this thesis. First of all, thanks to Prof. Dr. Kay E. Gottschalk for supervising my thesis and letting me stay in Munich during the last year. Thanks to Prof. Dr. Hermann E. Gaub for the opportunity to do my thesis at his chair in a great working environment. Special thanks to Prof. R. Dean Astumian for all his support, ideas and great discussions on the rotor project and everything else. Thanks to Prof. Dr. Roland Netz for his support as my second IDK supervisor and to Prof. Dr. Dominik Horinek for his time and helpful discussions on the rotor project.

Special thanks to Martin Höfling for a great time in the office or on trips like the JNN, for all the interesting scientific or totally unrelated discussions. Thanks to Dr. Julia Zimmermann for a great working atmosphere on our antibody publication. Thanks to Jan Opfer, Sandra Baumann, Julia Schmitz and Kamila Klamecka for critical reading of my scripts, many helpful discussions and a good time at the office.

I very much thank the whole Gambicrew for a great atmosphere at the university. Further, I like to thank all the IDK-NBT students for a great time at workshops and seminars and especially Julia Zimmermann and Marilena Pinto for your constant support. I would like to express my thanks to the Elitenetzwerk Bayern for financial support with the IDK-NBT scholarship.

This thesis would not have been possible without the support from my friends and family. Especially, I sincerely thank Nadine Schwierz for all her great scientific support, constant motivation and the marvelous time we share. Last but not least, my greatest thanks goes to my parents Gerd and Rosemarie who supported and accompanied me with their encouragement, their trust in my abilities and their backing in all those years.